Interaction of Close-in Giant Exoplanets with their Host Stars

Wing-Huen Ip

Institutes of Astronomy and Space Science
National Central University
Taiwan

Kobe International School of Planetary Science

September 16, 2004

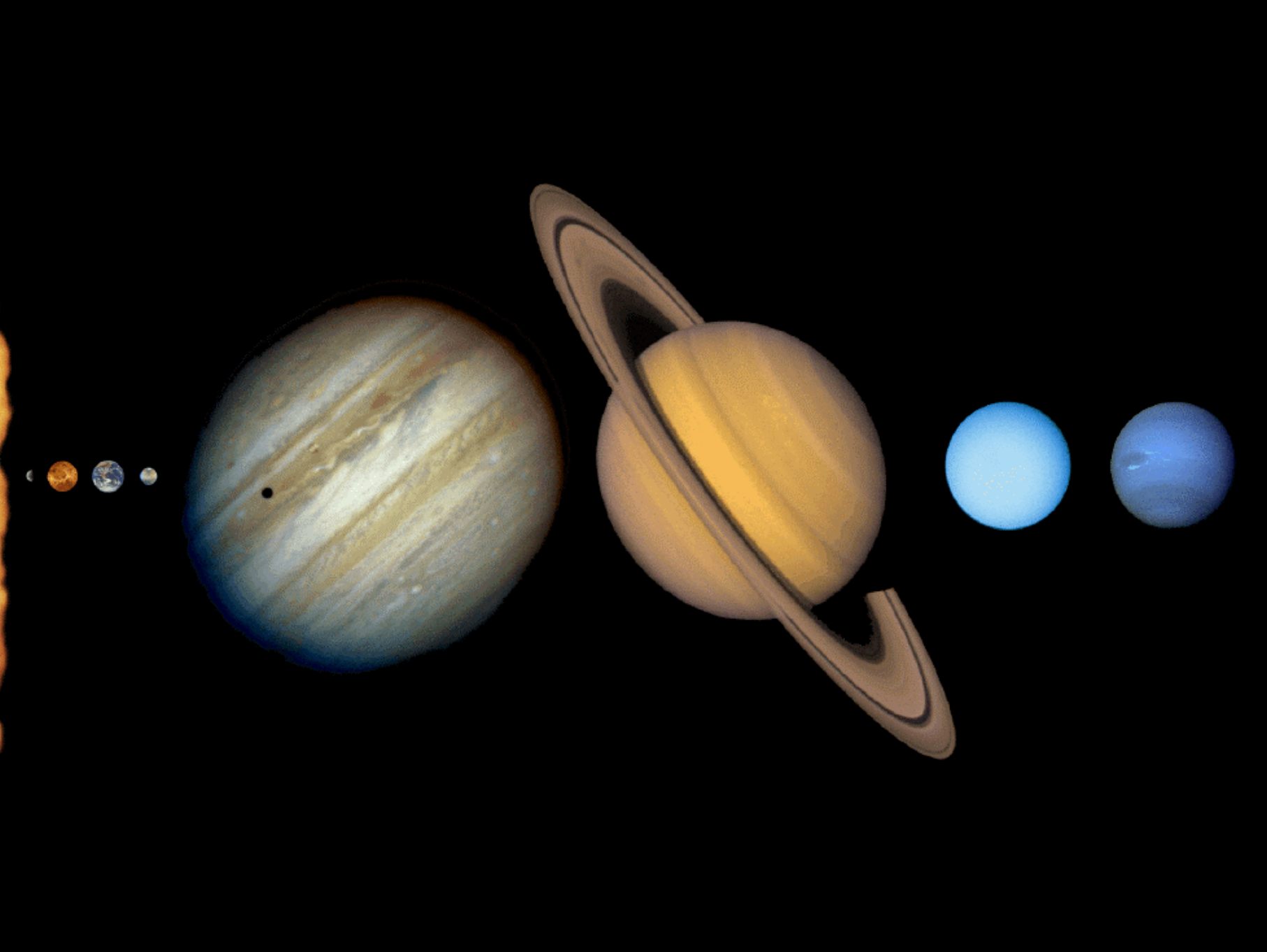

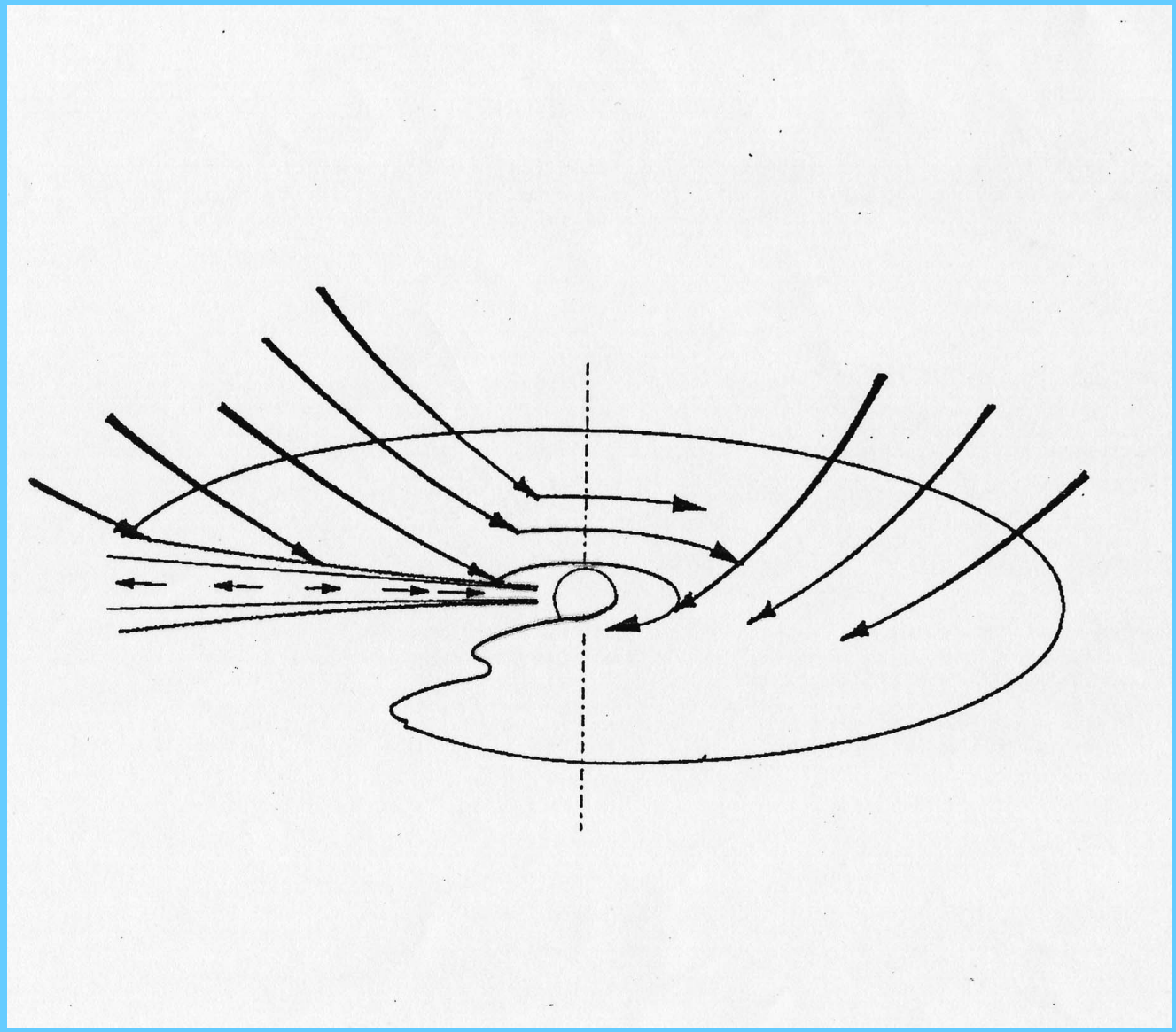

P. Cassen and A. Summers (1983) Icarus, 53, 26-40.

Accretion Disc Evolution

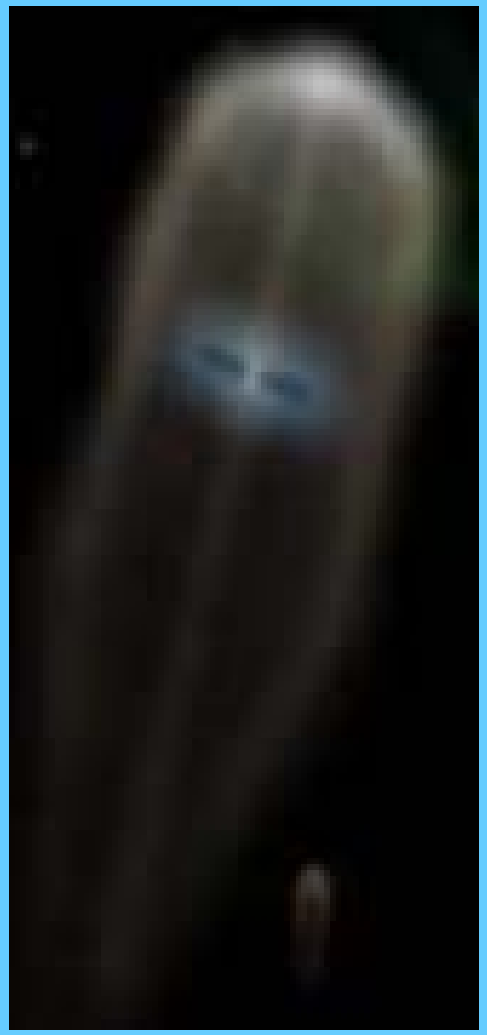

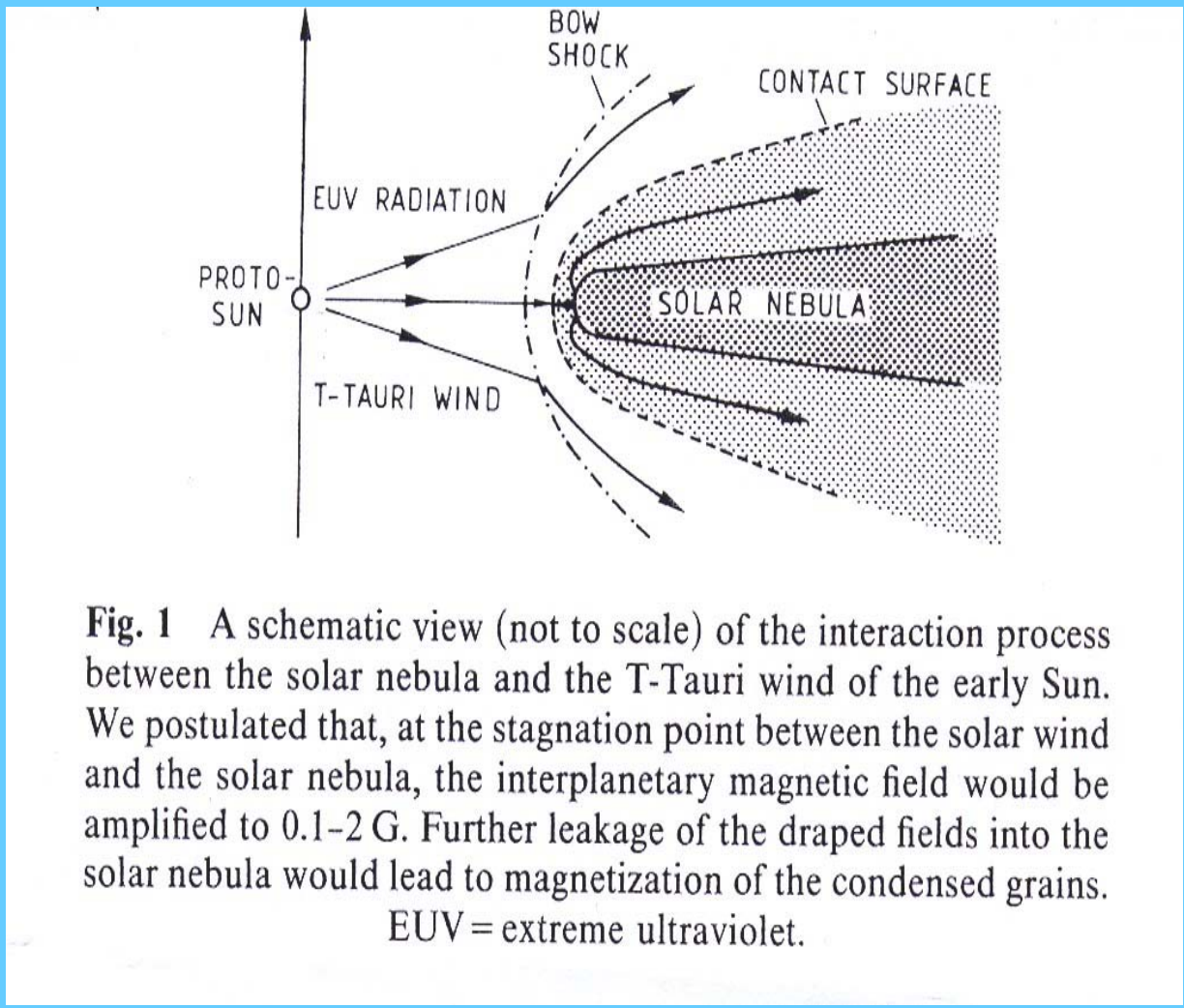

Fig. 1 A schematic view (not to scale) of the interaction process between the solar nebula and the T-Tauri wind of the early Sun. We postulated that, at the stagnation point between the solar wind and the solar nebula, the interplanetary magnetic field would be amplified to 0.1–2 G. Further leakage of the draped fields into the solar nebula would lead to magnetization of the condensed grains. EUV = extreme ultraviolet.

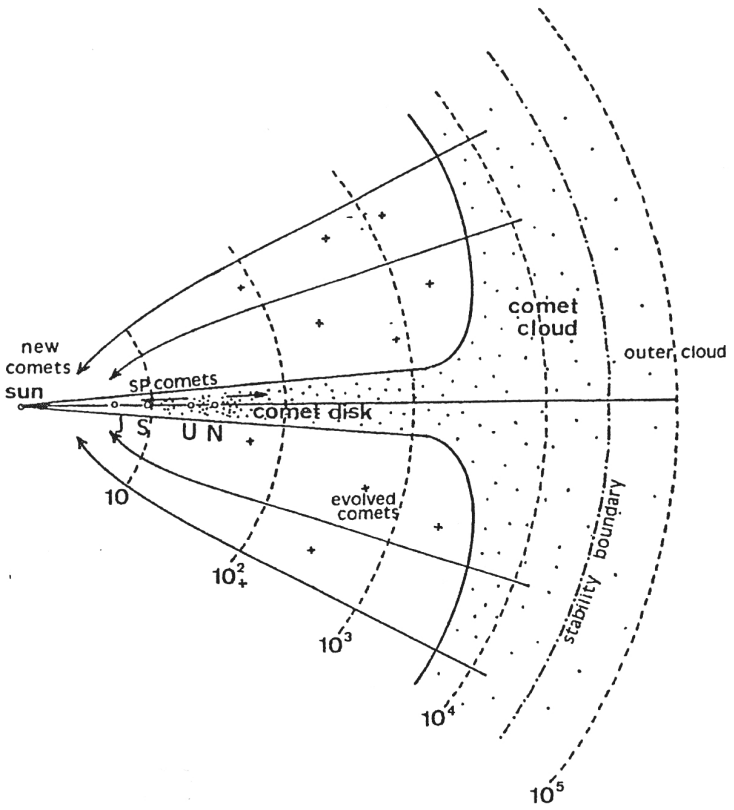

Figure 7. A schematic picture of the current spatial distribution of comets around the Solar System if they formed in the protoplanetary disk. A comet disk might still be present, stretching from the region of the outer planets to a few 10^3 AU. Farther away, the action of external perturbers should have by now randomized the orbital planes of comets. New comets probably come from the Oort cloud, whereas most short-period comets may come from the comet disk (*e.g.*, the Kuiper belt). The spherical volume of a few thousand AU in radius should contain evolved long-period comets (crosses). The dashed circles indicate distances to the Sun in AU. From Fernández and Ip (1991).

J.A. Fernandez and W.H. Ip (1984) Icarus, 58, 109-120

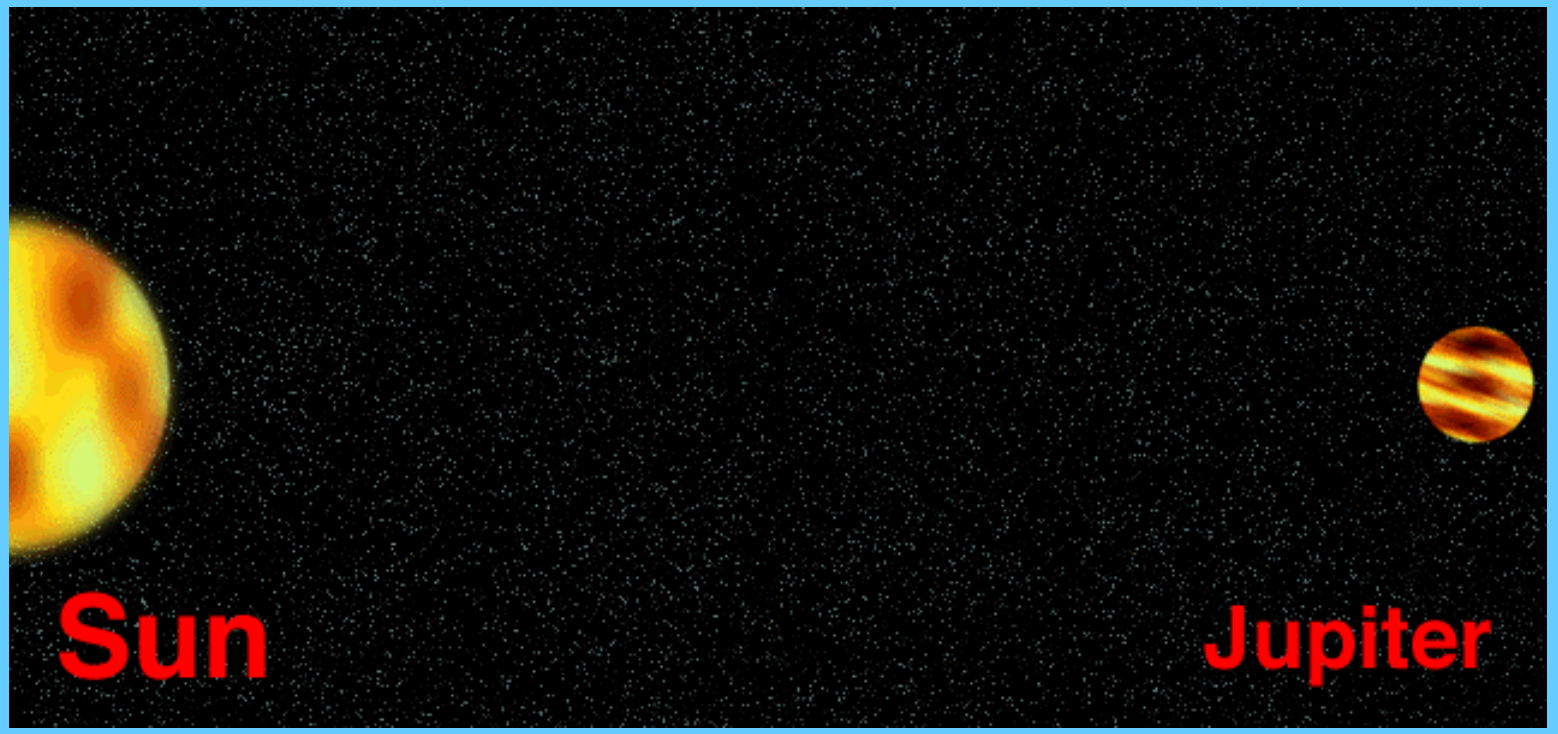
Sun
Jupiter

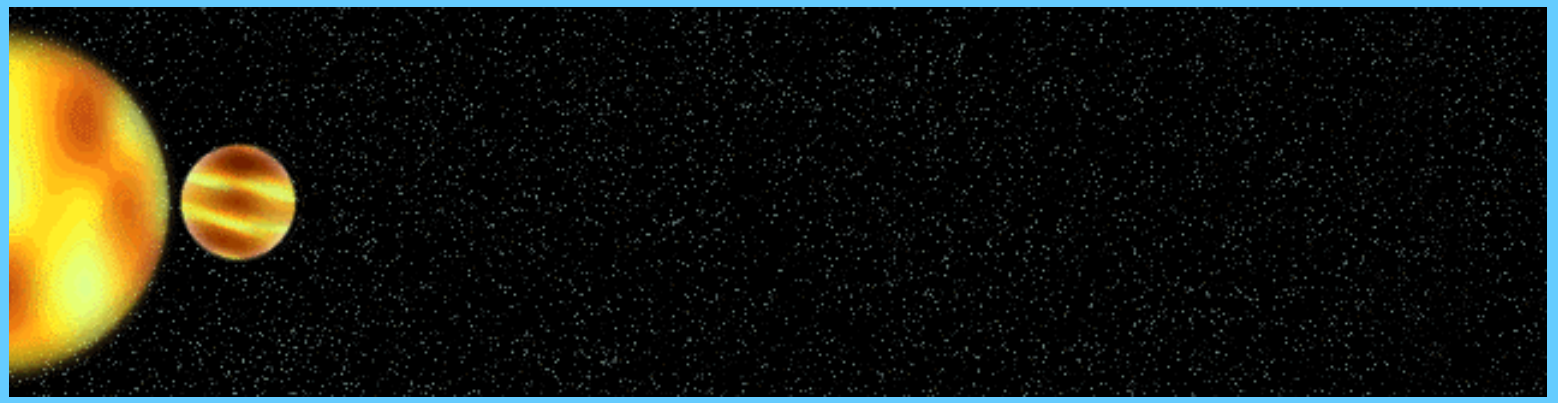

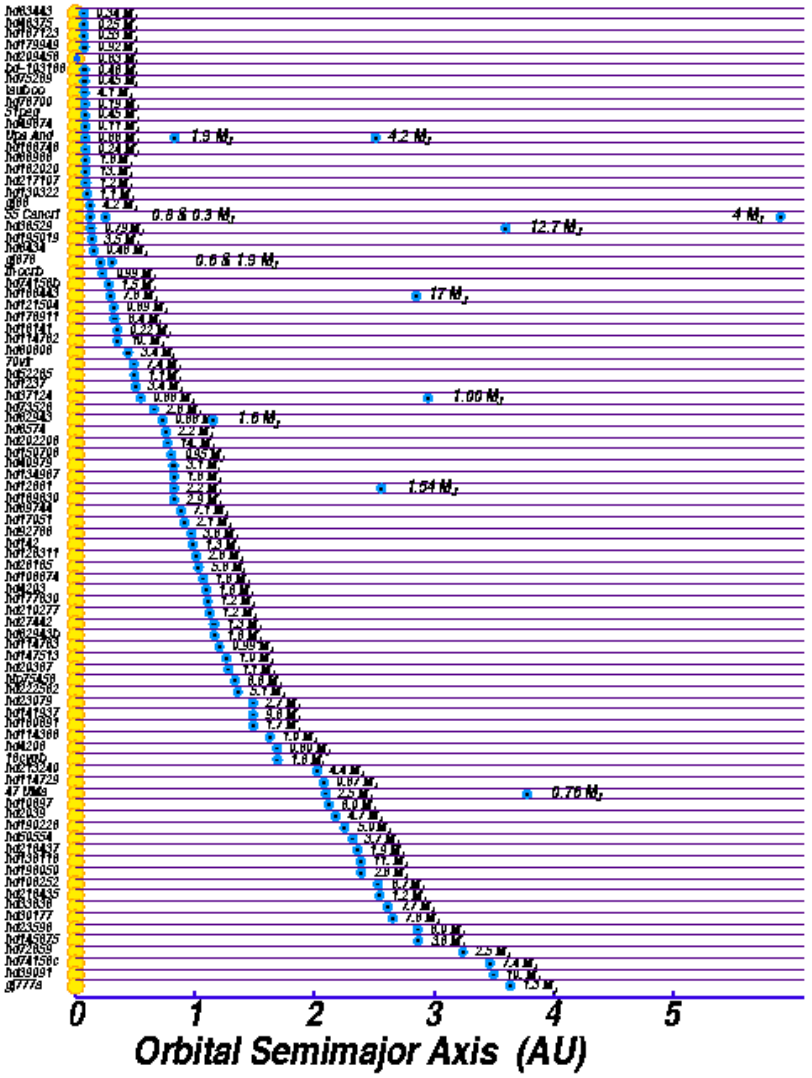
1.9 M,
4.2 M,
0.6 & 0.3 M,
12.7 M,
4 M,
0.6 & 1.9 M,
17 M,
1.00 M,
1.6 M,
1.54 M,
0.76 M,
0
1
2
3
4
5
Orbital Semimajor Axis (AU)

Giant Exoplanets close to Host Stars ~ Diversity of Solar Systems

Outline

Part I

- Detection methods
- Observational Statistics
- Orbital Migration
- Close-in Giant Exoplanets (CGEPs)

Part II

- Terrestrial and Oceanic Exoplanets
- Atmospheric Structure and Photochemistry of HD 209458b

Part III

- Stellar Interaction, Mass Loss and Evolution
- Ongoing Study

Exoplanets I

Planet Detection Methods

Michael Perryman, Rep. Prog. Phys., 2000, 63, 1209 (updated May 2004)
[corrections or suggestions please to michael.perryman@esa.int]

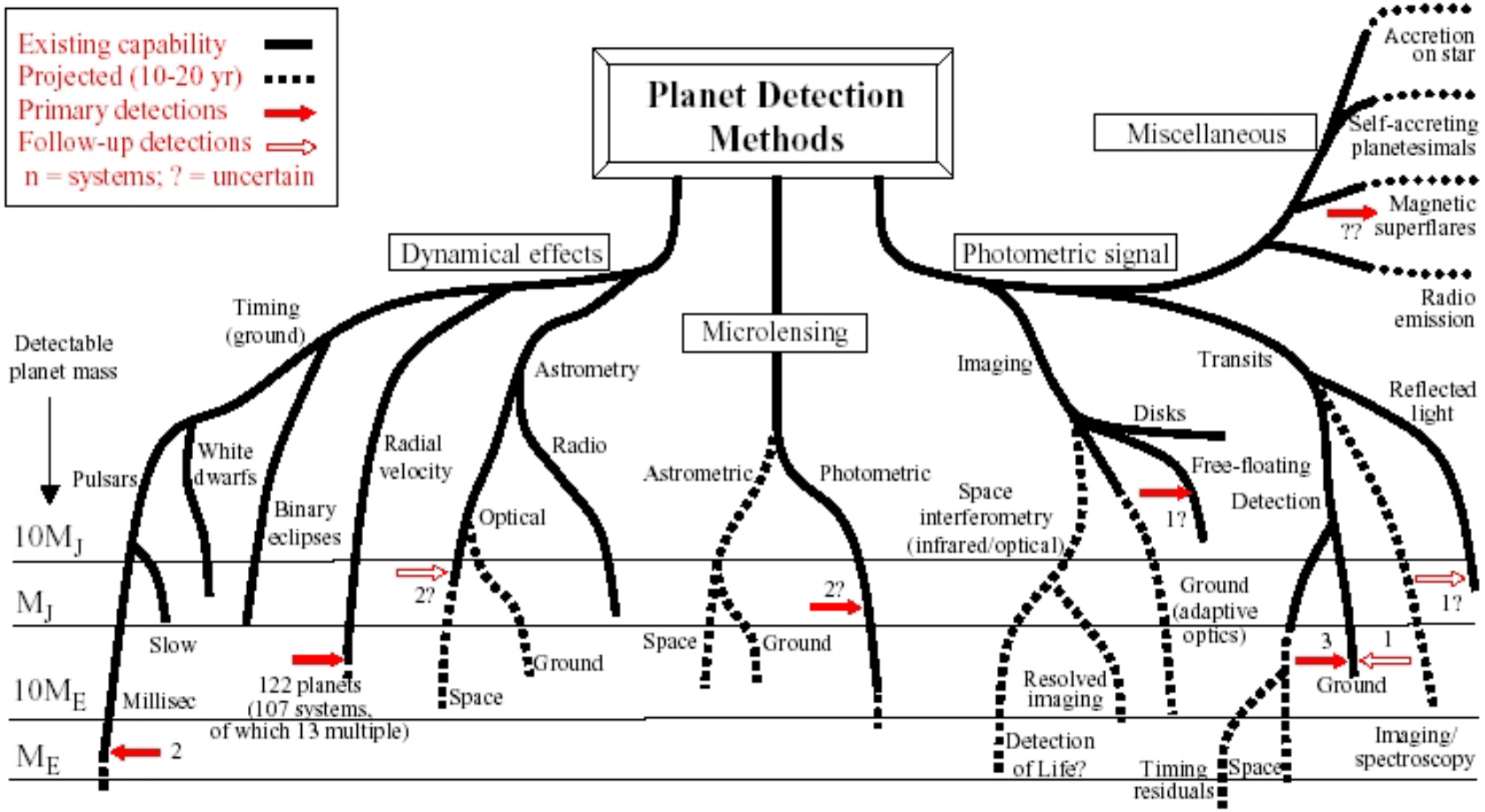

Detection Methods

- Radial Velocity Measurements
- Planetary Transit Measurements
- Gravitational Microlensing Measurements
- Infrared Spectral Signatures
- Direct Imaging Measurements

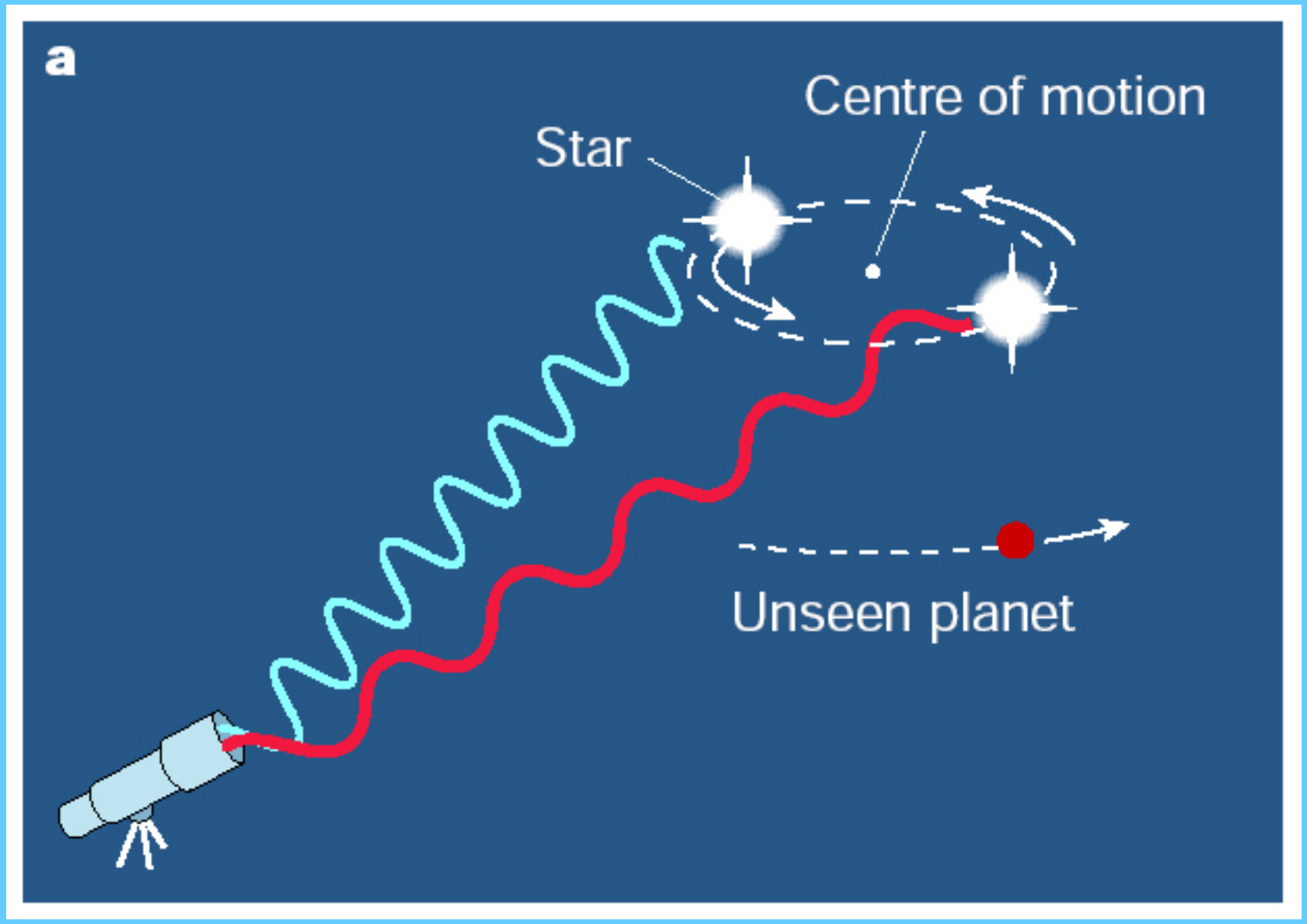

Lissauer (2002) Nature, 419, 355.

Radial Velocity Measurements

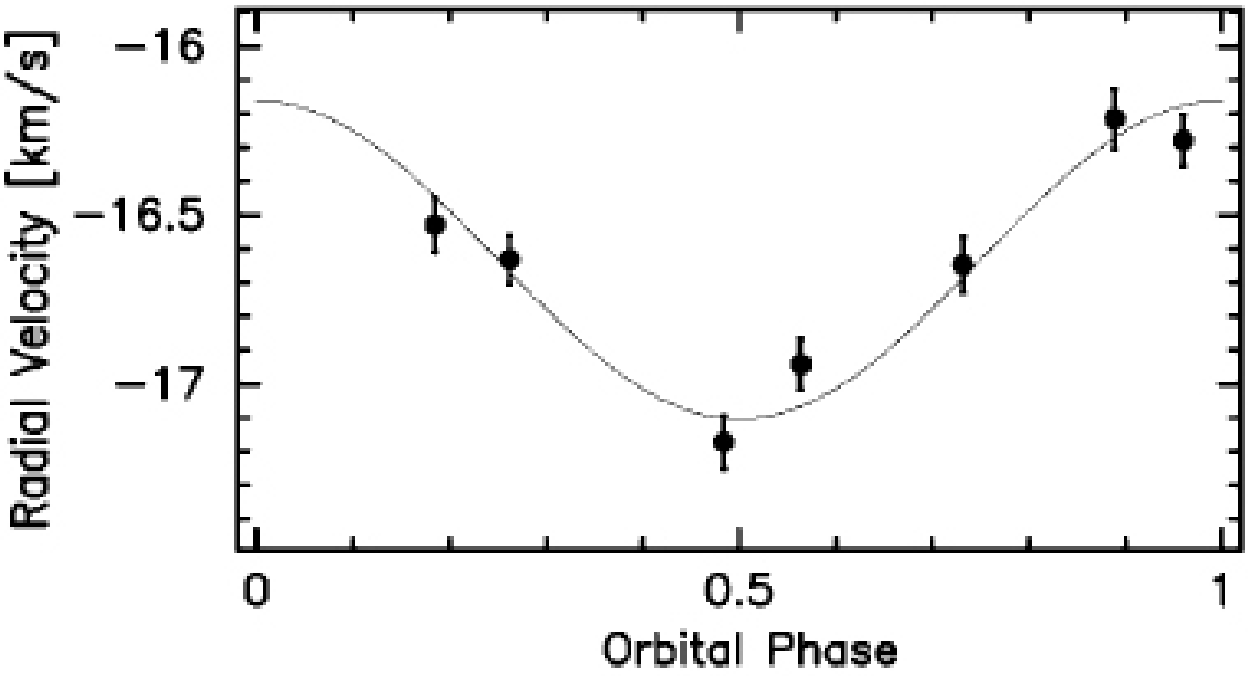

FIG. 1.—Radial velocity measurements for τ Boo as a function of orbital phase, along with the orbit determined by Butler et al. (1997). The only parameter we have adjusted is the velocity of the center of mass.

Konacki et al. (2004) ApJ. 609, L37.

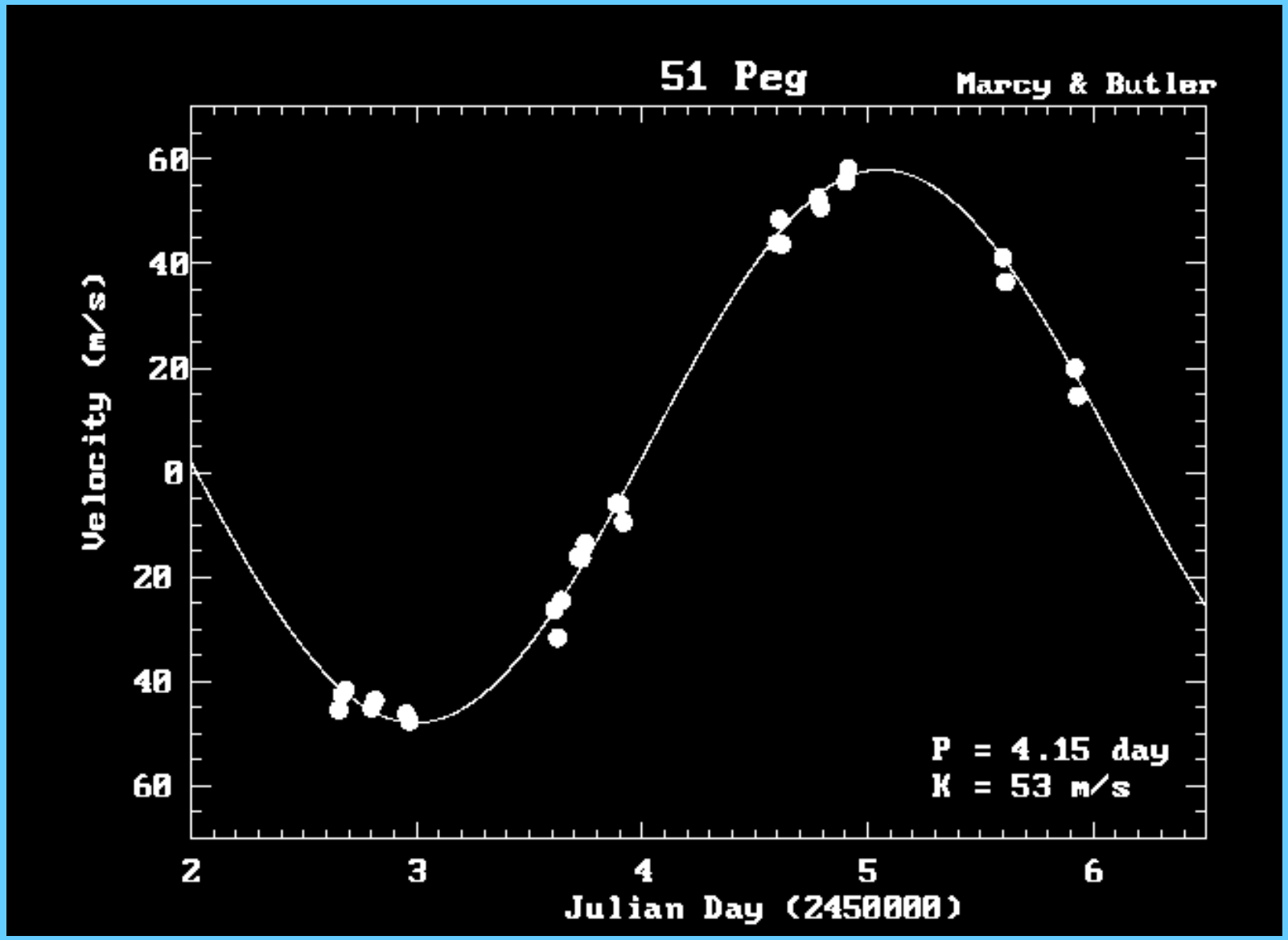
51 Peg
Marcy & Butler
Velocity (m/s)
60
40
20
0
20
40
60
2
3
4
5
6
Julian Day (2450000)
P = 4.15 day
K = 53 m/s

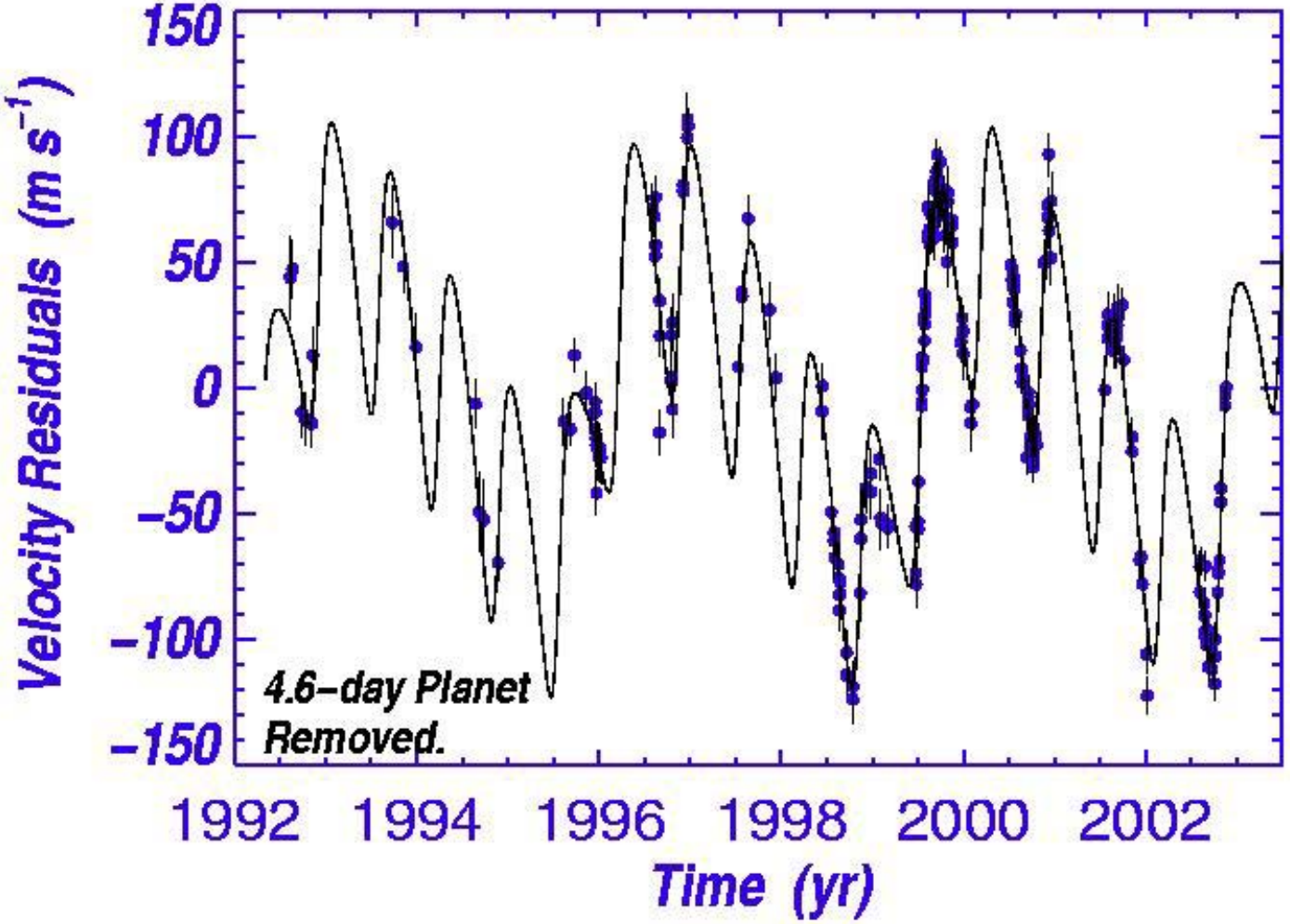
150
100
50
0
−50
−100
−150
Velocity Residuals (m s^{-1})
4.6−day Planet
Removed.
1992
1994
1996
1998
2000
2002
Time (yr)

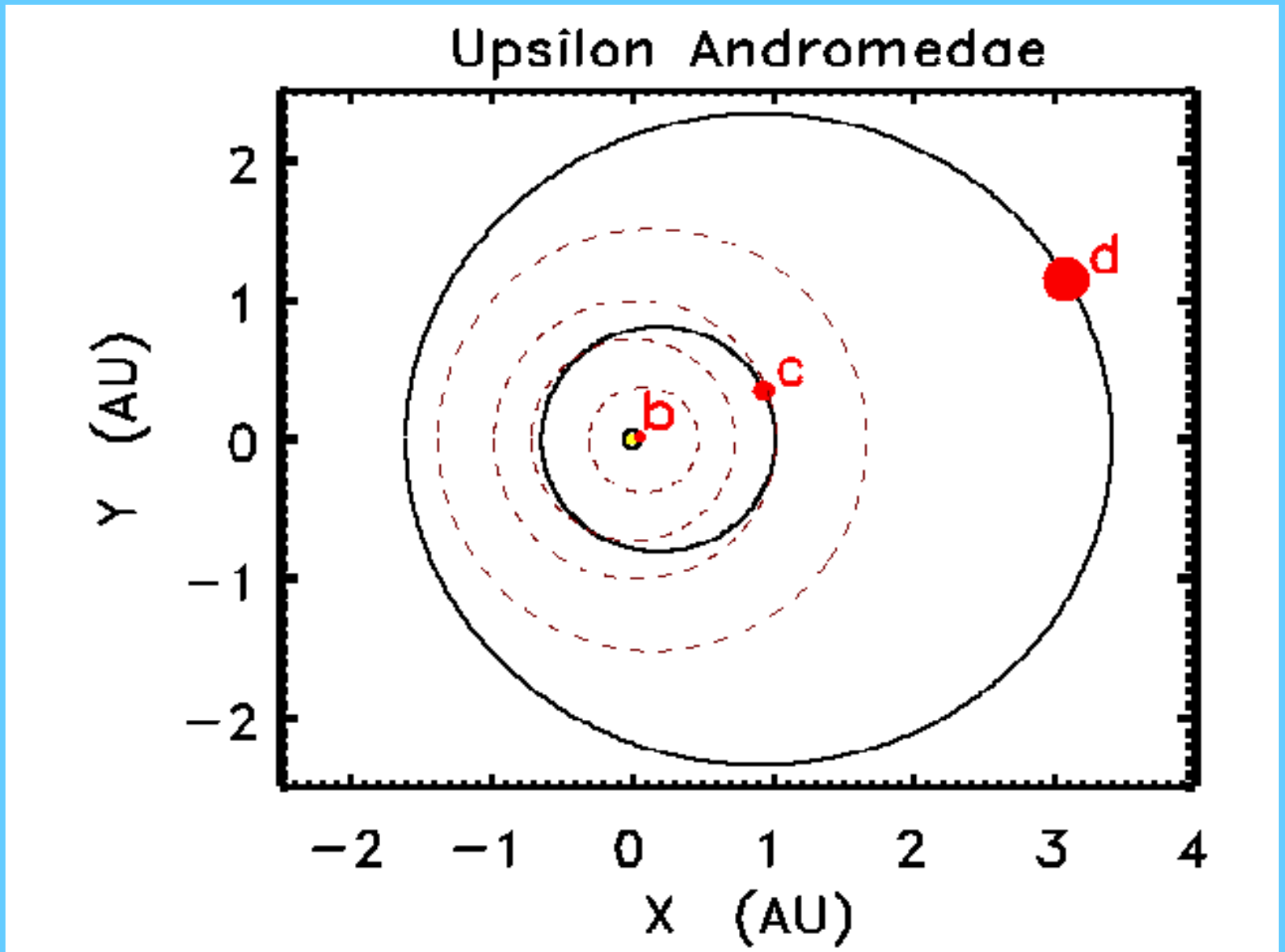
Upsilon Andromedae
Y (AU)
X (AU)
2
1
0
−1
−2
−2
−1
0
1
2
3
4
b
c
d

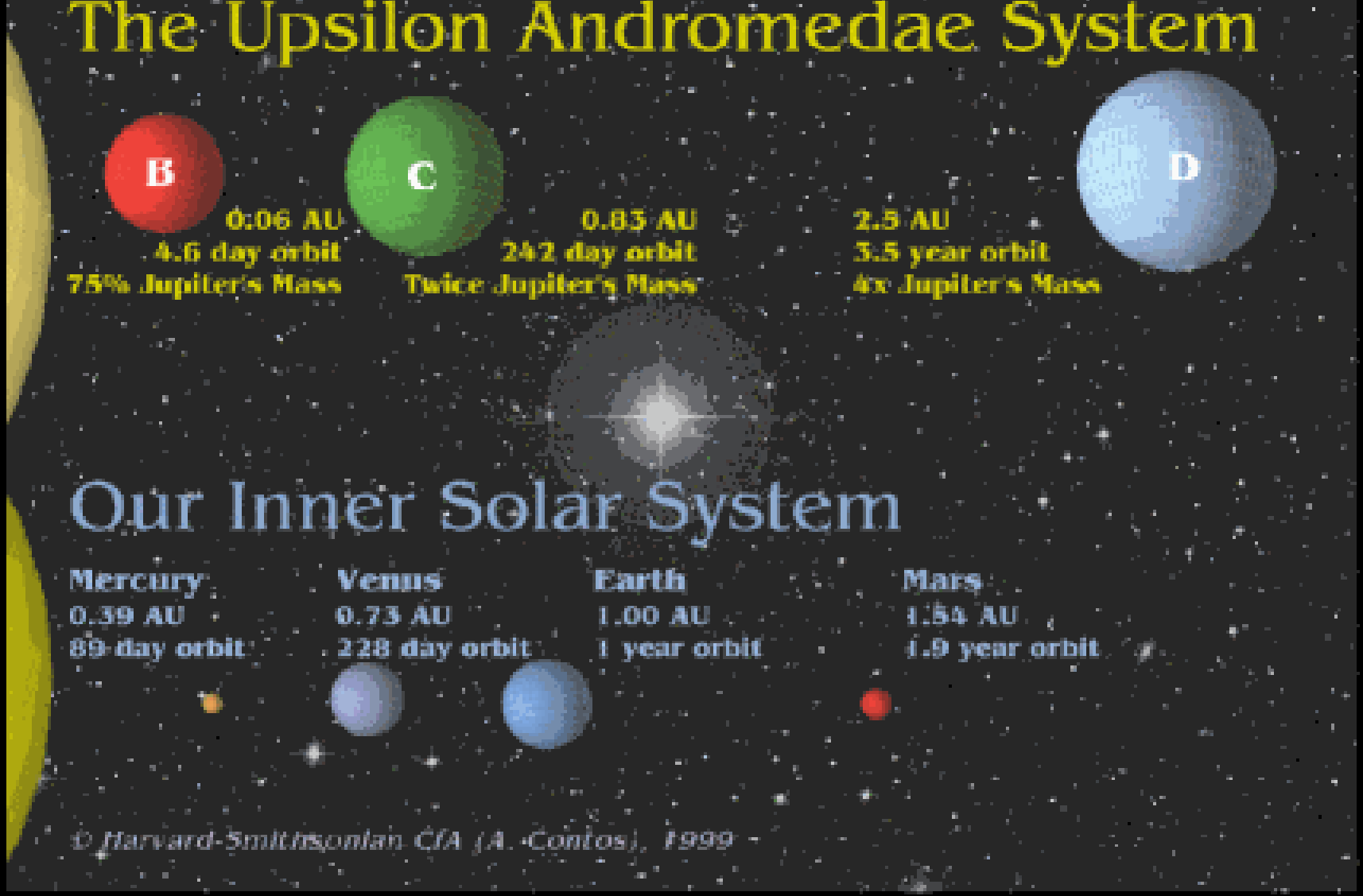

A Multiple Exoplanet System

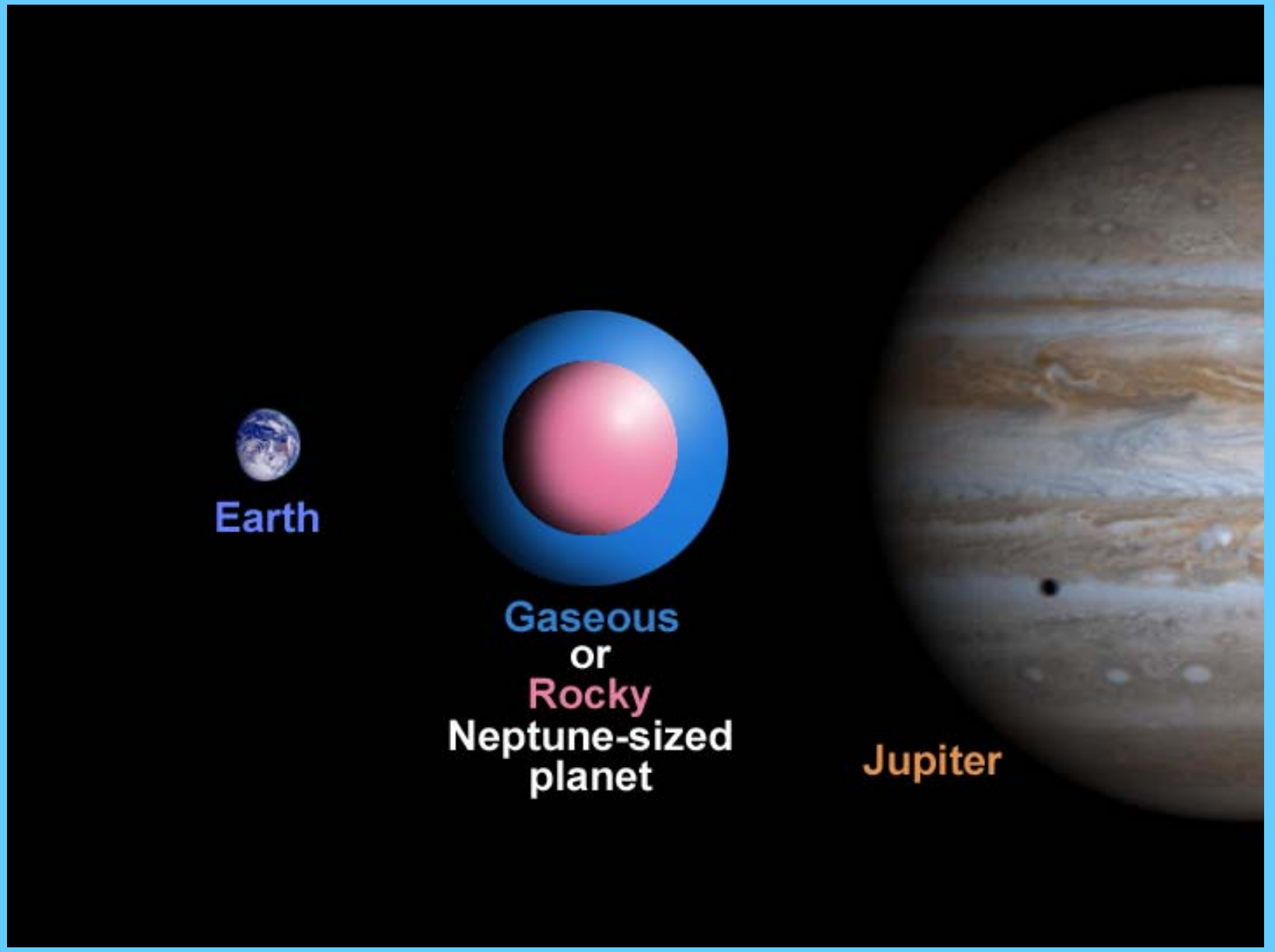
Earth
Gaseous
or
Rocky
Neptune-sized
planet
Jupiter

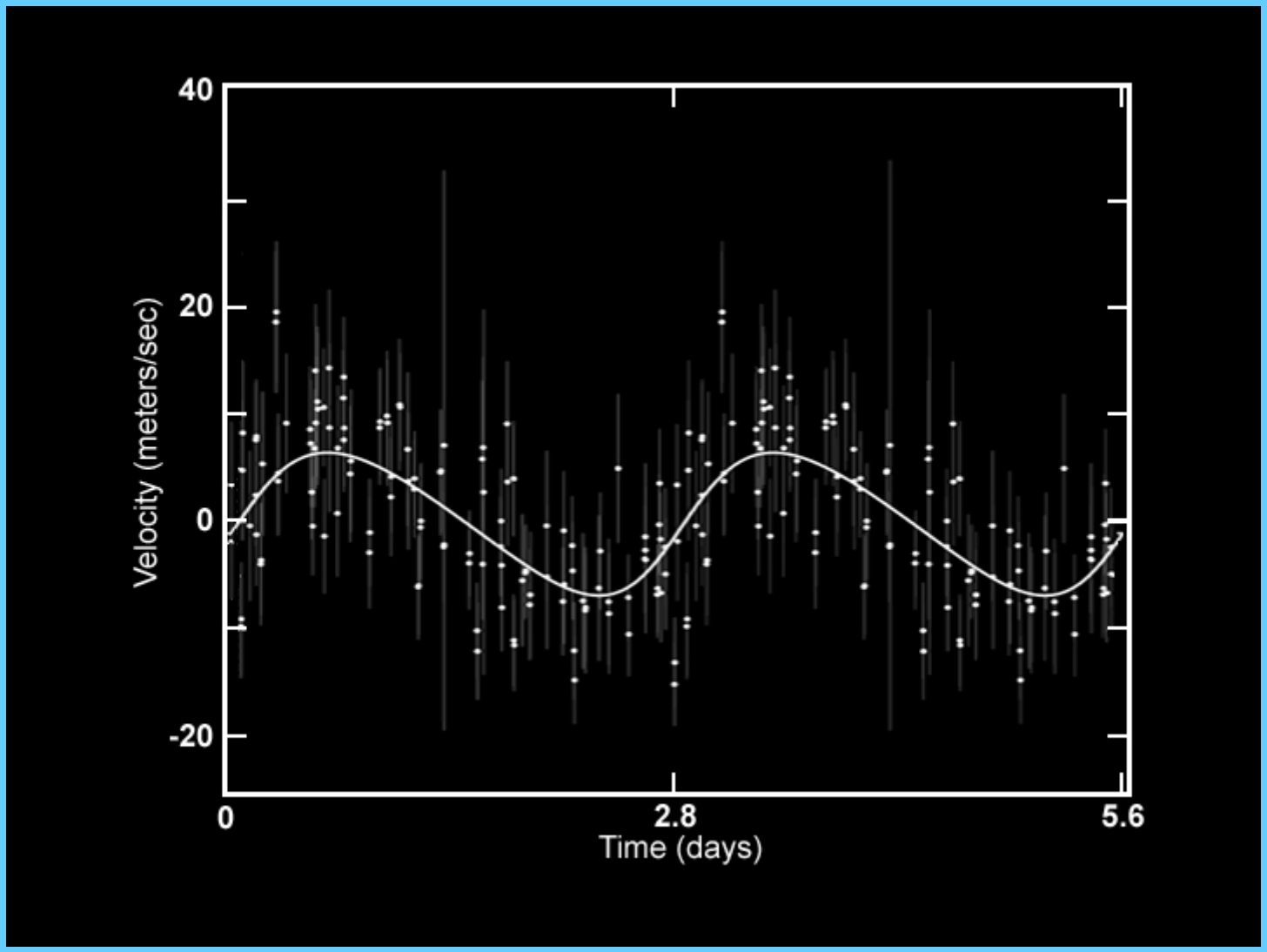
40
20
0
-20
Velocity (meters/sec)
0
2.8
5.6
Time (days)

Notes for 55 Cnc

by Jean Schneider

Update: **31 August 2004**

The planet(s):

- **Detection method:** Radial Velocity
- **Basic data:**

Name:	55 CnC e	55 CnC b	55 CnC c	55 CnC d
M.sin*i*:	0.045 ± 0.01 M_J = 14.2 ± 2.95 M_E	0.84 ± 0.07 M_J	0.21 ± 0.04 M_J	4.05 ± 0.4 M_J
Semi-major axis:	0.038 ± 0.001 AU	0.115 ± 0.003 AU	0.241 ± 0.005 AU	5.9 ± 0.9 AU
Orbital period:	2.81 ± 0.002 d.	14.653 ± 0.0006 d.	44.276 ± 0.021 d.	5360 ± 400 d.
Eccentricity:	0.174 ± 0.127	0.020 ± 0.02	0.339 ± 0.21	0.16 ± 0.06
Omega (deg):	261.7 ± 4	$99. \pm 35$	$61. \pm 25$	$201. \pm 22$
T_peri (JD-2450000):	3295.31 ± 0.32	1.479	31.4 ± 2.5	$2785. \pm 250$
Inclination:	-	-	-	

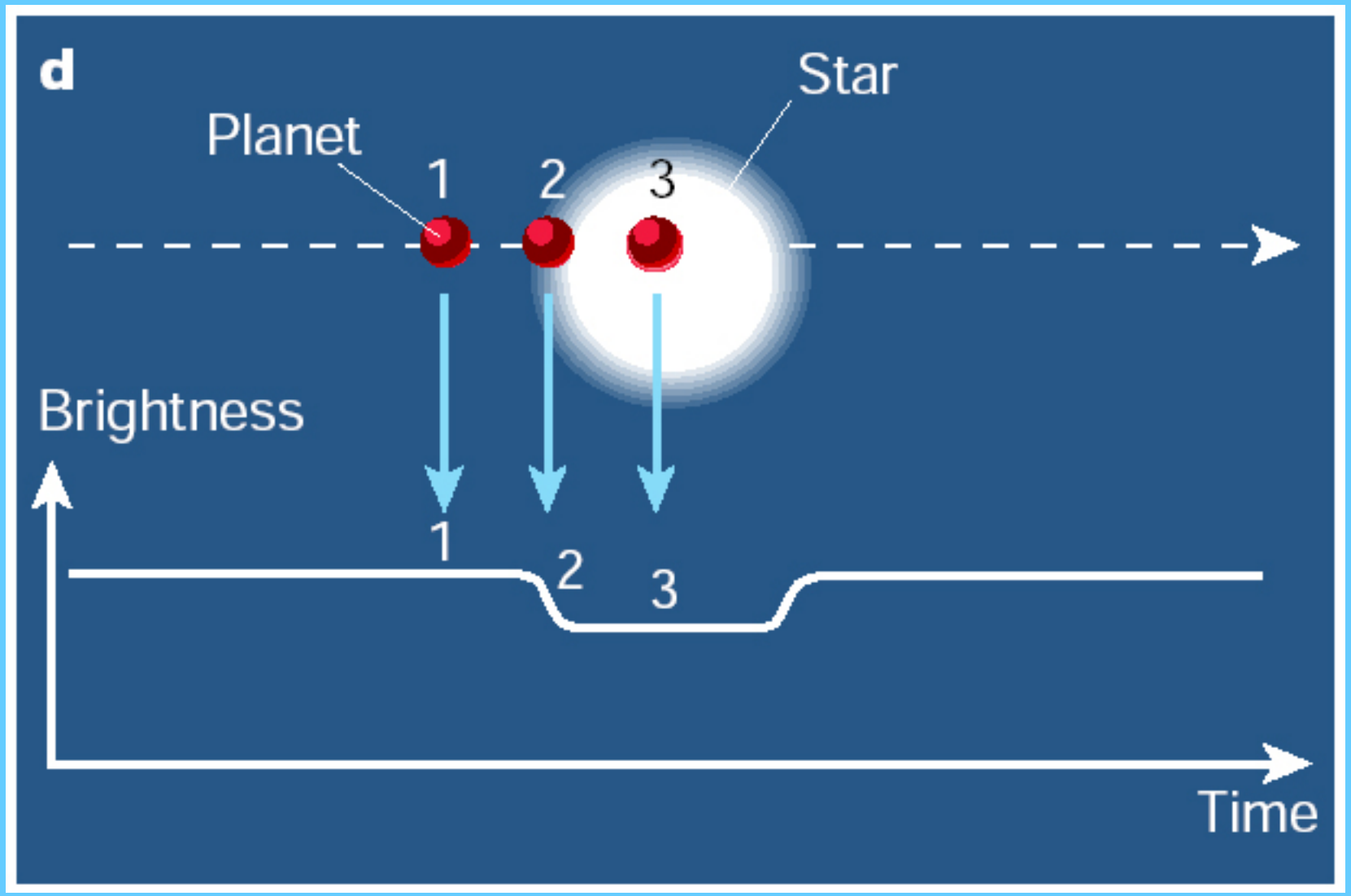

Lissauer (2002) Nature, 419, 355.

Lightcurve of HD 209458 observed with Hubble space telescope

intensity

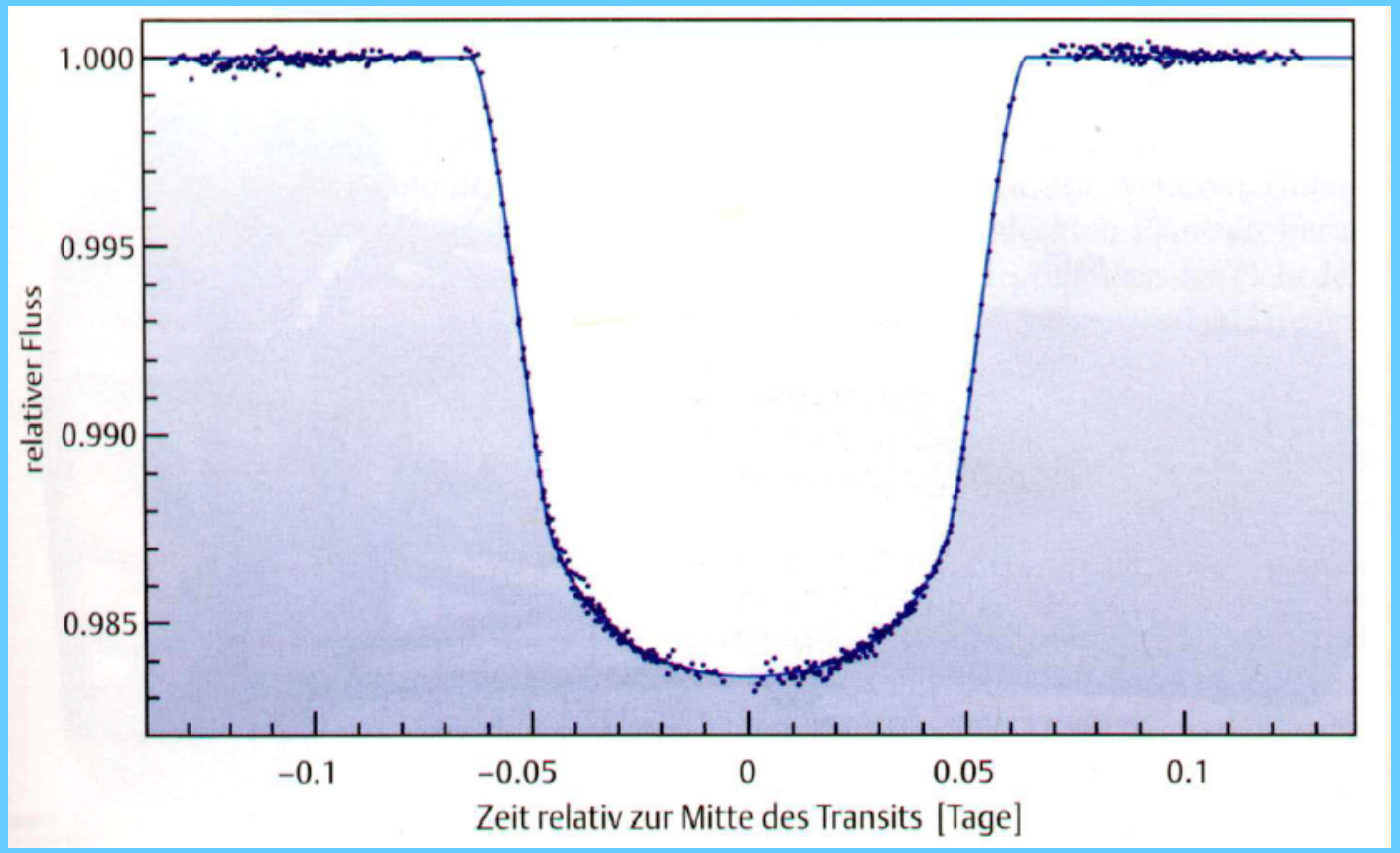

Time

Planetary Transit Measurements
HD 209458 b

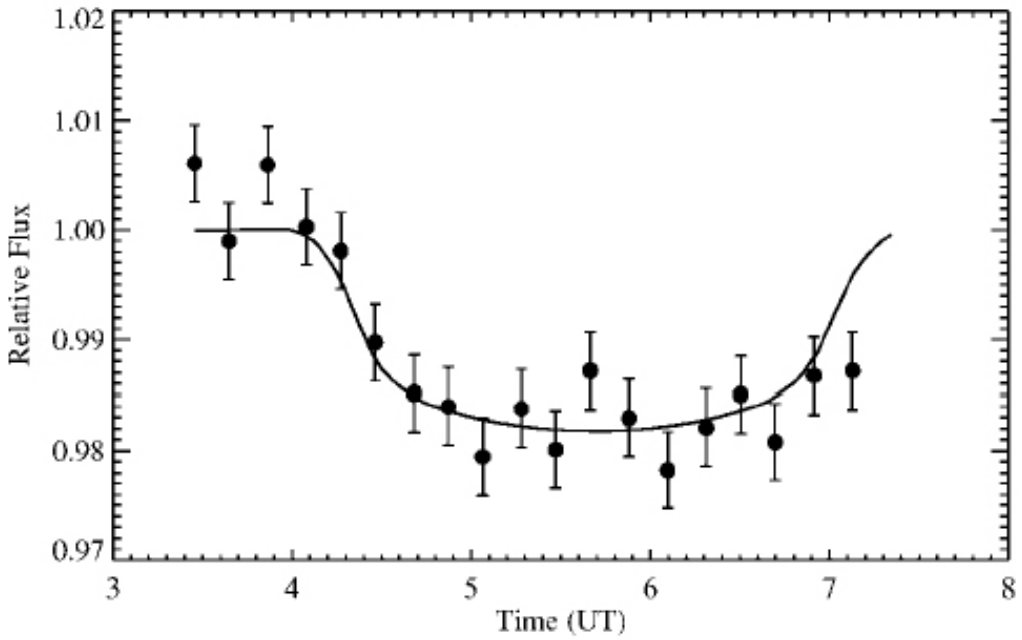

FIG. 1.—Detection of the planet transiting HD 209458, using the portable observatory described in the text. The data were taken from Fremont, CA, on the night of 2001 October 19/20. The solid curve is the model of Brown et al. (2001).

Charbonneau et al. (2003) ApJ, 529, L45.
Seagroves et al. (2003) PASP, 115, 1355.

Lulin Observatory

Open Cluster - NGC 381

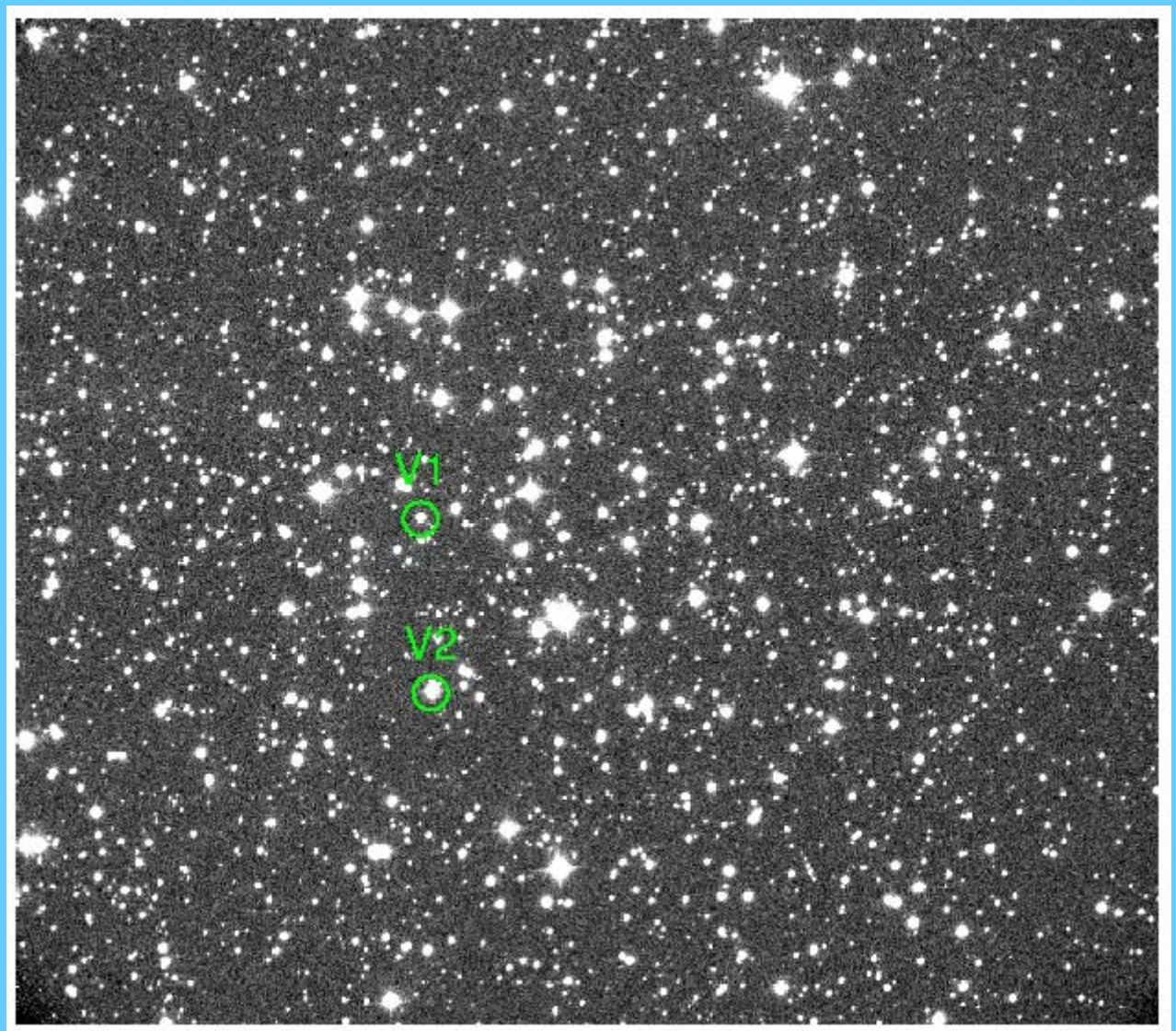

Gravitational Microlensing Measurements

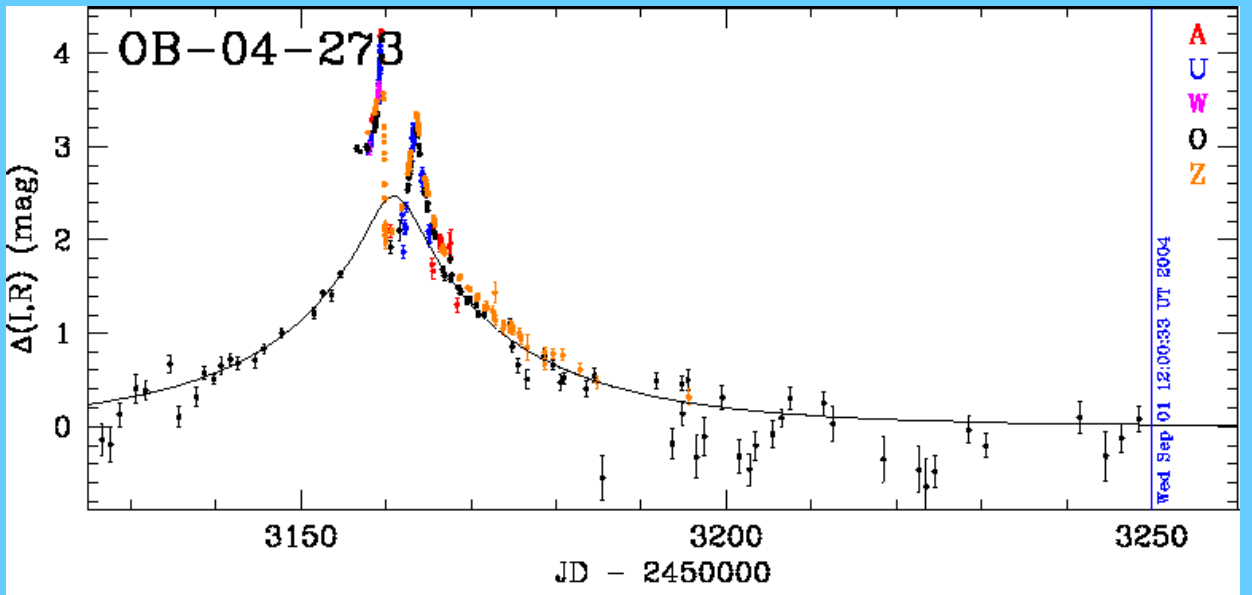

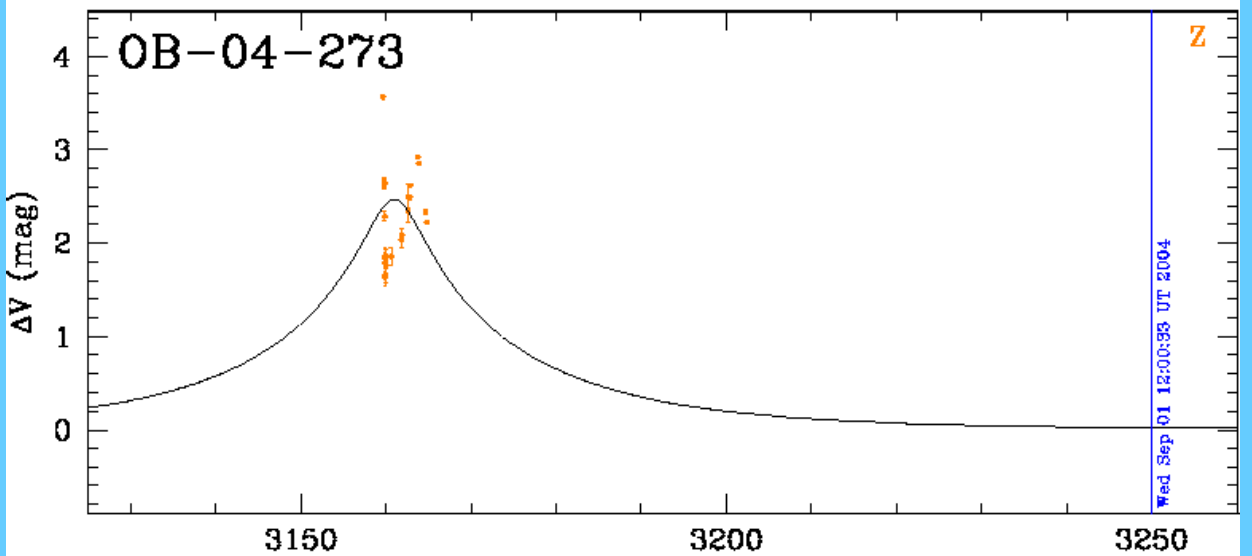

The Transisting CGEP OGLE-TR-56b

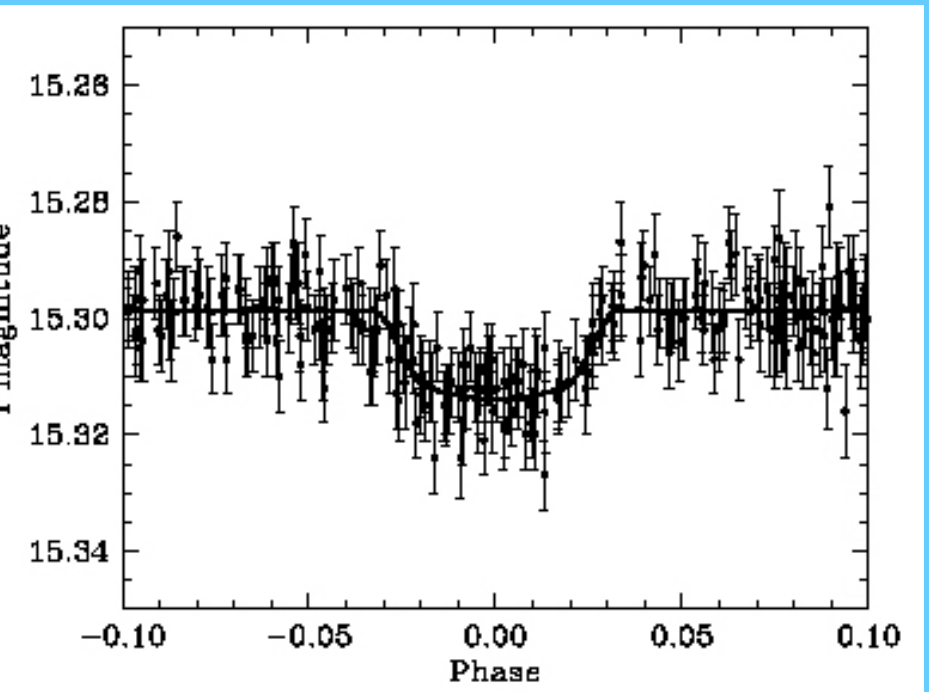

FIG. 4.—OGLE-III photometry for OGLE-TR-56 and our best-fit transit
ht curve.

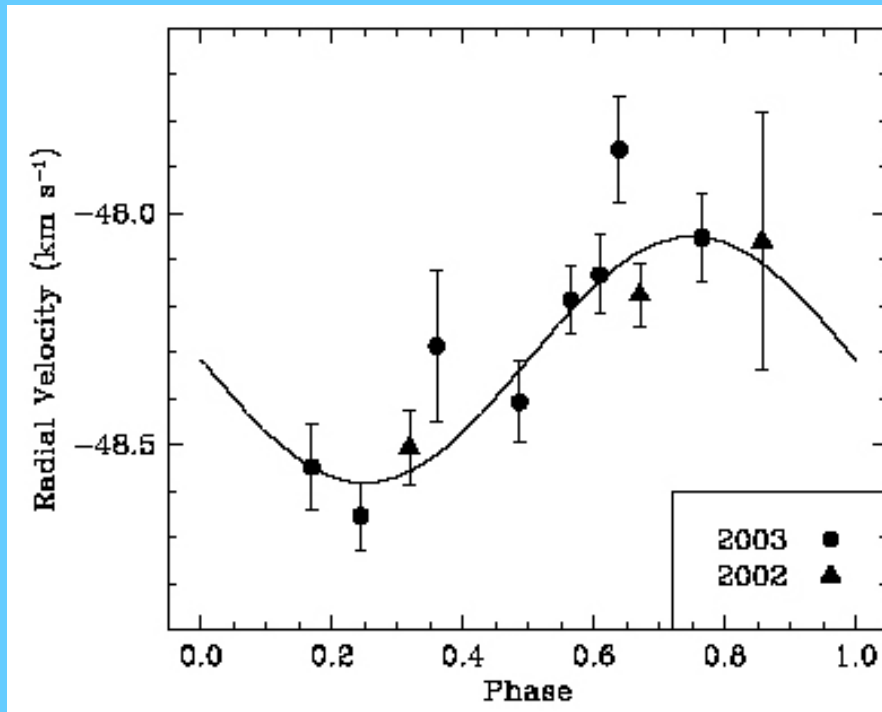

FIG. 1.—Radial velocity observations and fitted velocity curve for OGL
TR-56, as a function of orbital phase (ephemeris from § 5).

Udalski et al. (2002) Acta Astron., 52, 115.
Torres et al. (2004) ApJ, 609, 1071.

The Transisting CGEP OGLE-TR-113

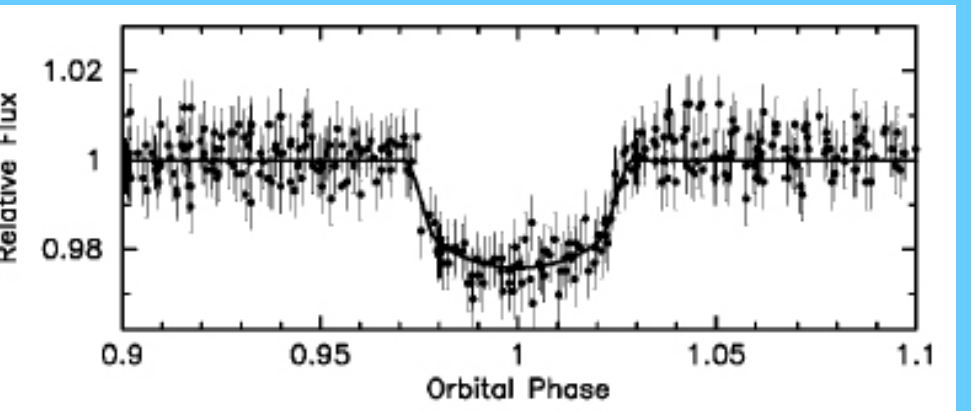

FIG. 4.—OGLE photometry for OGLE-TR-113 in the *I* band, with our best-transit light curve. The resulting parameters are listed in Table 2.

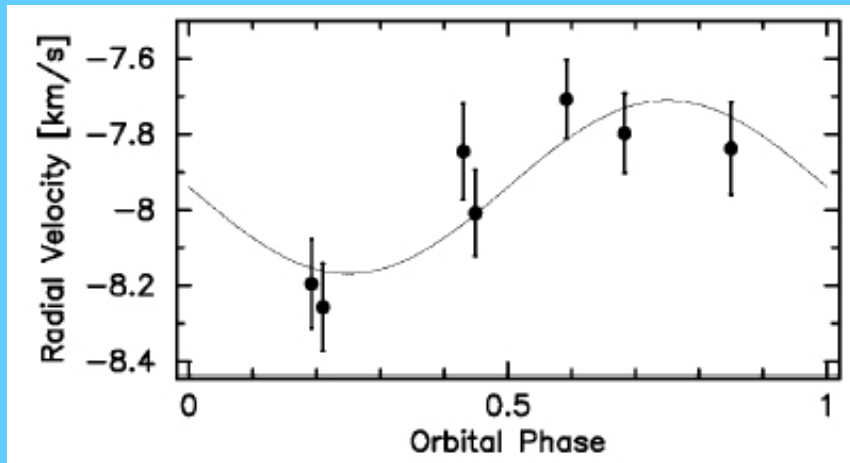

FIG. 2.—Radial velocity measurements and fitted velocity curve for OGLE TR-113, as a function of orbital phase. Only the semiamplitude and center of-mass velocity have been adjusted. The transit ephemeris is adopted from the photometry (see text).

Konacki et al. (2004) ApJ. 609, L37.

TABLE 1

DATA FOR CURRENT LIST OF TRANSITING EGPS

EGP	M_* ($M_\odot$)	R_* ($R_\odot$)	a (AU)	P (days)	M_p (M_J)	R_p (R_J)	Age (Gyr)
HD 209458b[a]	1.1 ± 0.1	1.2 ± 0.1	0.045	3.525	0.69 ± 0.05	1.4 ± 0.17	5.5 ± 1.5
HD 209458b[b]	1.06 ± 0.1	1.18 ± 0.1	0.045	3.525	0.69 ± 0.02	$1.42^{+0.12}_{-0.13}$	5.2 ± 0.5
HD 209458b[c]	1.1 ± 0.1	1.146 ± 0.05	0.045	3.525	~0.69	1.347 ± 0.06	...
OGLE-TR-56b[d]	1.04 ± 0.05	1.1 ± 0.1	0.0225	1.212	1.45 ± 0.23	1.23 ± 0.16	$2.5^{+1.5e}_{-1.0}$
OGLE-TR-113b[f]	0.77 ± 0.06	0.765 ± 0.025	0.0228	1.433	1.35 ± 0.22	$1.08^{+0.07}_{-0.05}$	...
OGLE-TR-113b[g]	0.79 ± 0.06	0.78 ± 0.06	0.023	1.432	1.08 ± 0.28	1.09 ± 0.10	...
OGLE-TR-132b[f]	1.34 ± 0.1	$1.41^{+0.49}_{-0.10}$	0.0306	1.689	1.01 ± 0.31	$1.15^{+0.80}_{-0.13}$	...

[a] Mazeh et al. (2000).
[b] Cody & Sasselov (2002).
[c] Brown et al. (2001).
[d] Torres et al. (2003).
[e] Sasselov (2003).
[f] Bouchy et al. (2004).
[g] Konacki et al. (2004).

Burrows et al. (2004) ApJ, 610, L53.

Exo-Kuiper Belt Dust Complexes

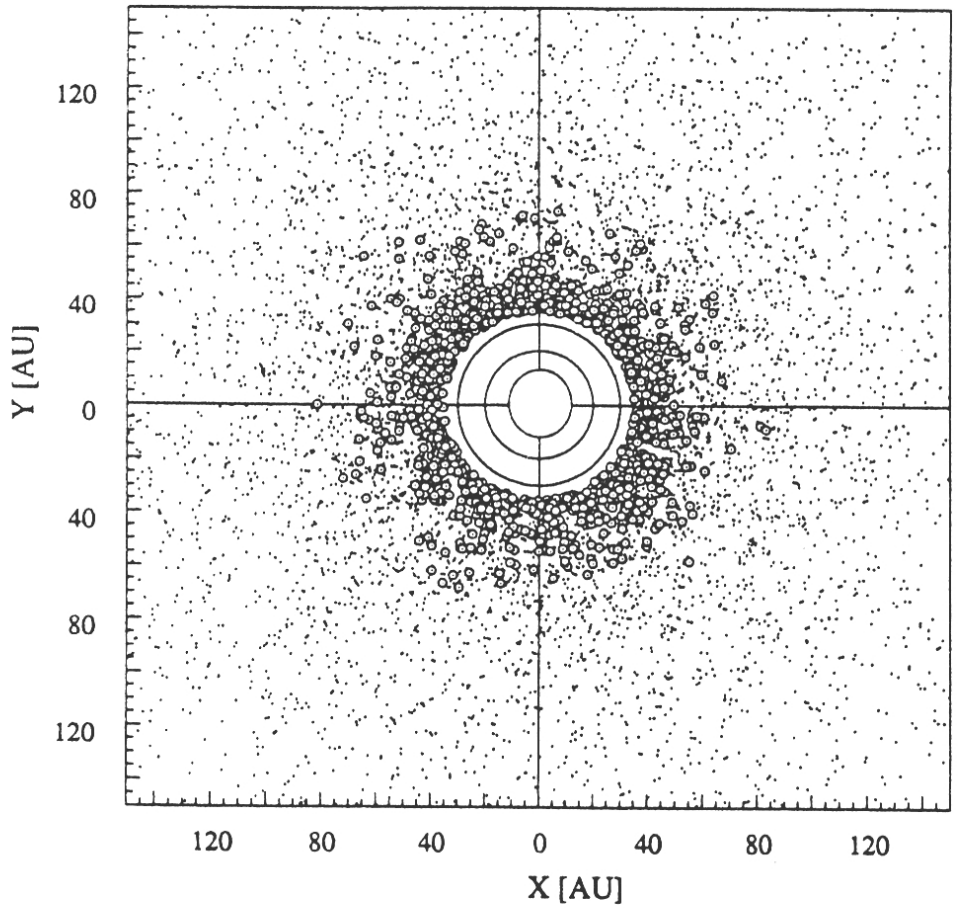

FIG. 6. Plan view of the Monte Carlo simulation in Fig. 5. Objects generated by the simulation are plotted as points, while objects that satisfy the detection criteria of the Mauna Kea survey are marked as circles.

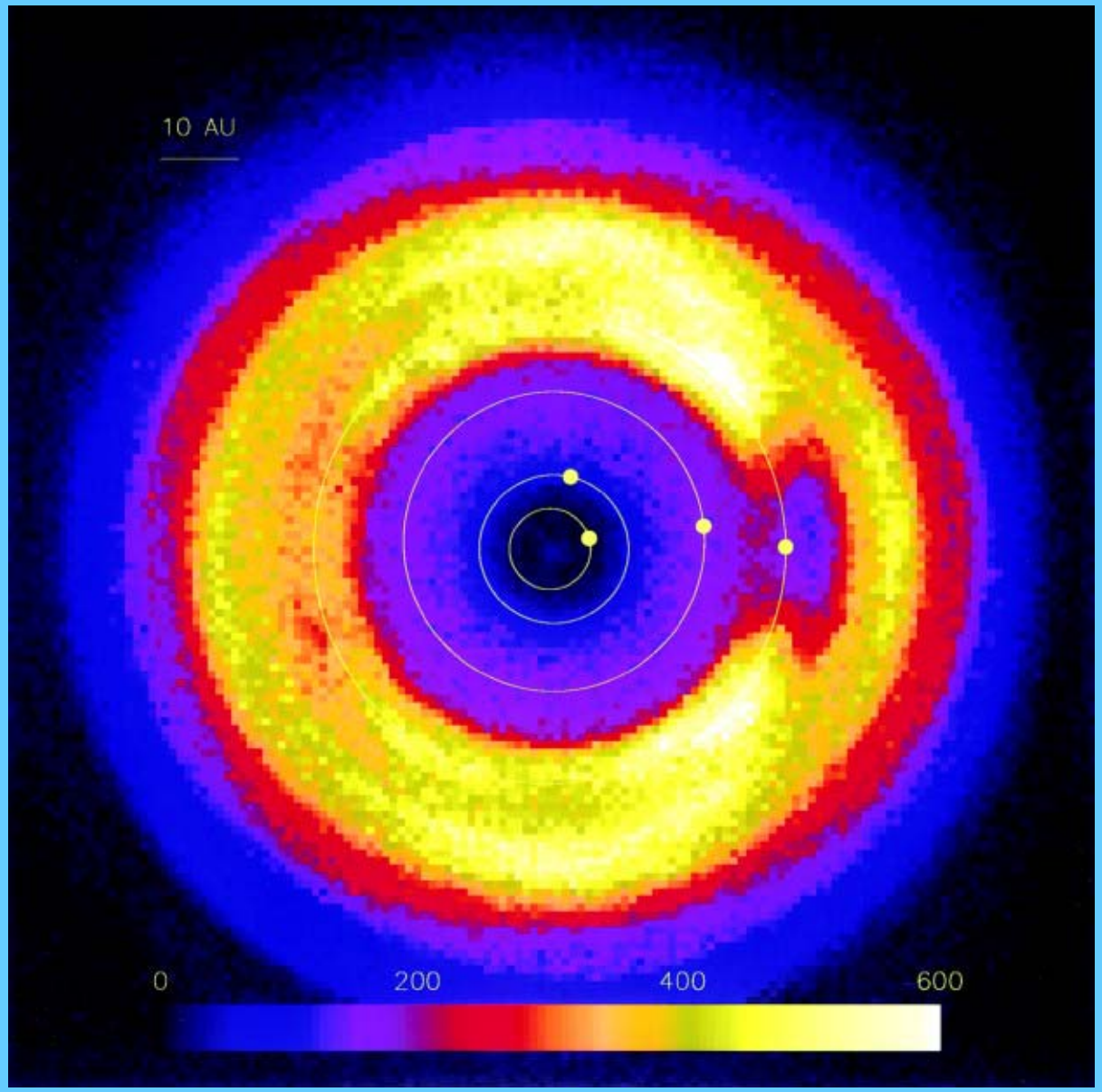
10 AU
0
200
400
600

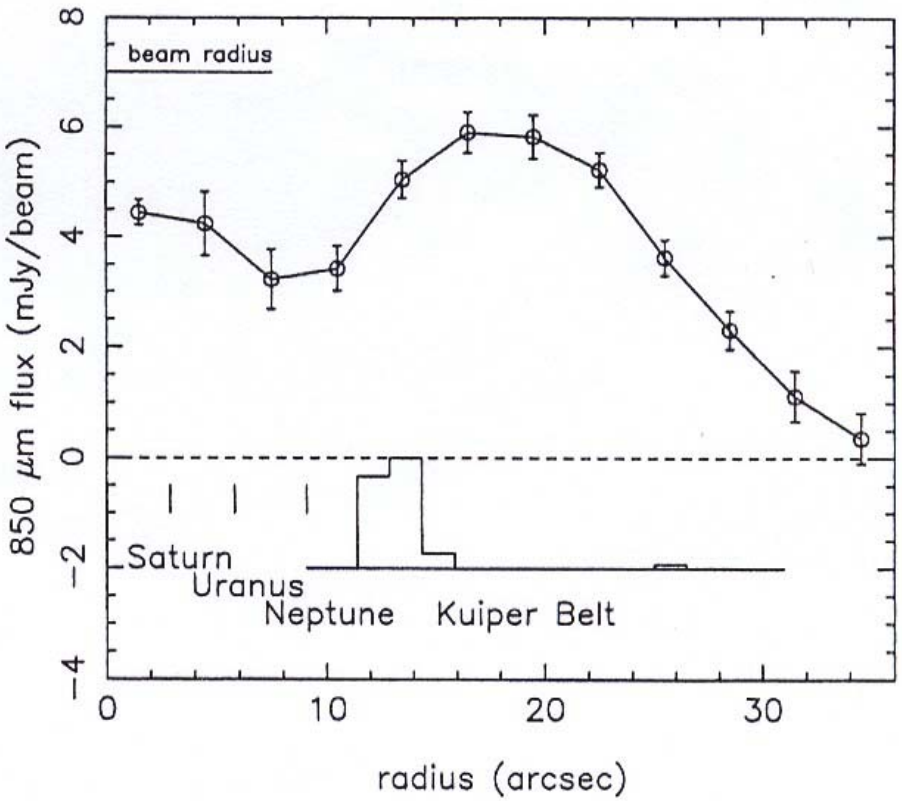

FIG. 2.—Radial profile of dust emission around ϵ Eri. The mean 850 μm flux density (in units of mJy beam^{-1}) is plotted against the radial distance from the star. The data are averaged in 3″ bins, to match the raw image sampling, and the error bars represent the standard error of the mean from the dispersion of signals at that radius. For comparison, the number of known Kuiper Belt objects is plotted underneath as a function of the semimajor axis, together with the locations of the outer planets.

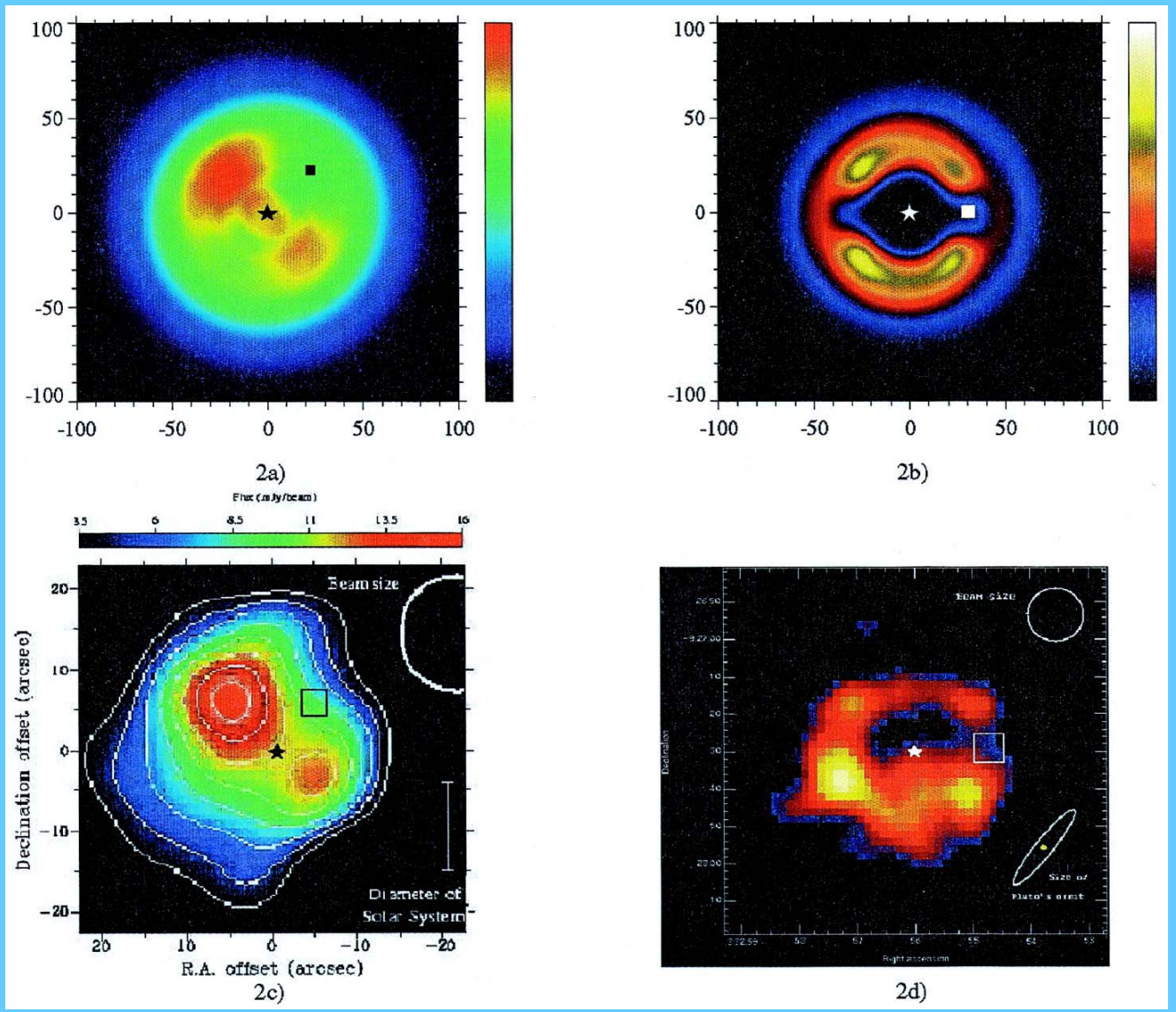

L.M. Ozerrnoy et al. (2000) ApJ, 537, L147-L151.

Direct detection of brown dwarf (and exoplanets?)

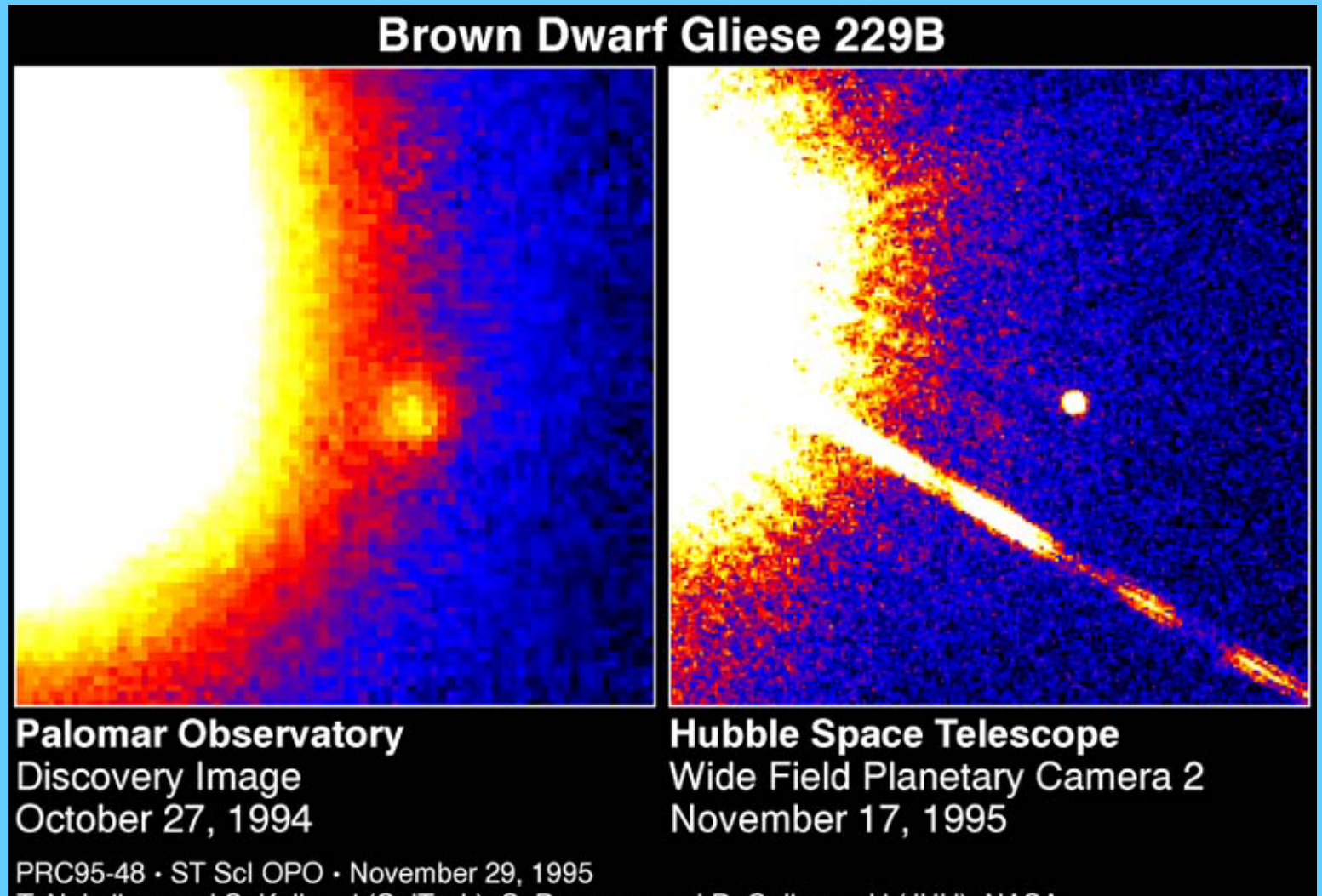

The Daily Yomiuri – Sept. 15, 2004

WASHINGTON (Reuter) - Blurry image might be first picture of exoplanet.

Exoplanet candidate of 5 MJ possibly orbiting at distance of 55 AU around brown dwarf 2M1207 at 70 pc from Earth.

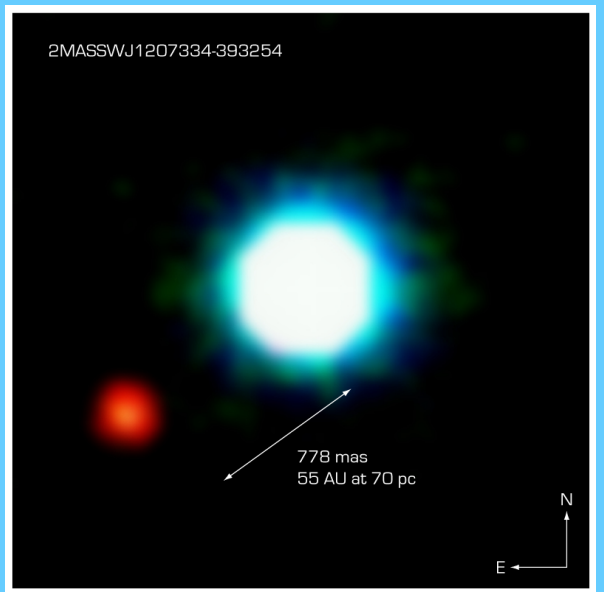

NACO Image of the Brown Dwarf Object 2M1207 and GPCC

ESO PR Photo 26a/04 (10 September 2004) © European Southern Observatory

Detection with future space observatories

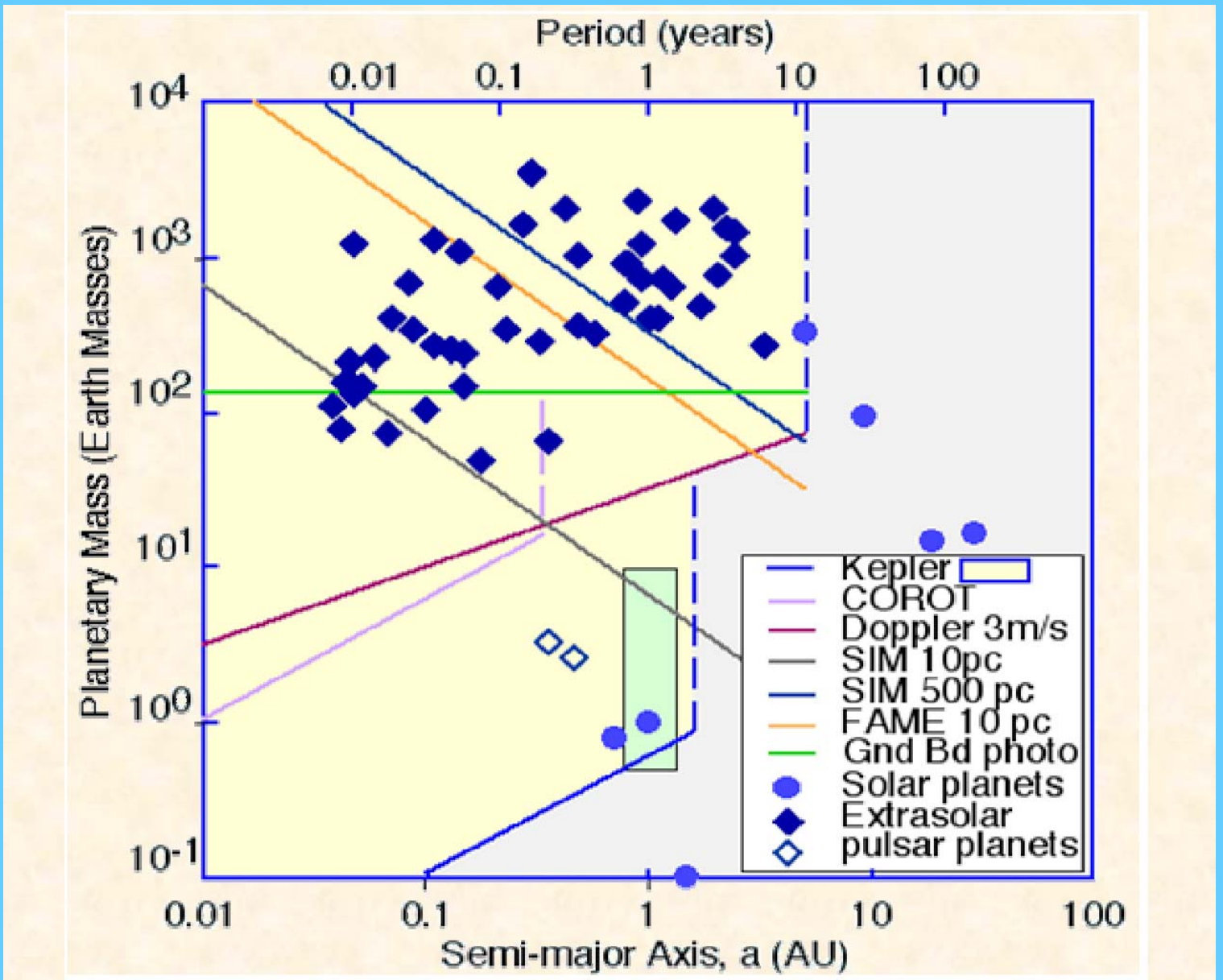

Some Observational Statistics

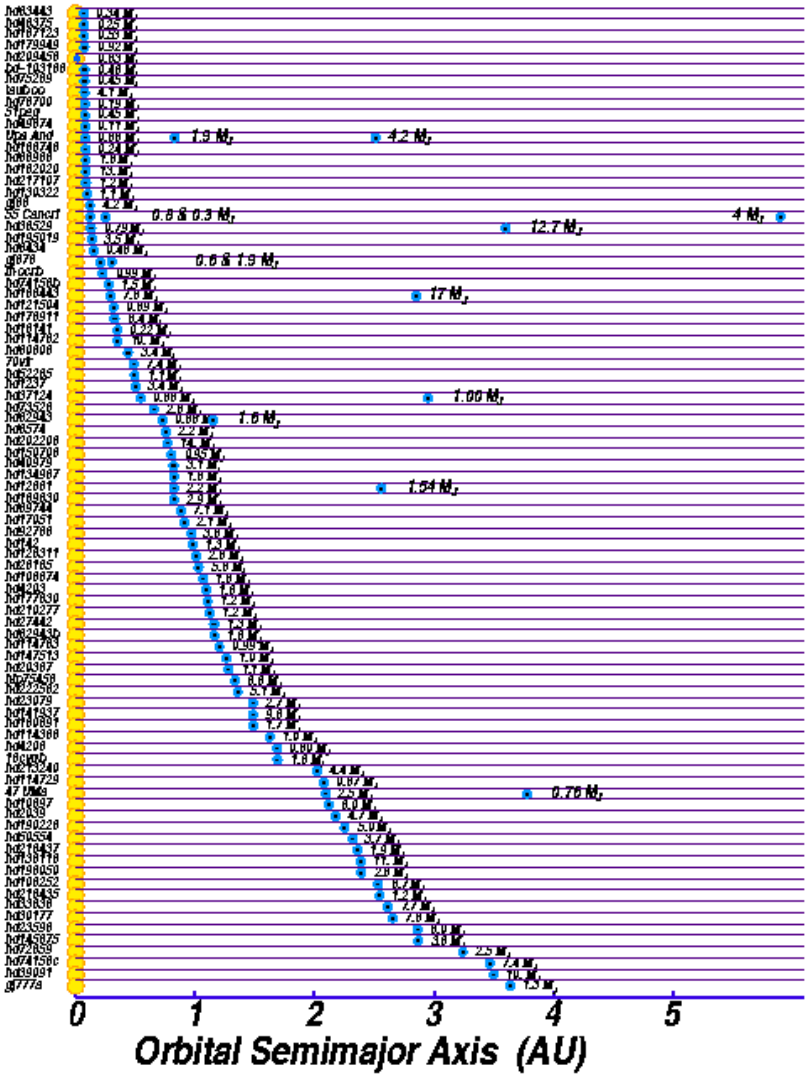
1.9 M,
4.2 M,
0.6 & 0.3 M,
12.7 M,
4 M,
0.6 & 1.9 M,
17 M,
1.00 M,
1.6 M,
1.54 M,
0.76 M,
0
1
2
3
4
5
Orbital Semimajor Axis (AU)

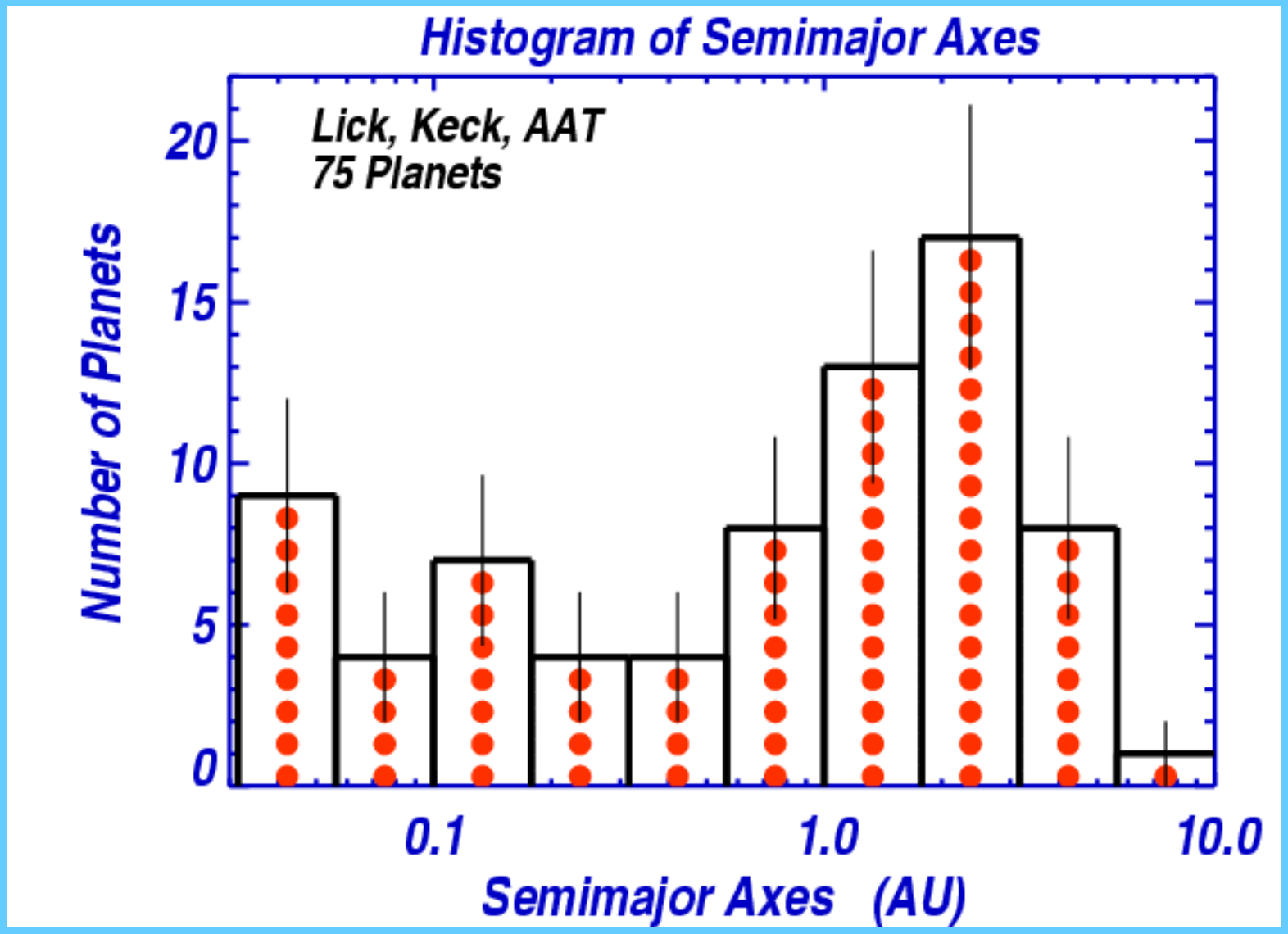
Histogram of Semimajor Axes
Lick, Keck, AAT
75 Planets
Number of Planets
20
15
10
5
0
0.1
1.0
10.0
Semimajor Axes (AU)

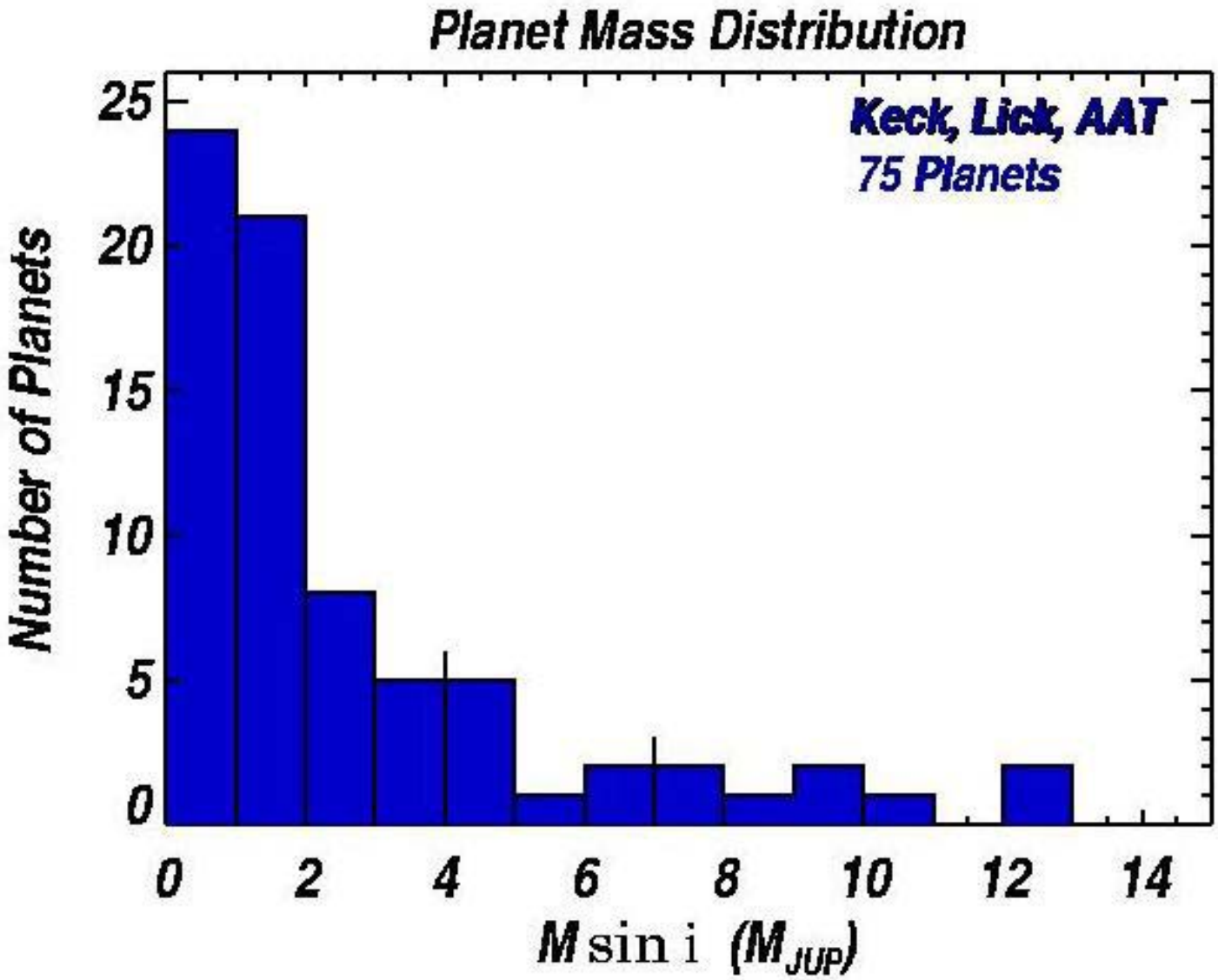
Planet Mass Distribution
Keck, Lick, AAT
75 Planets
Number of Planets
25
20
15
10
5
0
0
2
4
6
8
10
12
14
M sin i (M_JUP)

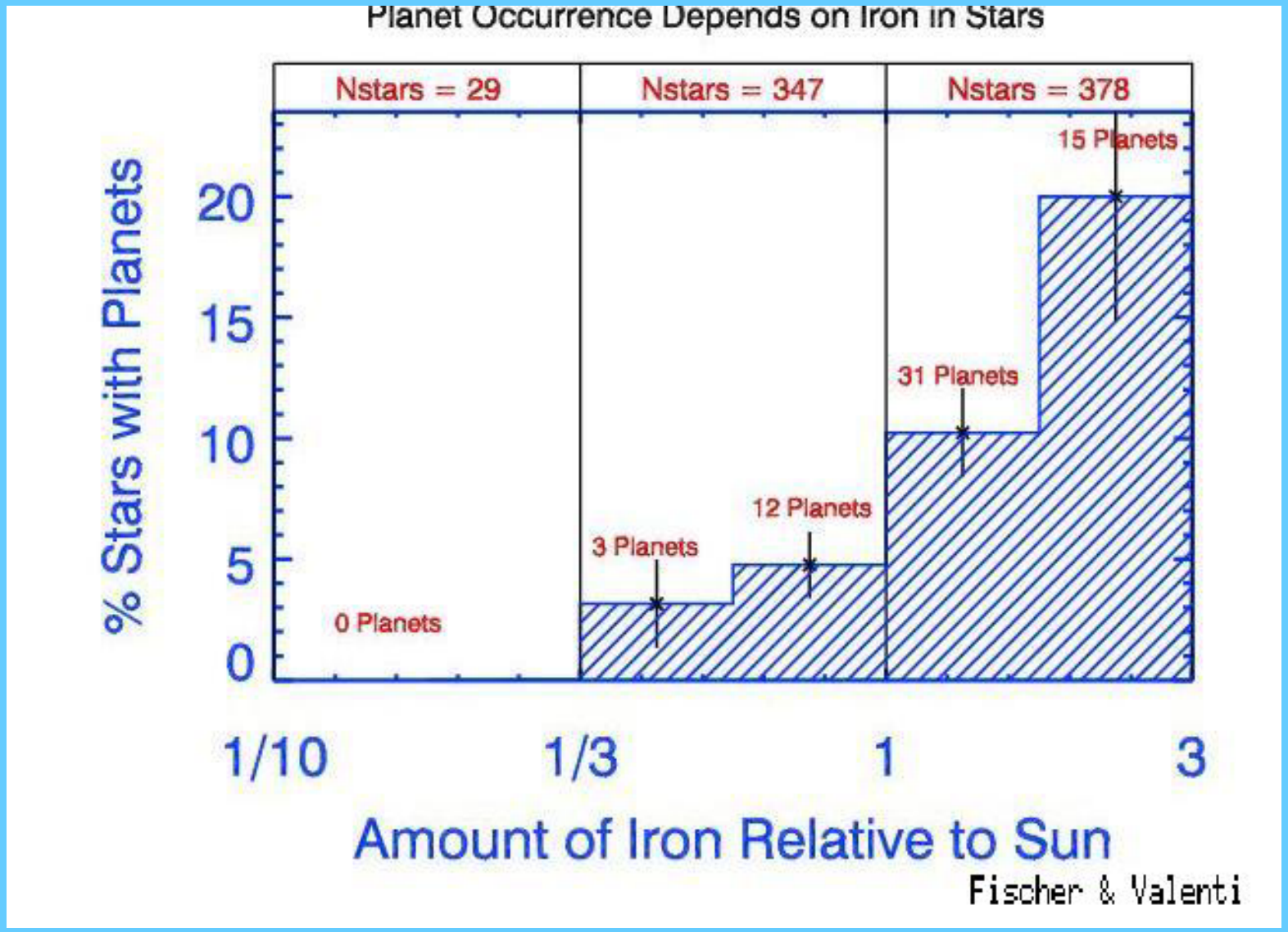
Planet Occurrence Depends on Iron in Stars
Nstars = 29
Nstars = 347
Nstars = 378
15 Planets
31 Planets
12 Planets
3 Planets
0 Planets
% Stars with Planets
0
5
10
15
20
1/10
1/3
1
3
Amount of Iron Relative to Sun
Fischer & Valenti

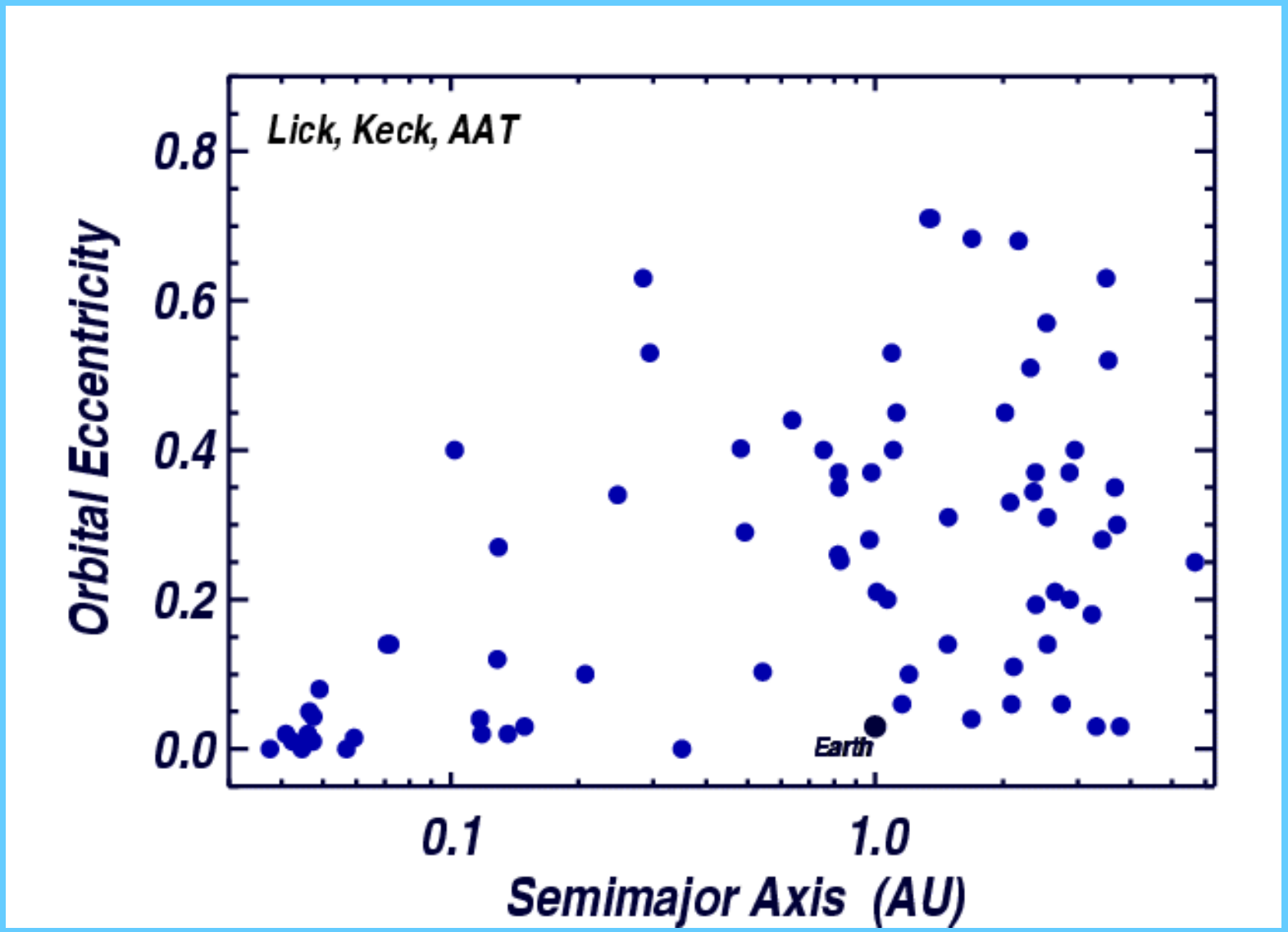
Lick, Keck, AAT
Earth
Orbital Eccentricity
0.0
0.2
0.4
0.6
0.8
0.1
1.0
Semimajor Axis (AU)

Why are the orbital eccentricities so large?

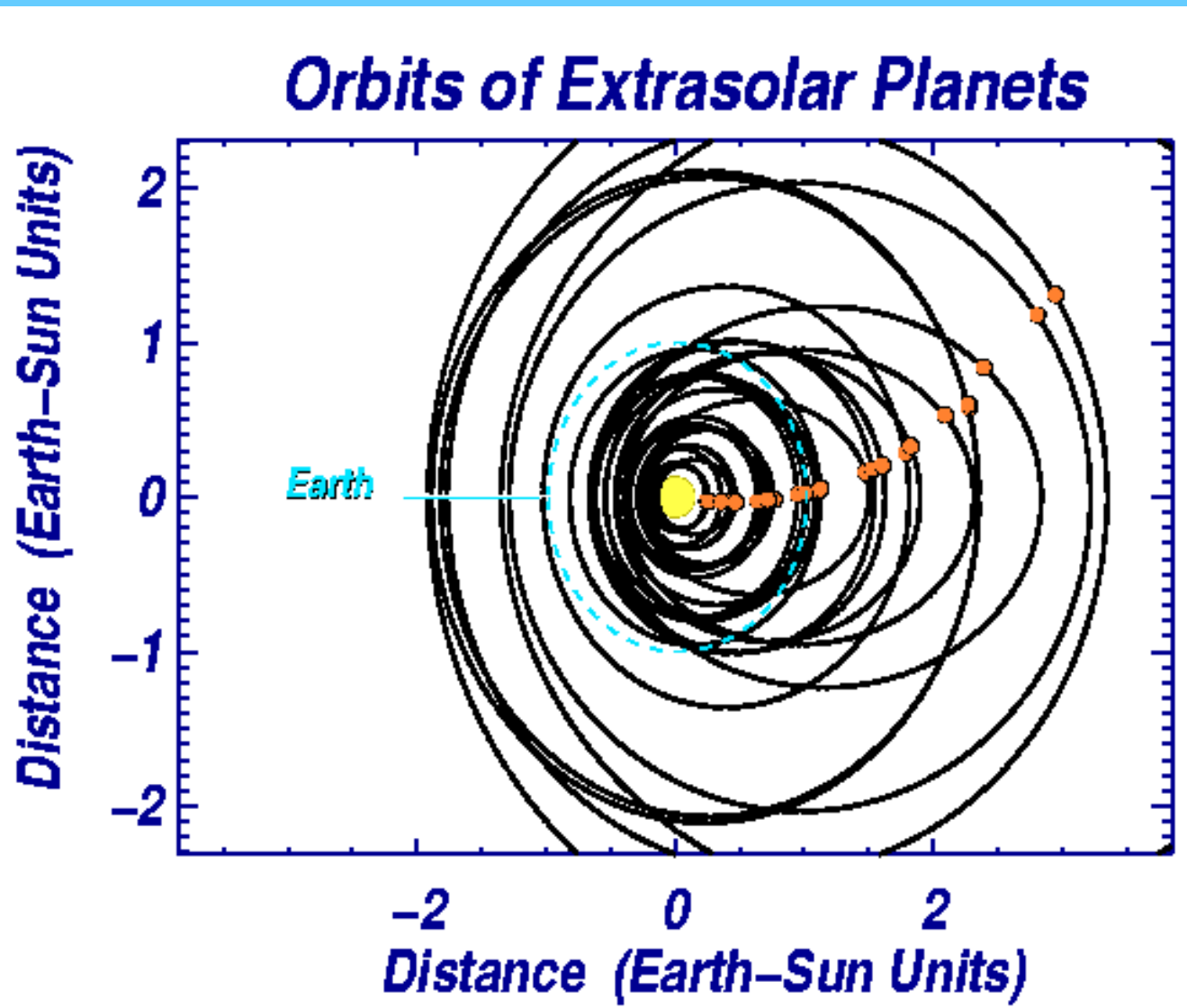
Orbits of Extrasolar Planets
Distance (Earth–Sun Units)
2
1
0
–1
–2
Earth
–2
0
2
Distance (Earth–Sun Units)

Orbital Scattering Mechanisms

- Disk-Planet interaction
- Orbital scattering by passing stars
- Planet-planet interaction
- ……

Star Cluster - NGC 381

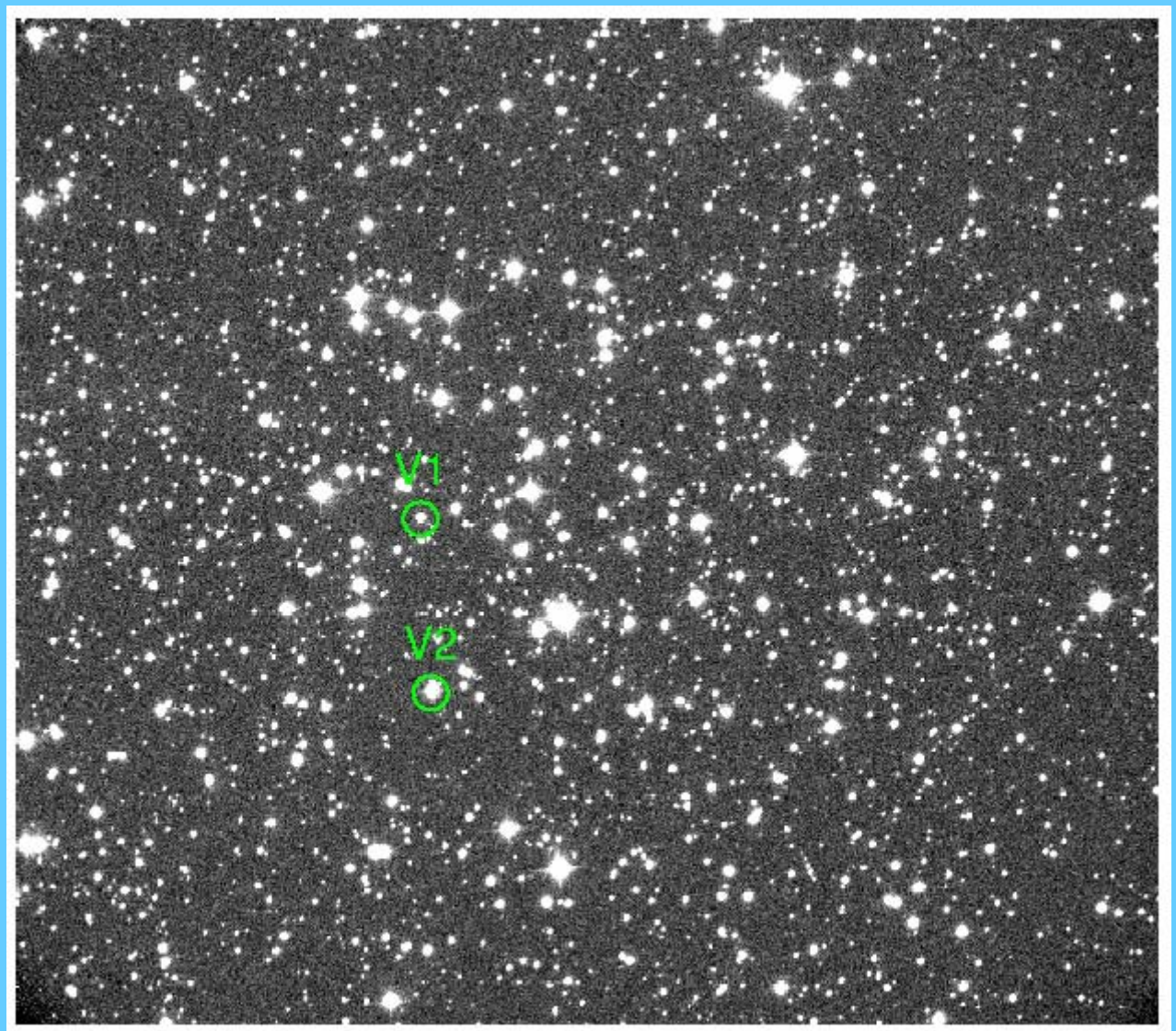

Gravitational Scattering or Too Close for Comfort

•For orbital spacing

$$\Delta a < 2\sqrt{3} R_H$$

$$R_H = \left[\frac{(m_1+m_2)}{3M}\right]^{1/3} \left(\frac{a_1+a_2}{2}\right)$$

➠ Orbital instability

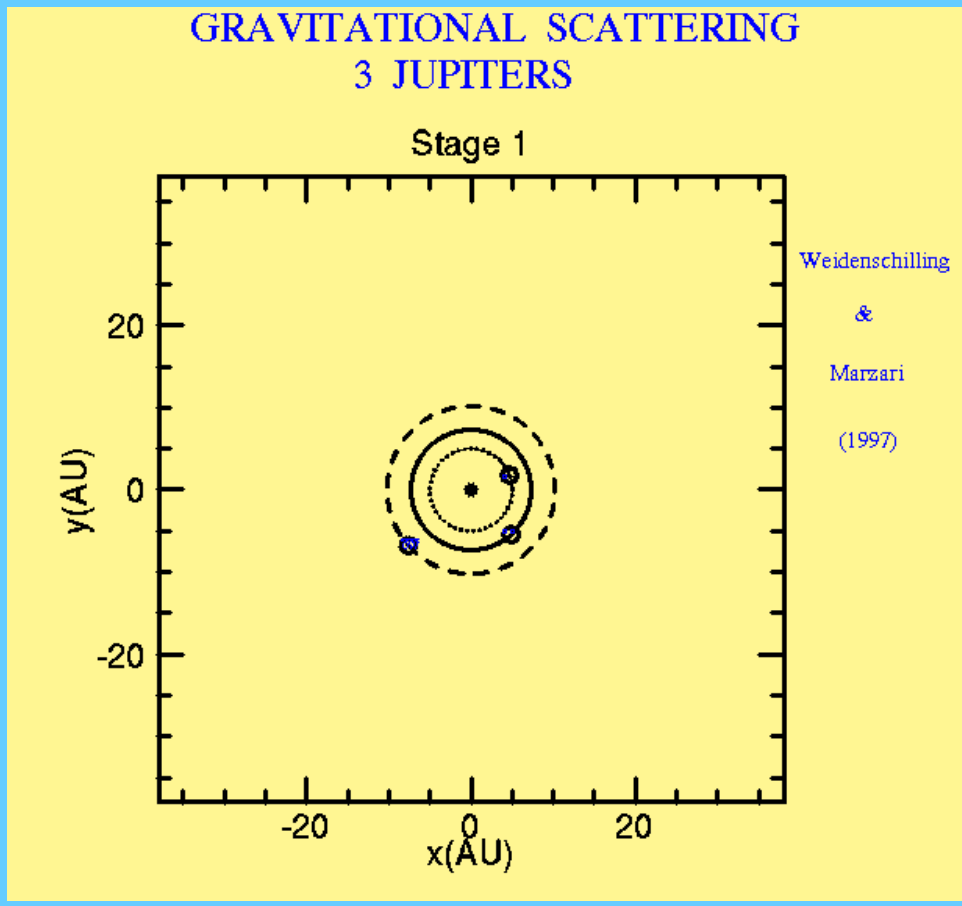

Weidenschilling and Marzari. (1997) Nature, 384, 619.

Gravitational Scattering as a Possible Origin for the Giant Planets at Small Stellar Distances

Weidenschilling and Marzari 1996, Nature, v384, p619

a system of three or more giant planets form about a star, their orbits may become unstable as they ain mass by accreting gas from the circumstellar disk; subsequent gravitational encounters among ese planets can eject one from the system while placing the others into highly eccentric orbits both oser and farther from the star.

GRAVITATIONAL SCATTERING

3 JUPITERS

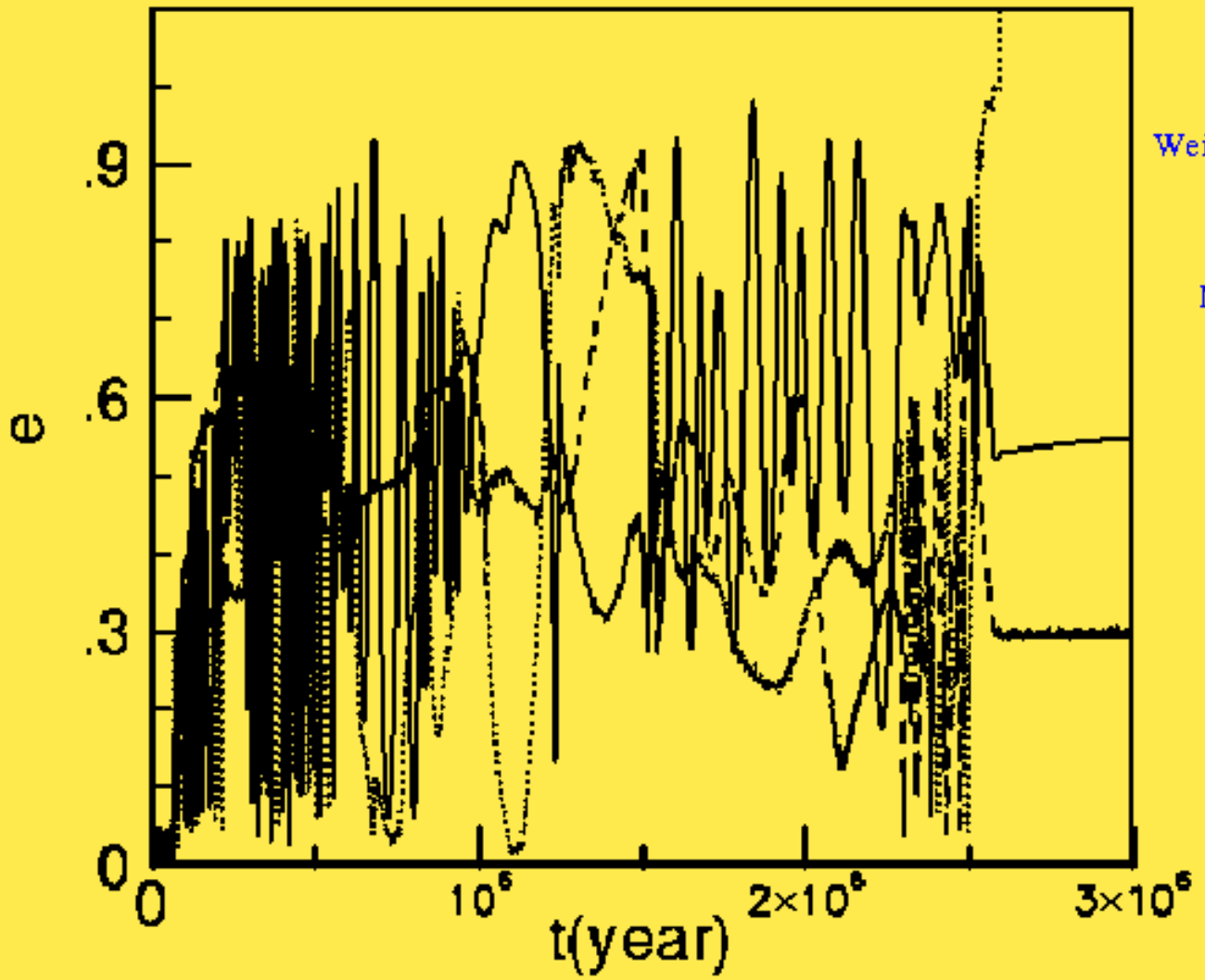

Weidenschilling

&

Marzari

(1997)

How about the close-in "Hot Jupiters"?

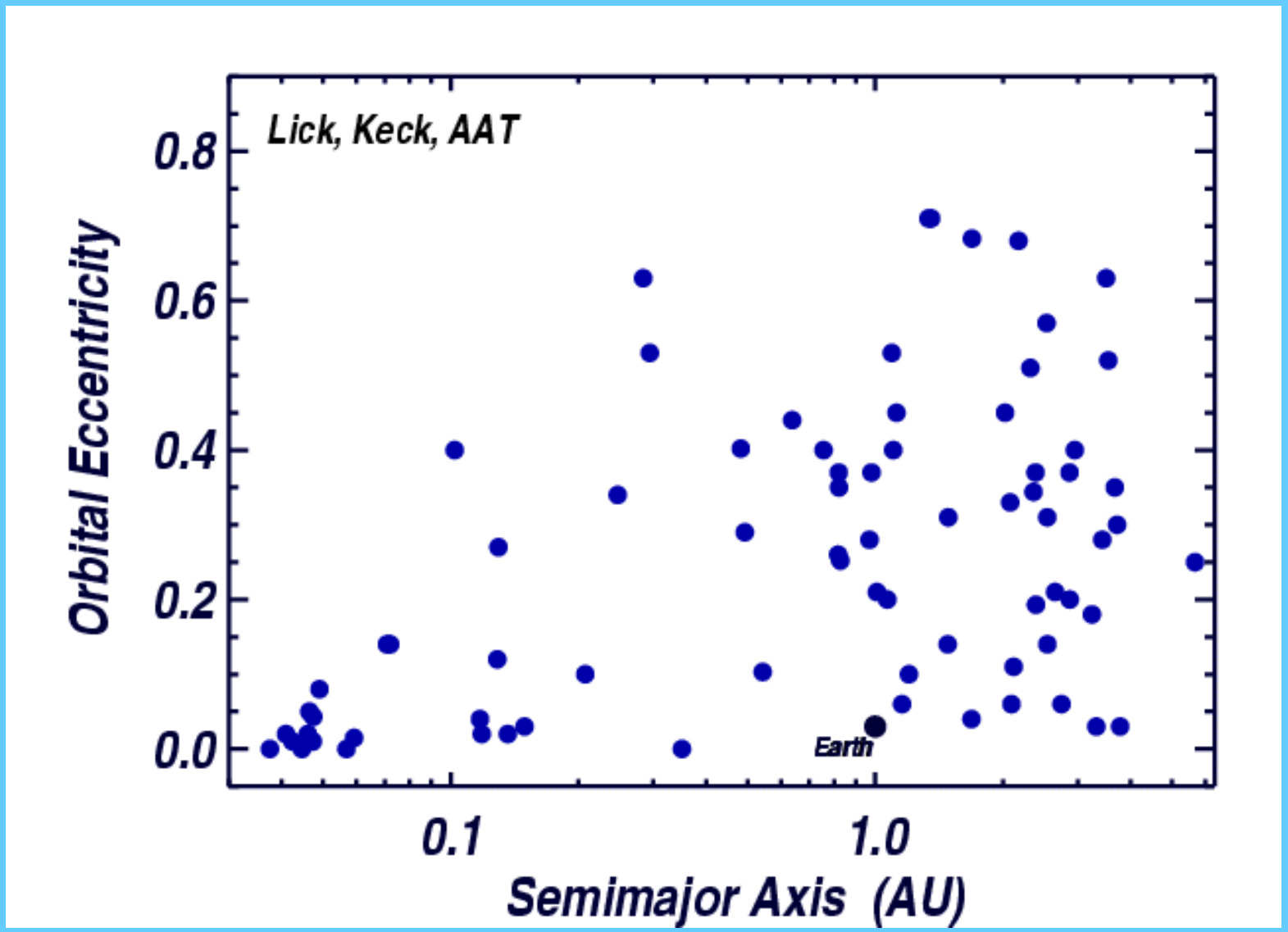
Lick, Keck, AAT
Earth
Orbital Eccentricity
0.0
0.2
0.4
0.6
0.8
0.1
1.0
Semimajor Axis (AU)

Orbital Migration in Solar Nebula

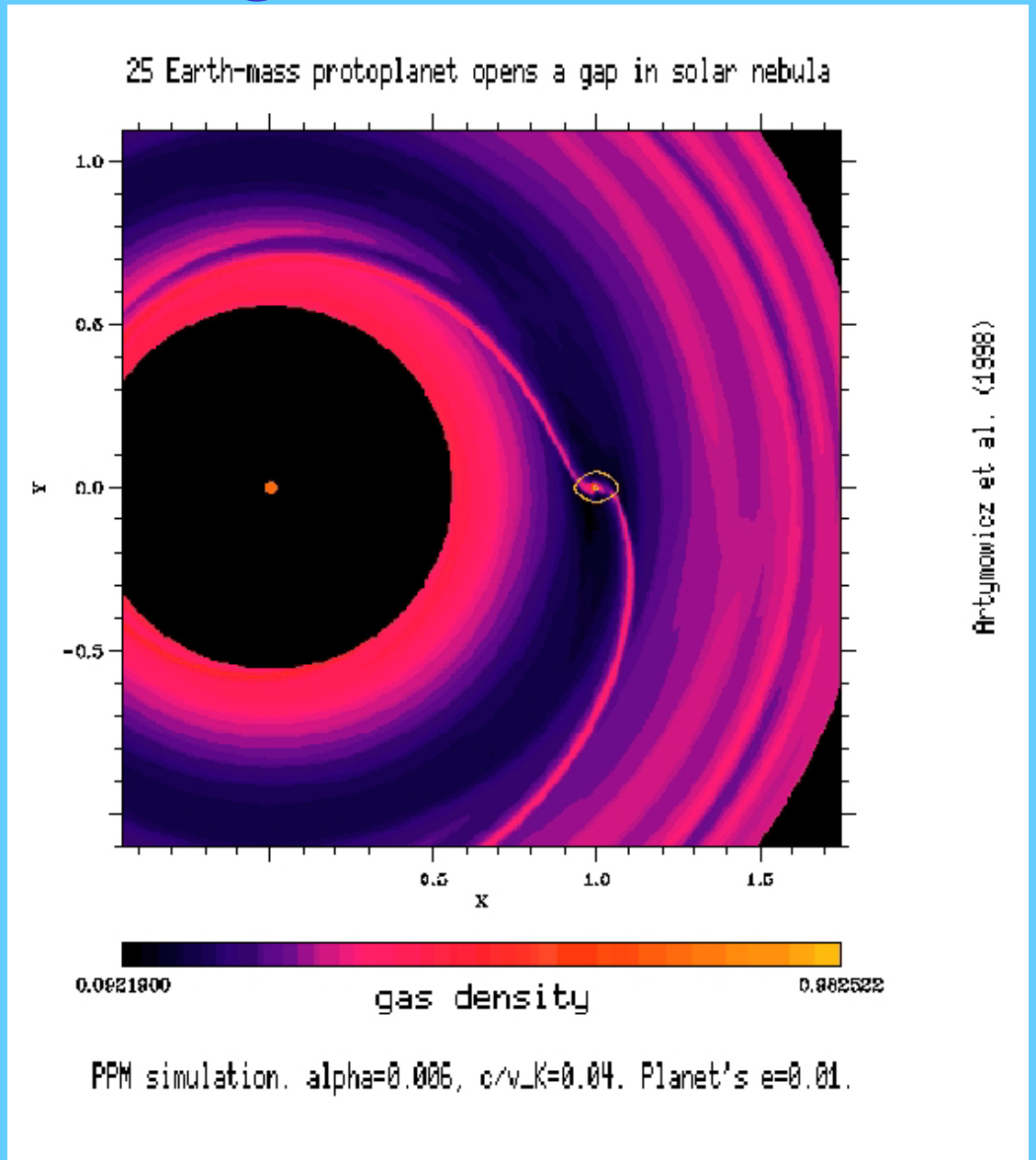

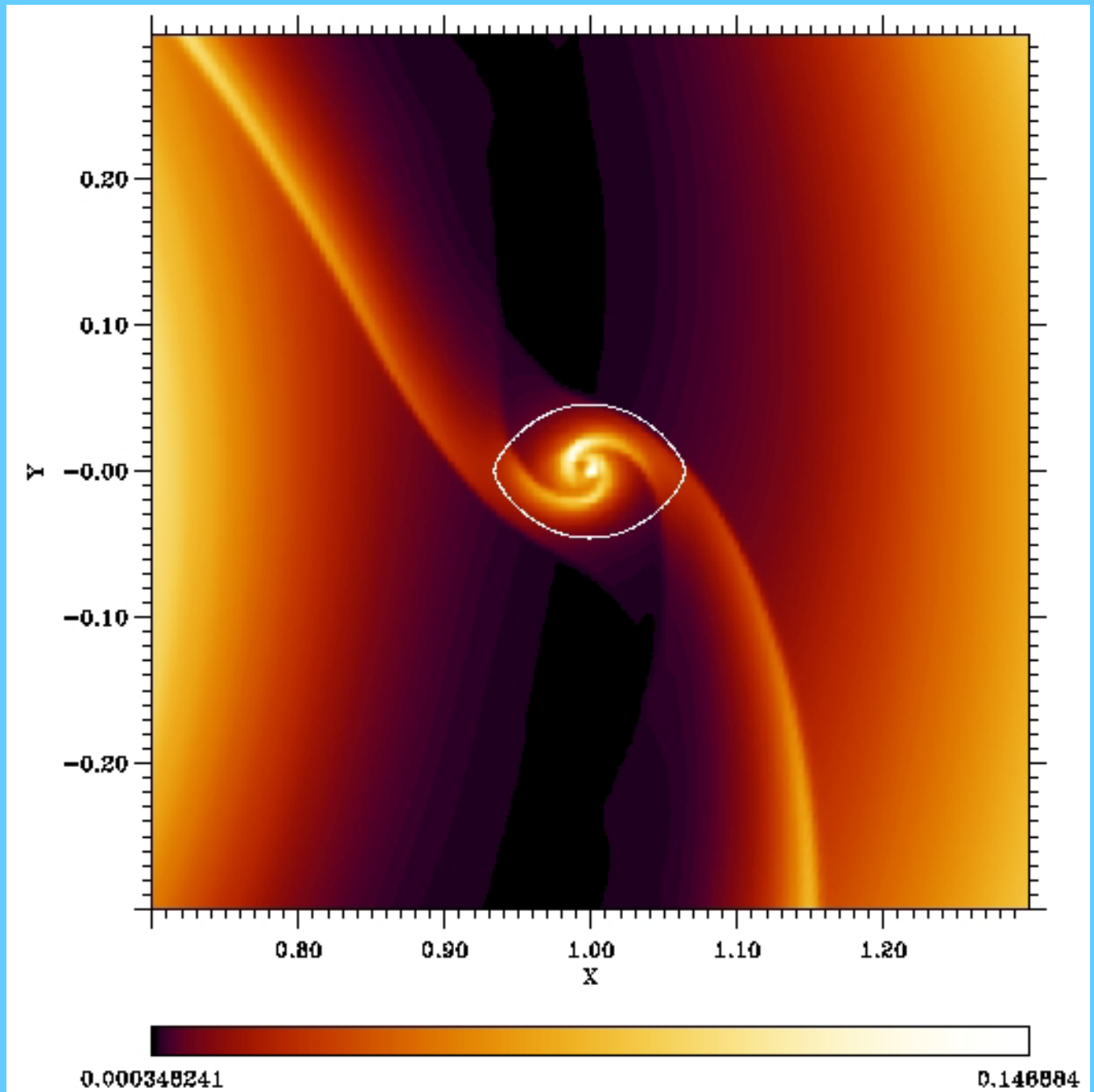
0.20
0.10
−0.00
−0.10
−0.20
Y
0.80
0.90
1.00
1.10
1.20
X
0.000348241
0.146884

Orbital Evolution of CEGPs

$e = 0$

$$\frac{da}{dt} = \text{sign}\,(\Omega - n)\frac{3k}{Q}\frac{m}{M}\left(\frac{R}{a}\right)^5 na$$

$e \neq 0$

$$\frac{da}{dt} = 3k\frac{Gm^2}{a^7}\frac{R^5}{Qn}\frac{M+m}{Mm}\left(n - \Omega\sqrt{1-e^2}\right)^{-1} \times \left[\Omega - \frac{\sqrt{G(M+m)a(1-e^2)}}{a^2(1-e\cos nt)^2}\right],$$

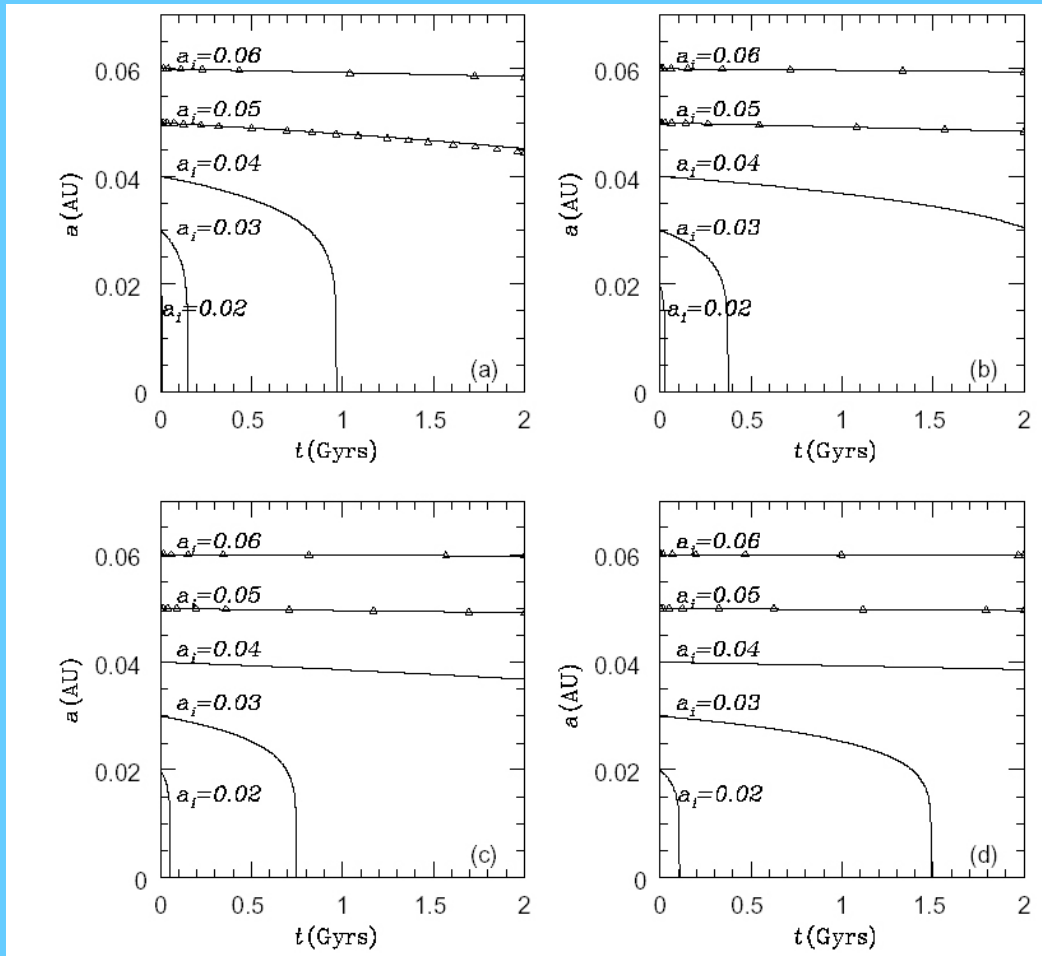

FIG. 1.—Semimajor axes as a function of time. The solid curves are the result of $e = 0$ and initial semimajor axis $a_i = 0.02,\ 0.03,\ \ldots,\ 0.06$. The trian
are the result of $e = 0.5$ and $a_i = 0.05,\ 0.06$. Planetary mass is (*a*) 5 M_J, (*b*) 2 M_J, (*c*) M_J, and (*d*) 0.5 M_J.

Paetzold &Rauer (2002) ApJ, 568, L117.
Jiang et al. (2003) ApJ, 582, 449

Exoplanets II

Evolution of Earth-like Exoplanets

- Terrestrial ocean = 1.4×10^{24} g
- Terrestrial atmosphere = 5.1×10^{21} g
- Gradual warming by solar irradiation ➠ H_2O Evaporation from Ocean in 1 Gyr.
- Possibility of total evaporation in 3 Gyr as $L_\odot \sim 1.4 L_\odot^{(now)}$
- Venus – like stellar wind interaction with atomic hydrogen tail from photodissociation of H_2O.
- Ask Dr. George Hashimoto!

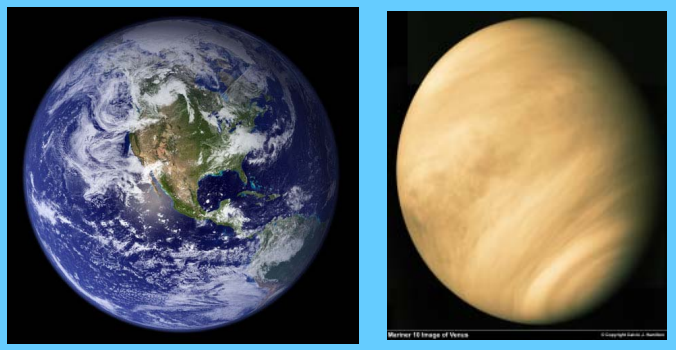

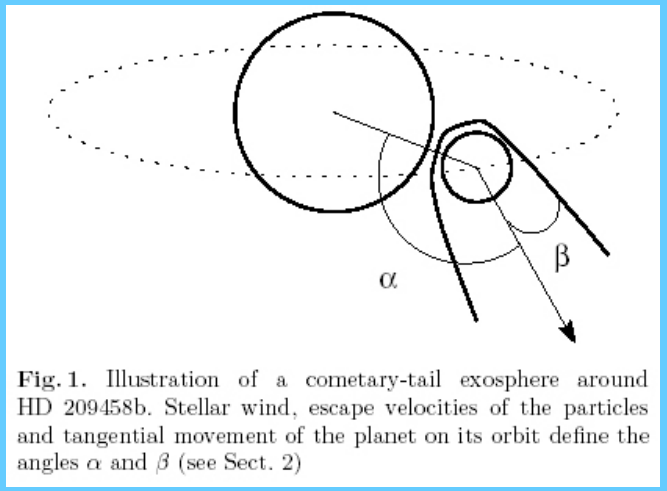

Fig. 1. Illustration of a cometary-tail exosphere around HD 209458b. Stellar wind, escape velocities of the particles and tangential movement of the planet on its orbit define the angles α and β (see Sect. 2)

Jura(2004), ApJ, 605, L65.
Moutou et al(2001), A&A, 371, 260.

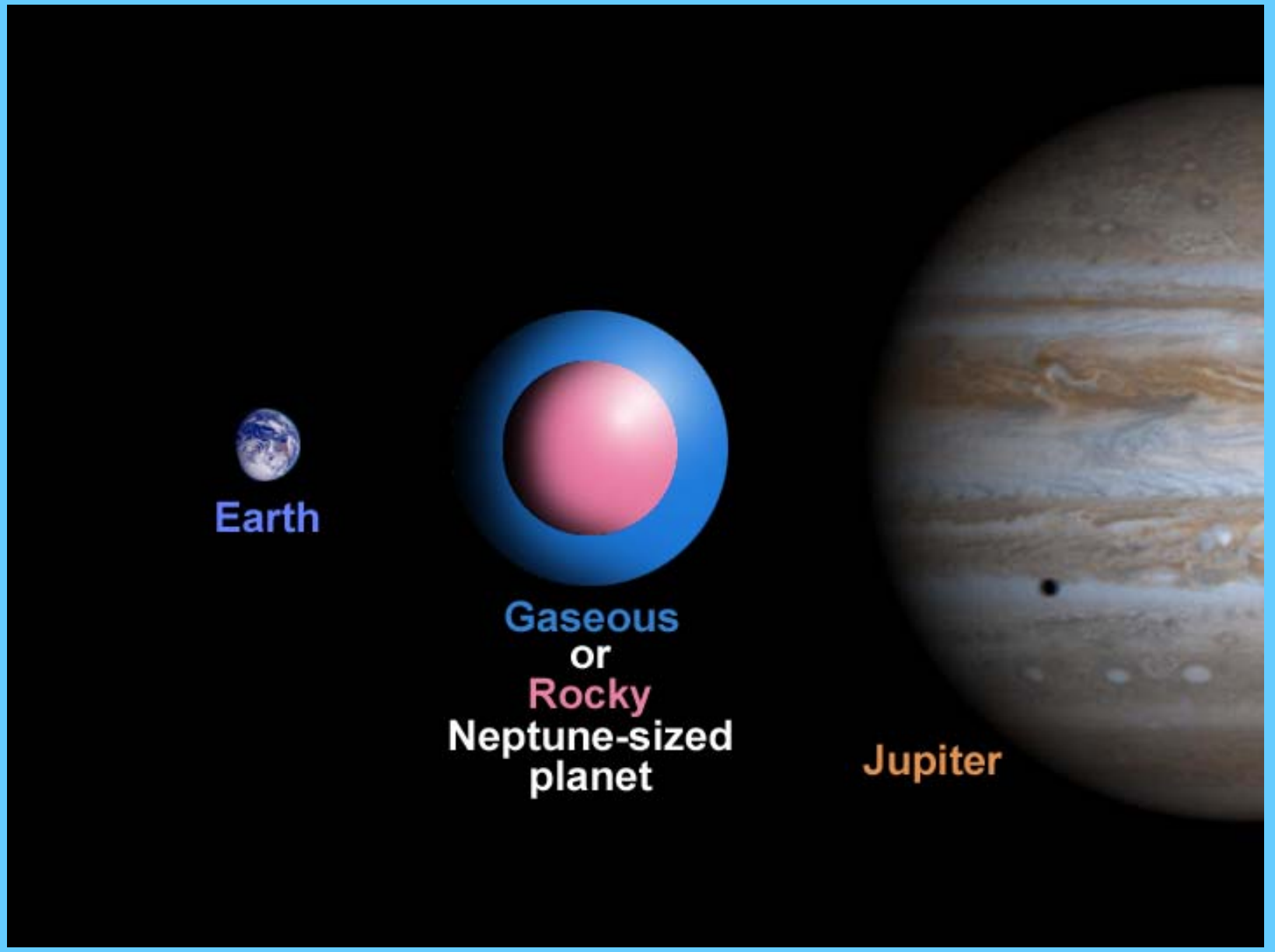
Earth
Gaseous
or
Rocky
Neptune-sized
planet
Jupiter

Ocean Planets – A New Family of Exoplanets

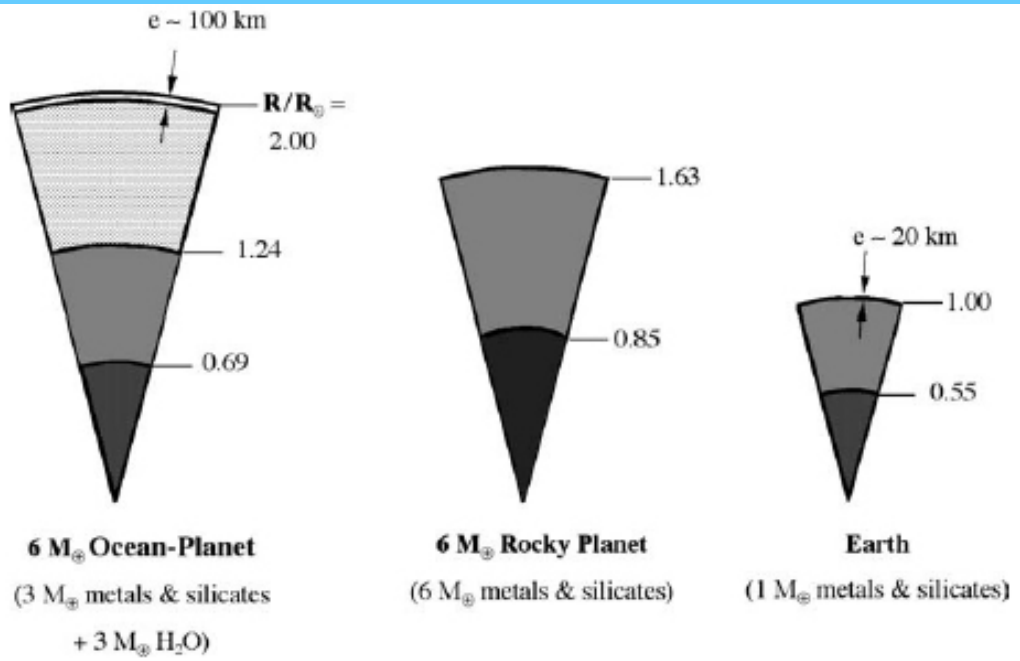

Fig. 1. From left to right: (1) calculated internal structure of a $6M_\oplus$ Ocean-Planet. Constituents are, from the centre to the outside, $1M_\oplus$ metals, $2M_\oplus$ silicates, and $3M_\oplus$ ice. The density (g cm^{-3}) at the centre, different interfaces and top is: 19.5, 15.6–8.2, 6.2–3.9, and 1.54; gravity ($g_\oplus$): 0, 2.1, 1.96, and 1.54; pressure (GPa): 1580, 735, 250, and ~ 1. The upper layer is a ~ 100 km thick ocean. The mean planetary density is 4.34 g cm^{-3}; (2) idem for a rocky planet with the same total mass ($2M_\oplus$ metals, $4M_\oplus$ silicates). Density is: 21.0, 15.5–8.1, and 4.1; gravity: 0, 2.72, and 2.24; pressure: 2200, 745, and 0. The mean planetary density is 7.74 g cm^{-3}; (3) for comparison, the structure of the Earth calculated with the same model is shown. It agrees fairly well with the actual one. Density is: 13, 9.5–5.2, 3.3; gravity: 0, 1.04, 1.00; pressure: 340, 130, 0. The mean planetary density is 5.57 g cm^{-3}.

Leger et al. (2004) Icarus 169, 499.

Oceanic Exoplanets in Habitable Zone

Icy planets ($0.1 - 10 M_{\oplus}$) with half olatiles and half rocks material(like the ovian moons). Inward orbital migration f volatile (H_2O) – rich protoplanets into he "habitable zone"

Atmospheric Greenhouse Temperature

$T_G = \lambda^{1/4} T_{BB}$ **(surface blackbody temperature)**

($\lambda \sim 31$ for Venus with $T_G = 2.4 * T_{BB}$)

$T_G < 647K$ (Hot Steam Ocean)

$T_G > 647K$ (Massive evaporation)

EUV – driven atmospheric loss

$$\dot{M} = 4\pi m F_{esc}$$
$$F_{esc} = s r_0^3 / GMm$$
$$s = 1\ ergs\ cm^{-2} (a/1AU)(t/4.5 \times 10^9 yr)^-$$

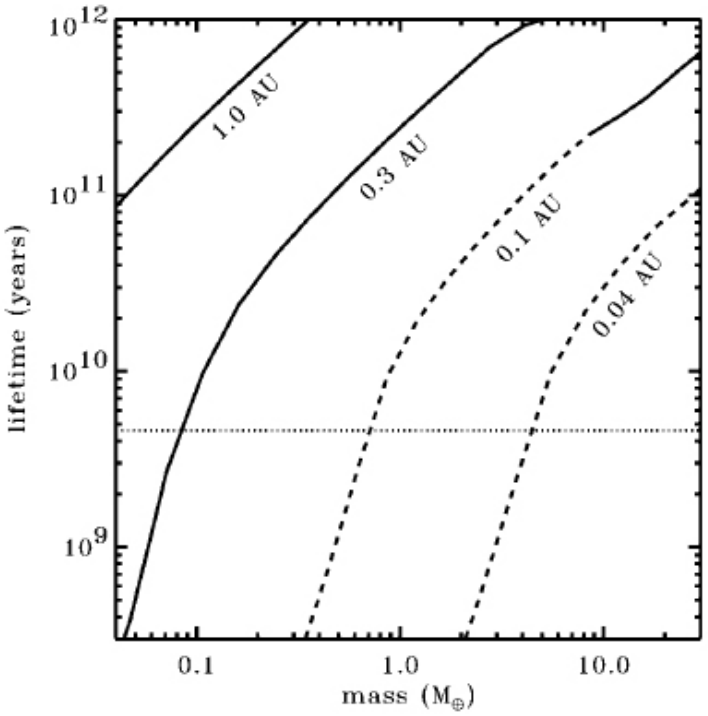

FIG. 1.—Survival time for EUV-driven atmospheric escape as a function of mass for volatile planets at 1, 0.3, 0.1, and 0.04 AU. The curves become dashed where the atmosphere becomes ≥10% of the planet's mass. The dotted line shows the age of the solar system.

Kuchner(2003), ApJ, 596, L105.

Matsui & Abe(1986), Nature, 322, 526.

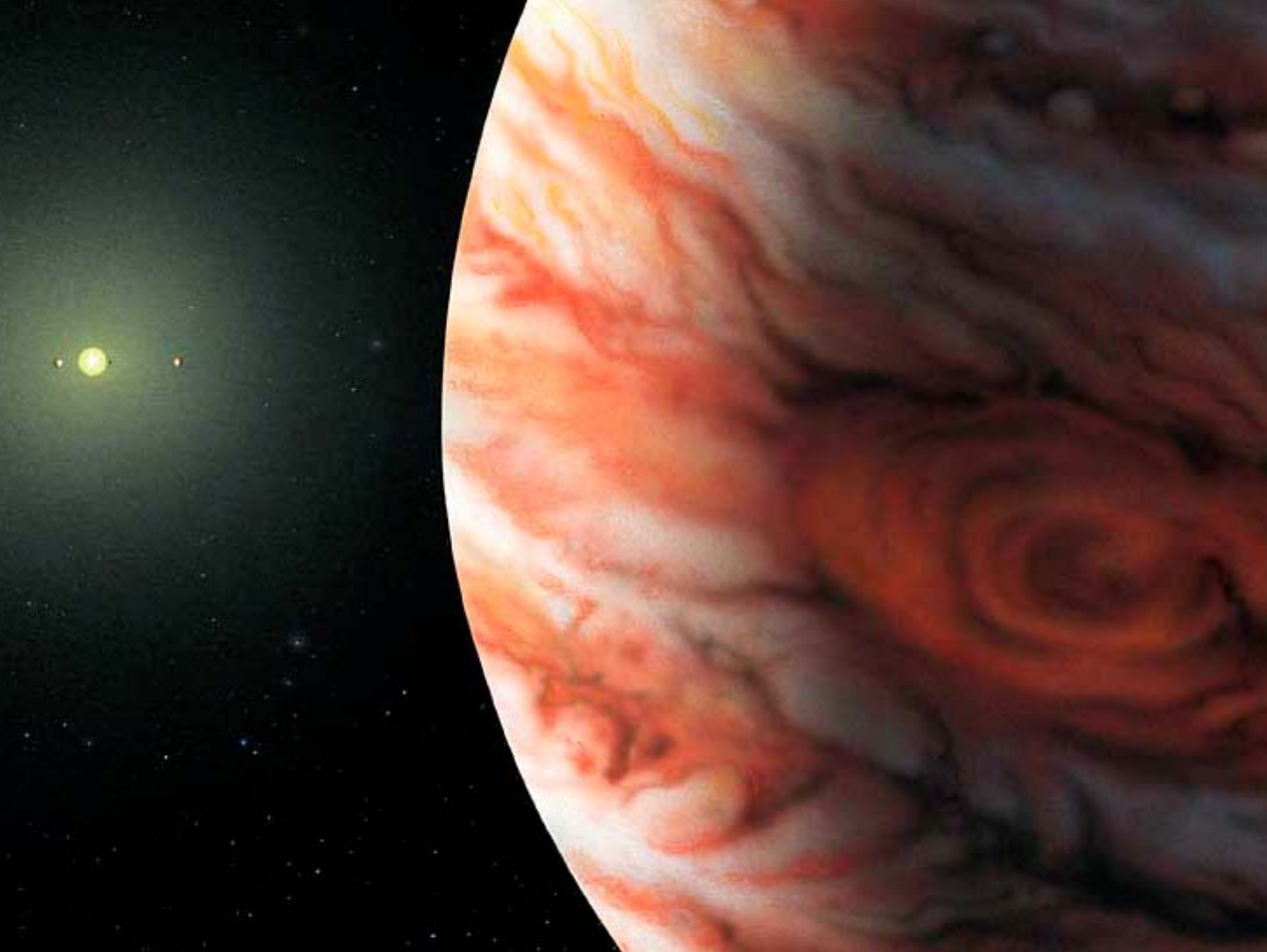

Stellar Irradiation of Close-in Giant Exoplanets

- 51 Pegasus b:

$$4\pi R^2 \sigma T_{\rm eff}^4 = L_{\odot} + L_{\rm int}$$

$$2T_{\odot}^4 = T_{\rm night}^4 + T_{\rm day}^4$$

$$T_{\odot} = 1400\,{\rm K}$$

$$T_{\rm day} = 2^{1/4} T_{\odot}$$

$$T_{\rm day} = 1500\,{\rm K}$$

$$T_{\rm night} = 1272\,{\rm K}$$

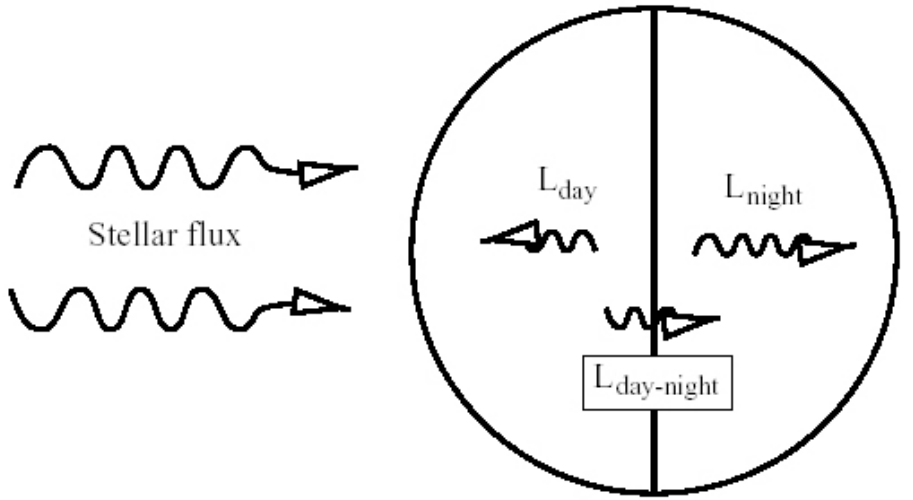

Fig. 5. Schematics of the day-night toy evolution model. The slow mixing of the interior leads to a non-radial heat flux $L_{\rm day-night}$ from the day side to the night side. As a consequence, the intrinsic luminosity on the day side is smaller and that on the night side becomes larger.

Guillot & Showman(2002) A&A, 385, 156.

Atmospheric Dynamic of CGEPs

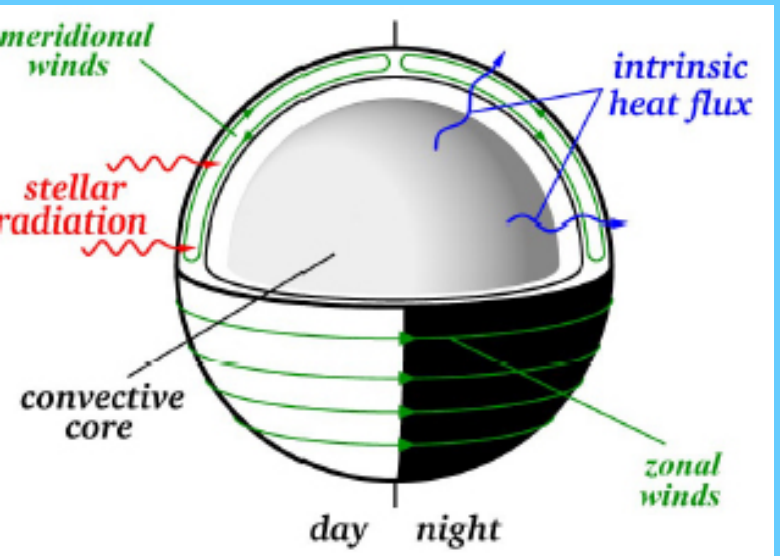

Fig. 2. Conjectured dynamical structure of Pegasi planets: at pressures larger than 100–800 bar, the intrinsic heat flux must be transported by convection. The convective core is at or near synchronous rotation with the star and has small latitudinal and longitudinal temperature variations. At lower pressures a radiative envelope is present. The top part of the atmosphere is penetrated by the stellar light on the day side. The spatial variation in insolation should drive winds that transport heat from the day side to the night side (see text).

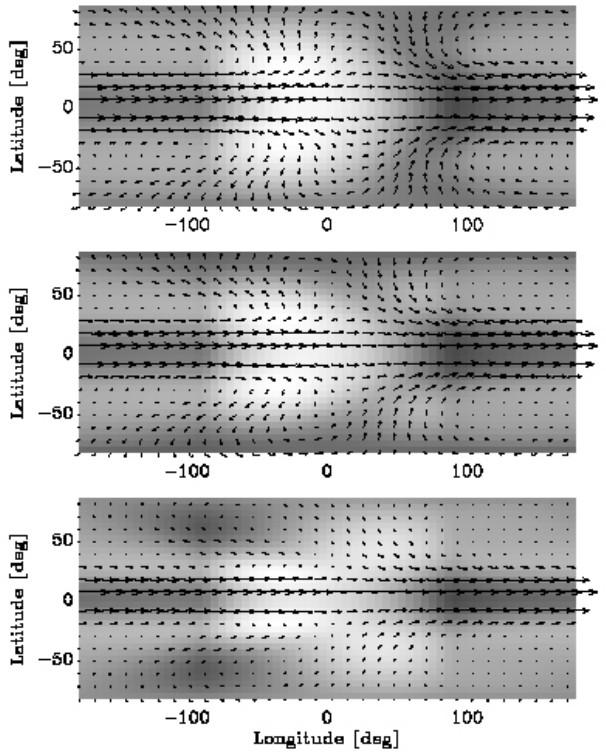

Fig. 7. Additional simulation results at 466 days. Arrows are identical to those in Fig. 6, but here greyscale is vertical velocity $d\theta/dt$, where θ is potential temperature. Light regions are heating (i.e., θ is increasing) and dark regions are cooling (θ is decreasing). From top to bottom, the greyscales span (from dark to white) -0.003 to $0.003\,\mathrm{K\,s^{-1}}$, -0.002 to $0.002\,\mathrm{K\,s^{-1}}$, and -0.001 to $0.001\,\mathrm{K\,s^{-1}}$, respectively. The lowermost panel separates the convective interior from the radiative region, and the implication is that mass exchange can happen across this interface.

Showman & Guillot(2002) A+A, 385, 166.

Spectroscopic Search for Atmospheric Signatures of HD 209458b

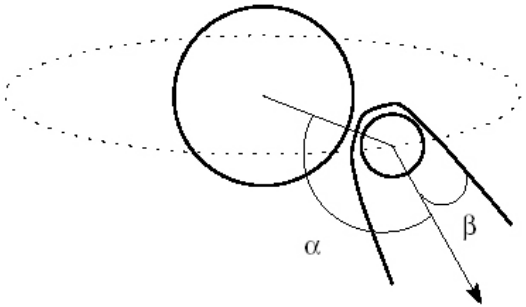

Fig. 1. Illustration of a cometary-tail exosphere around HD 209458b. Stellar wind, escape velocities of the particles and tangential movement of the planet on its orbit define the angles α and β (see Sect. 2)

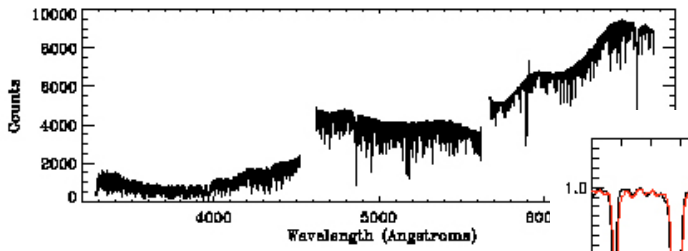

Fig. 2. The total spectrum of the star HD 2094 with UVES, after flatfielding, optimal extraction a rebinning. Some gaps can be seen, which are intr servations in the DIC1 - 390+564 nm setting. T served range is 3280–4562 Å, 4583–5644 Å and 5 Resolving powers of 58 000 in the blue and 71 00 are achieved.

- Moutou et al.(2001): VLT UVES 328-669nm

absorption depth < 1%

- Moutou et al.(2003): VLT ISSAC/ HD209458b/ He λ 1083nm/

absorption depth < 0.5 %

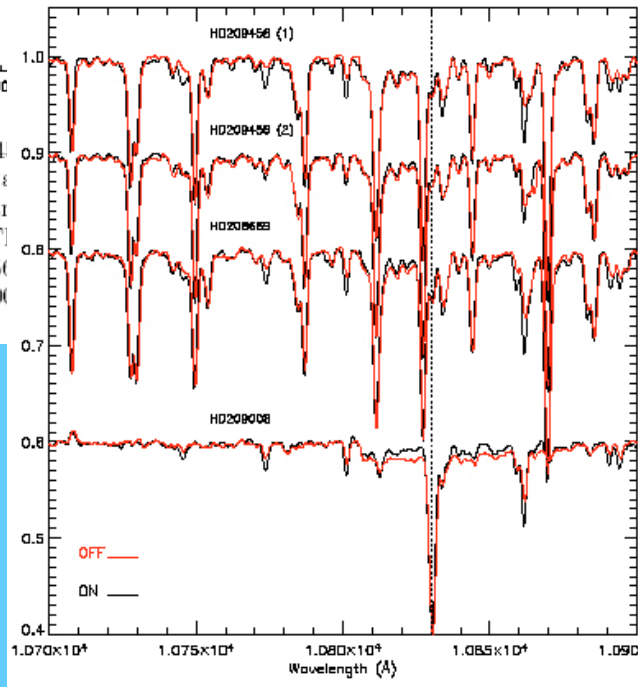

Fig. 4. Reduced and extracted spectra of HD 209458 (divided in into the consecutive period (1) and period (2)), HD 208669 HD 209008, from top to bottom, during both on-transit (thick and off-transit (thin line) nights. The plot shows the domain 10 7 10 900 Å. The spectra, all normalized to unity, are shifted in more visibility. The position of the expected HeI feature is ma with dotted lines.

Moutou et al.(2002) A&A, 371, 260.

Detection of Na λ589.3nm at HD 209458b

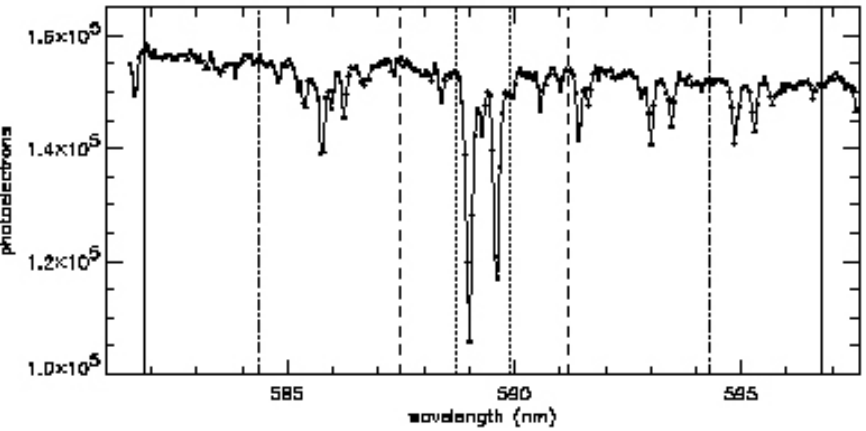

FIG. 1.—Portion of an STIS spectrum of HD 209458, centered on the Na D lines. The vertical axis is the number of detected photoelectrons per wavelength pixel after integrating over 17 pixels in cross-dispersion. The vertical lines indicate the bandpasses over which we integrate the spectrum to produce the photometric time series. The band n_c is the set of pixels between the two dotted lines; m_c is the set between the dashed lines; w_c is the set between the dot-dashed lines. The corresponding blue bands (n_b, m_b, and w_b) are the sets of pixels between the left solid line and the left boundary of the center band. Similarly, the corresponding red bands (n_r, m_r, and w_r) are the sets of pixels between the right edge of the center band and the right solid line.

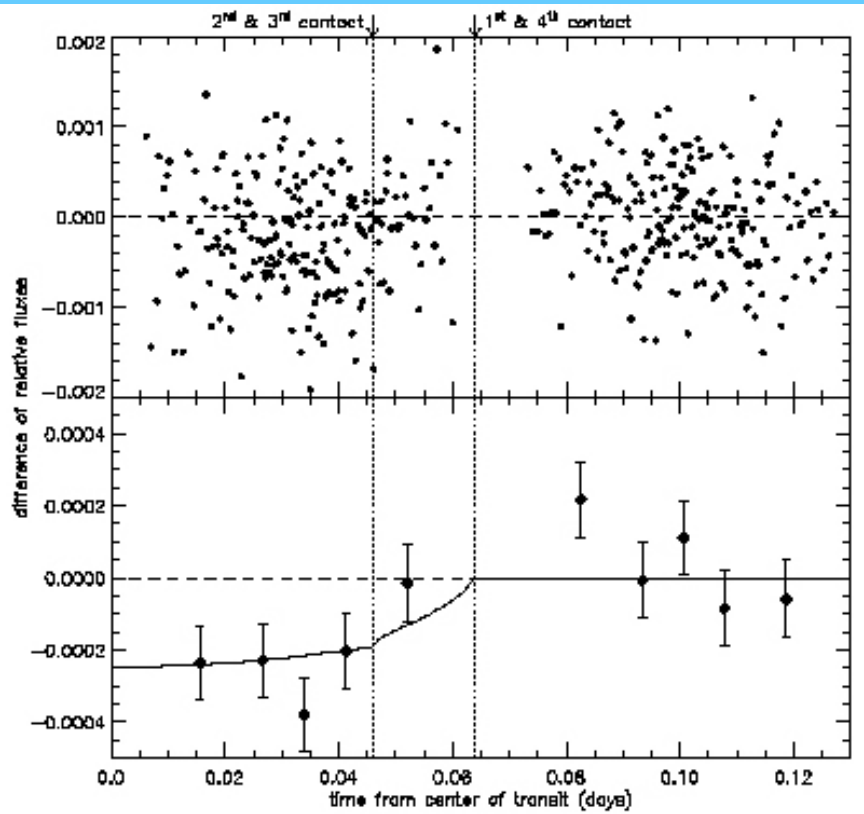

FIG. 4.—*Top*: Unbinned time series n_{Na} (Fig. 2, *top panel*). *Bottom*: These data binned in time (each point is the median value in each bin). There are 10 bins, with roughly equal numbers of observations per bin (42). The error bars indicate the estimated standard deviation of the median. The solid curve is a model for the difference of two transit curves (described in § 3), scaled to the observed offset in the mean during transit, $\Delta n_{Na} = -2.32 \times 10^{-4}$.

Charbonneau et al.(2002) ApJ, 568, 377.

Na absorption depth $= (2.32 \pm 0.57) \times 10^{-4}$

CGEP-Atmospheric Thermal Structure

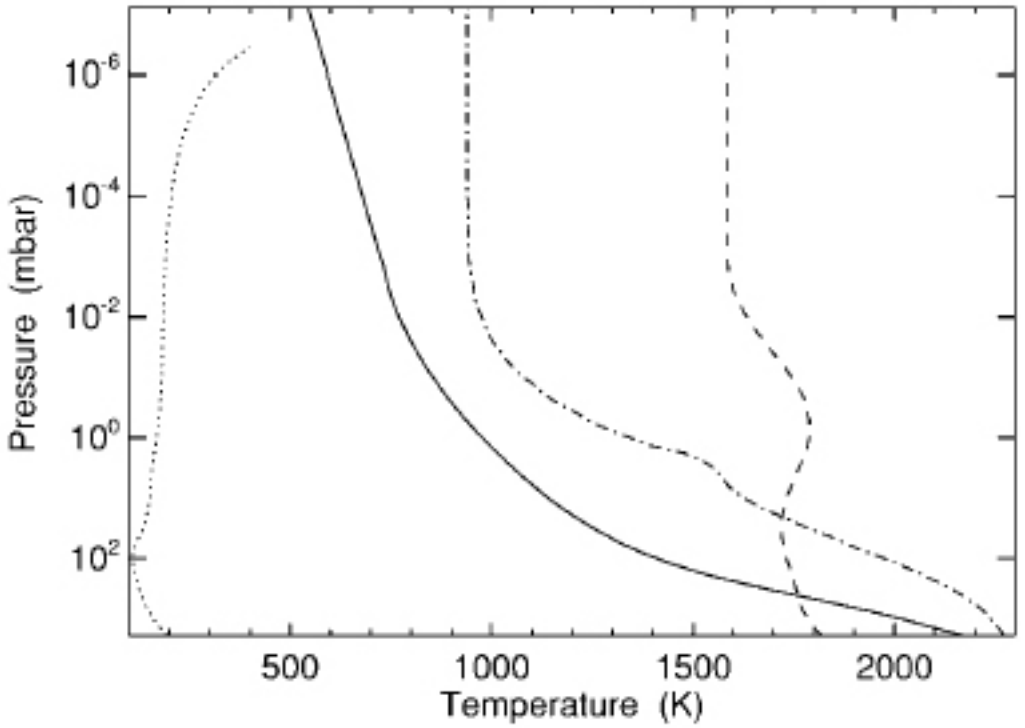

FIG. 1.—Vertical temperature profiles of the reference model (*solid line*), Barman et al. (2002, *dashed line*), Fortney et al. (2003, *dash-dotted line*), and Jupiter (*dotted line*). We assume that the profiles of Barman et al. (2002) and Fortney et al. (2003) are isothermal above their reported pressure levels.

Barman et al. (2002) ApJ, 569, L51.
Fortney et al. (2003) ApJ, 589, 615.
Liang et al. (2004) ApJ, 605, L61.

Extended Hydrogen Atomic Cloud Around HD 209854b

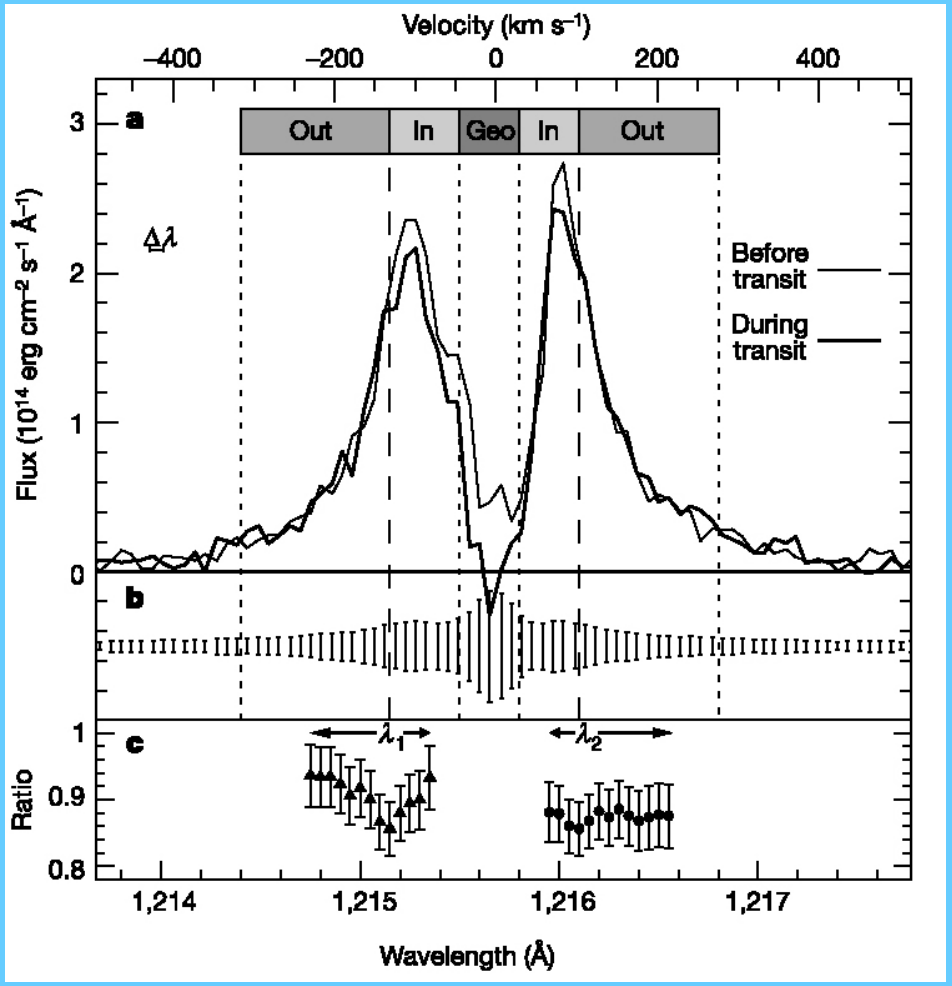

HST Detection of Oxygen and Carbon at HD 209458b

- HST STIS λλ 119 ~ 171 mm
- Detection of OI* and
  - ➡ OII*(collisionallly excited emission)
  - ➡ absorption within a few planetary radii.
- Also CII and CII*.
- Roche lobe
- Hydrodynamic blow off

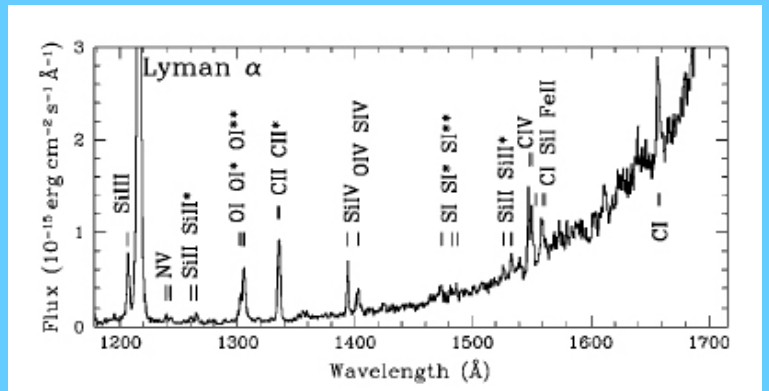

FIG. 1.—Full HD 209458 G140L spectrum. Stellar emission lines are clearly detected together with the stellar continuum, which is increasing toward longer wavelengths.

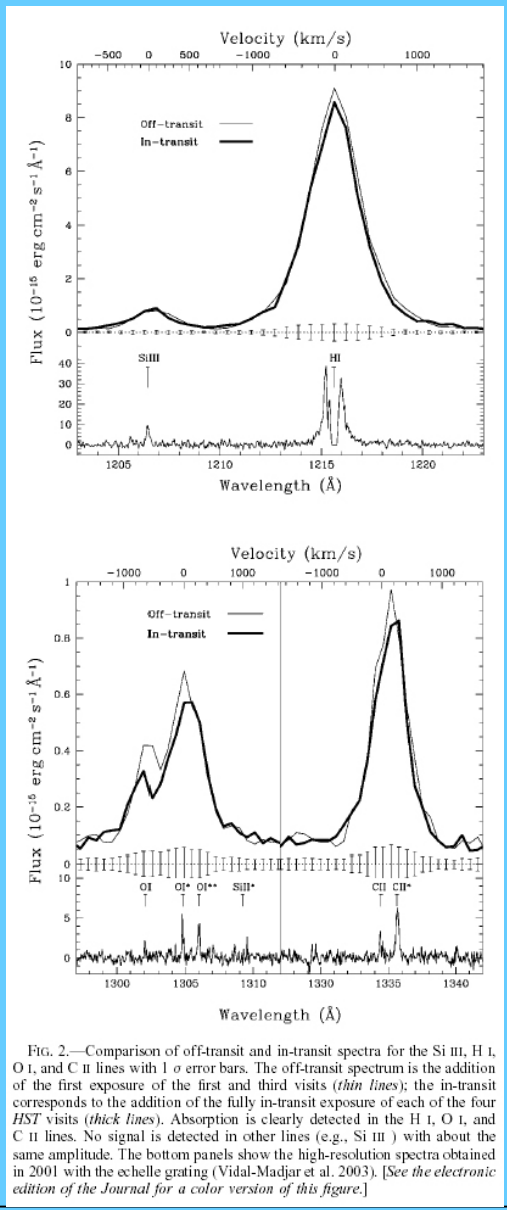

FIG. 2.—Comparison of off-transit and in-transit spectra for the Si III, H I, O I, and C II lines with 1 σ error bars. The off-transit spectrum is the addition of the first exposure of the first and third visits (*thin lines*); the in-transit corresponds to the addition of the fully in-transit exposure of each of the four *HST* visits (*thick lines*). Absorption is clearly detected in the H I, O I, and C II lines. No signal is detected in other lines (e.g., Si III) with about the same amplitude. The bottom panels show the high-resolution spectra obtained in 2001 with the echelle grating (Vidal-Madjar et al. 2003). [*See the electronic edition of the Journal for a color version of this figure.*]

Vidal-Madjar et al.(2004) ApJ, 604, L69.

Oxygen and Carbon in HD 209458b

TABLE 1

ABSORPTION DEPTH OF EMISSION LINES AND CONTINUUM

SPECIES	λ[a] (Å)	ABSORPTION DEPTH[b] 1 σ (%)	2 σ (%)
Continuum	1350–1700	$2.0^{+0.5}_{-0.7}$	...
H I	1212–1220	$5.3^{+1.6}_{-1.9}$	...
O I, O I*, O I**	1300–1310	$12.8^{+4.5}_{-4.5}$	...
C II, C II*	1332–1340	$7.5^{+3.6}_{-3.4}$	...
C I	1557–1565	$0.4^{+21.1}_{-0.4}$	<36.0
C I	1654–1660	$11.3^{+11.9}_{-11.3}$	<33.6
C IV	1545–1554	$0.4^{+9.5}_{-0.4}$	<19.0
N V	1237–1246	$27.3^{+22.7}_{-27.3}$	<50.0
S I, S I*, S I**	1471–1489	$32.2^{+13.0}_{-32.2}$	<58.2
Si II, Si II*	1525–1536	$18.4^{+15.4}_{-18.4}$	<47.4
Si III	1204–1210	$0.0^{+2.2}_{-0.0}$	<5.9
Si IV	1391–1397	$0.0^{+6.5}_{-0.0}$	<14.0

NOTE.—1 σ error bars and 2 σ upper limits for non-detections.

[a] Wavelength range for the line's intensity evaluation.

[b] Absorption depth given by the $(R_{abs}/R_*)^2$ parameter of the fit (see text).

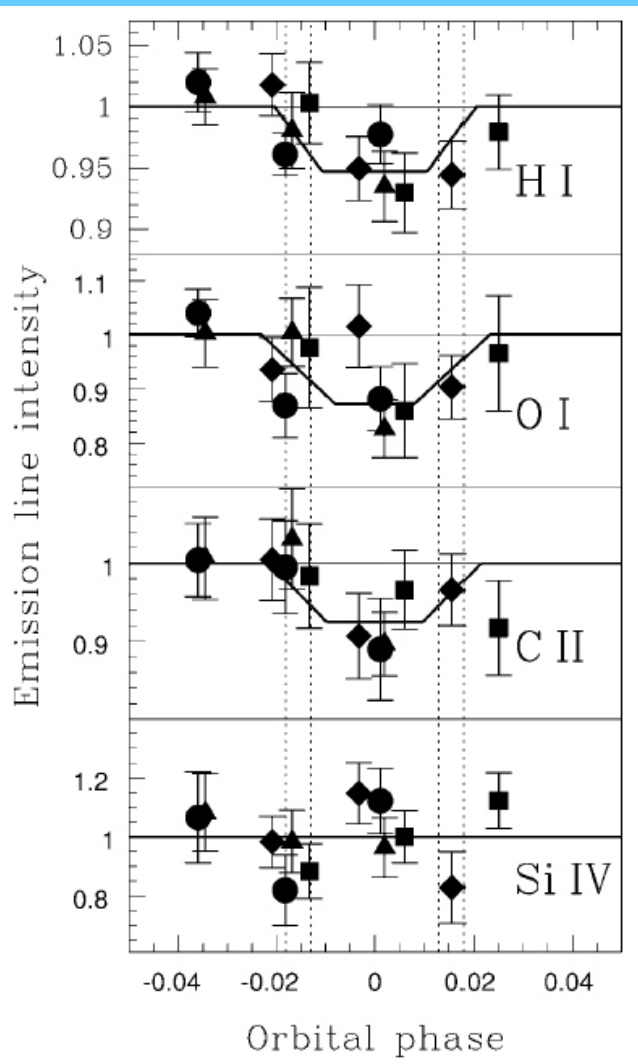

FIG. 3.—Plot of the lines' total intensity as a function of the orbital phase. Circles, squares, triangles, and diamonds are for first to fourth transits, respectively. The vertical dotted lines correspond to the position of the first to fourth contacts of the planetary disk transit. The thick line represents the best fit to the data (see § 3). Absorptions are detected in H I, O I, and C II during the transits; no significant absorptions are detected in the other lines (i.e., Si IV). [*See the electronic edition of the Journal for a color version of this*

- $(R_{abs}/R_*)^2 \sim 1.5\%$
- Absorption depth: 10% ➠

Roche Lobe Overflow

- HST STIS Measurements
- Lyα absorption depth ~ 15%
- Filling beyond the Roche lobe with radius $\simeq 2.7 R_p\,(3.6)\,R_J$
- Large-scale atmospheric excape with $\dot{M} > 10^{10} g/s$

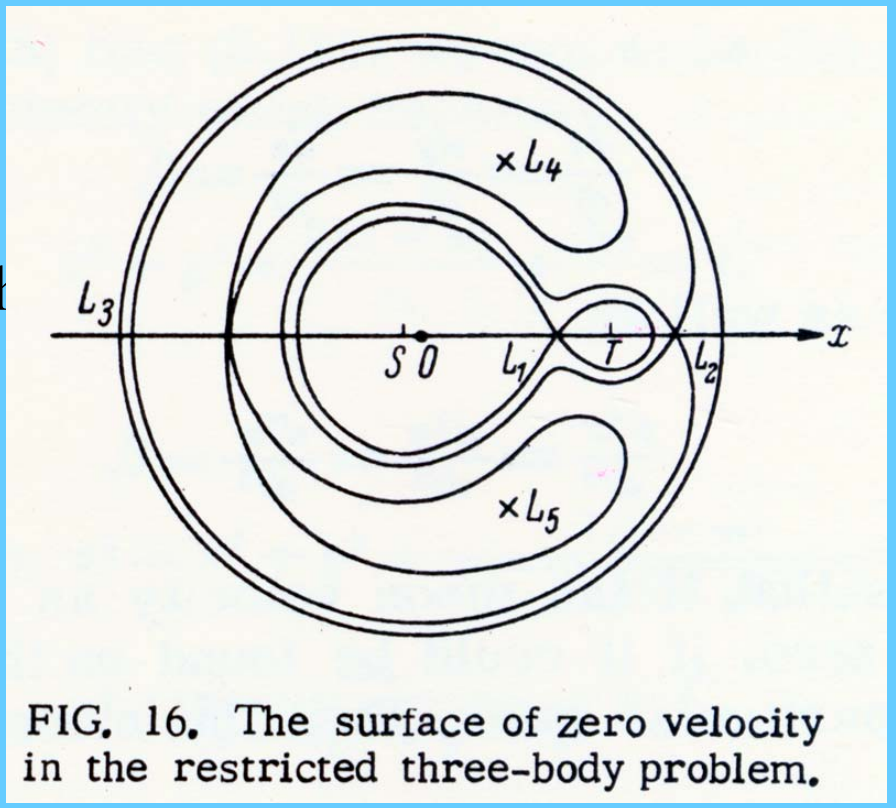

FIG. 16. The surface of zero velocity in the restricted three-body problem.

Vidal-Madjar et al. (2003) Nature, 422, 143.

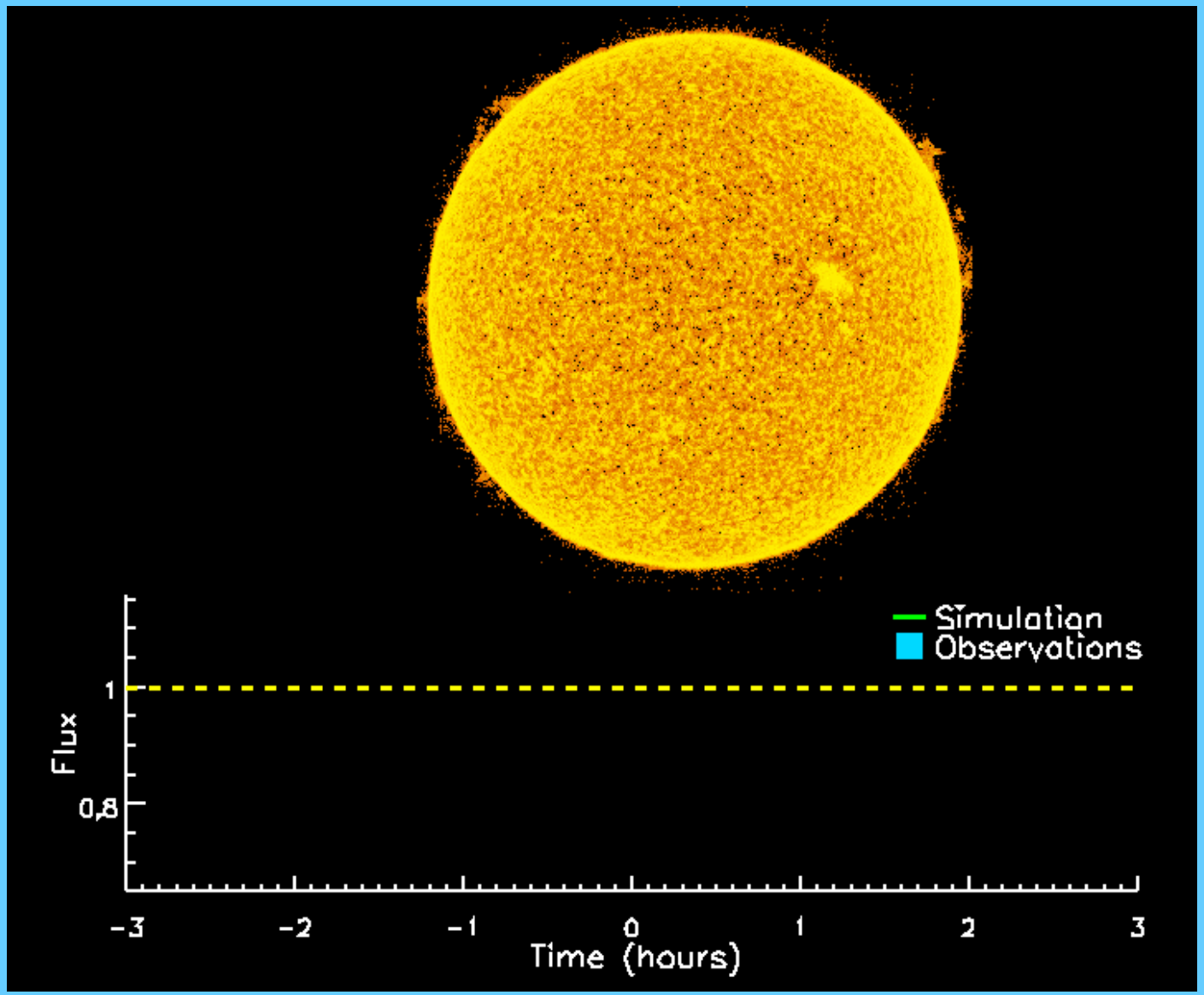
Simulation
Observations
Flux
1
0,8
-3
-2
-1
0
1
2
3
Time (hours)

Osiris

The Egyptian god of the underworld and of vegetation.

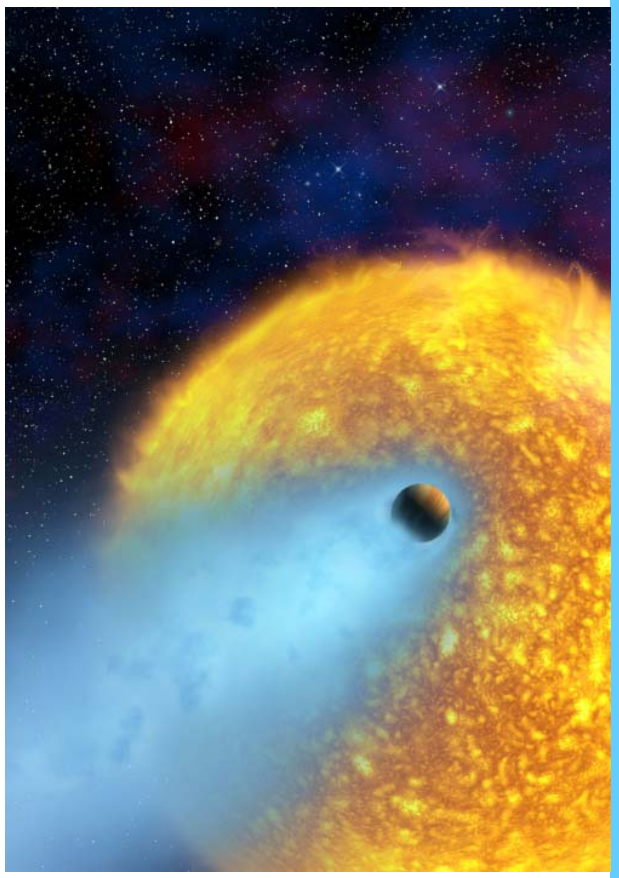

Open Questions

- **Thermal structure of the atmosphere**
- **Sources of the atomic hydrogen, carbon and oxygen**
- **Heating mechanisms of the upper atmosphere**
- **Atmospheric loss rate**
- **Evolutionary effect**

CEGP-Atmospheric Thermal Profile

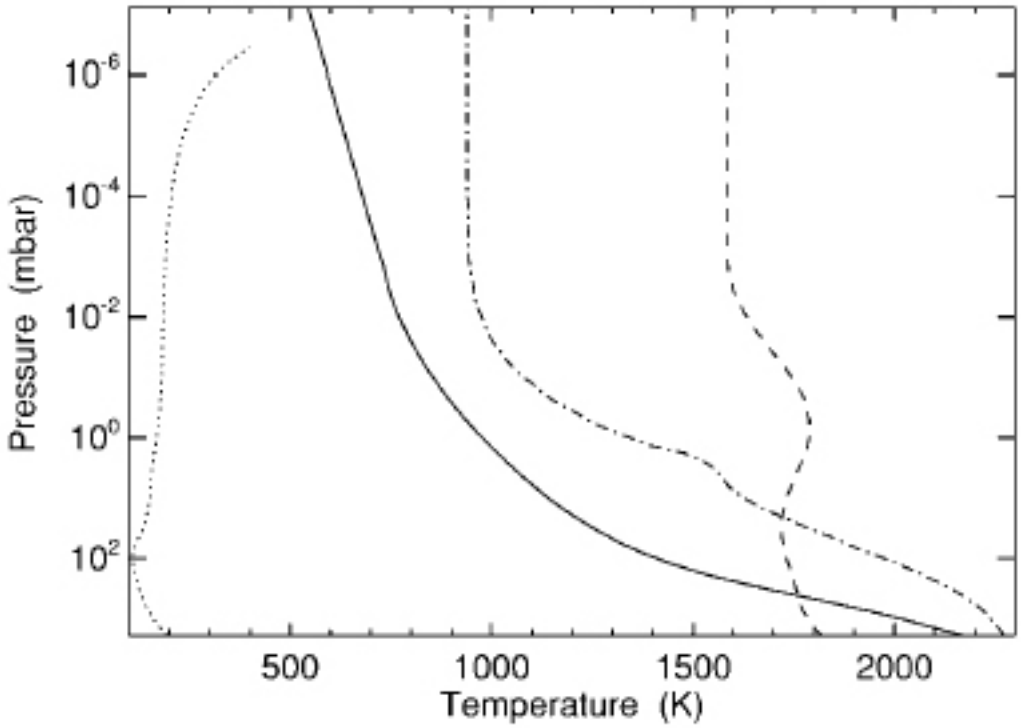

FIG. 1.—Vertical temperature profiles of the reference model (*solid line*), Barman et al. (2002, *dashed line*), Fortney et al. (2003, *dash-dotted line*), and Jupiter (*dotted line*). We assume that the profiles of Barman et al. (2002) and Fortney et al. (2003) are isothermal above their reported pressure levels.

Liang et al. (2004) ApJ, 605, L61.
Barman et al. (2002) ApJ, 569, L51.
Fortney et al. (2003) ApJ, 589, 615.

Photochemistry in the Atmospheres of CEGPs

- Chemical equilibrium of H_2, CO, H_2O and CH_4 in high temperature (>~ 1000K)
  - $CO:H_2O:CH_4$ = $3.6\times10^{-4}:4.5\times10^{-4}:3.9\times10^{-8}$
- Major H source from:
  - $H_2O + h\nu \Rightarrow H + OH$
- Major Oxygen source from:
  - $CO + h\nu \Rightarrow C + O$
- Very small amount of C_2H_2(unlike in the cold Jovian atmosphere) and little photochemical hydrocarbon aerosols.

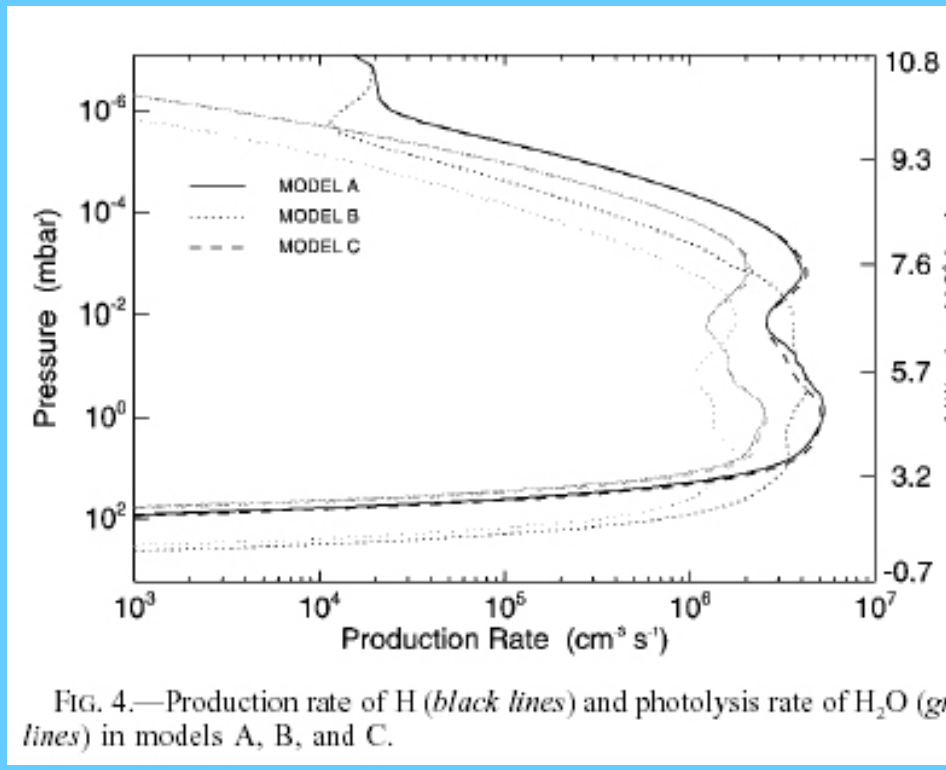

FIG. 4.—Production rate of H (*black lines*) and photolysis rate of H_2O (*gr lines*) in models A, B, and C.

Seager & Sasselov (2002) ApJ, 537, 916.
Liang et al. (2003) Apj, 596, L247.

Photochemistry of Hydrocarbon Aerosols

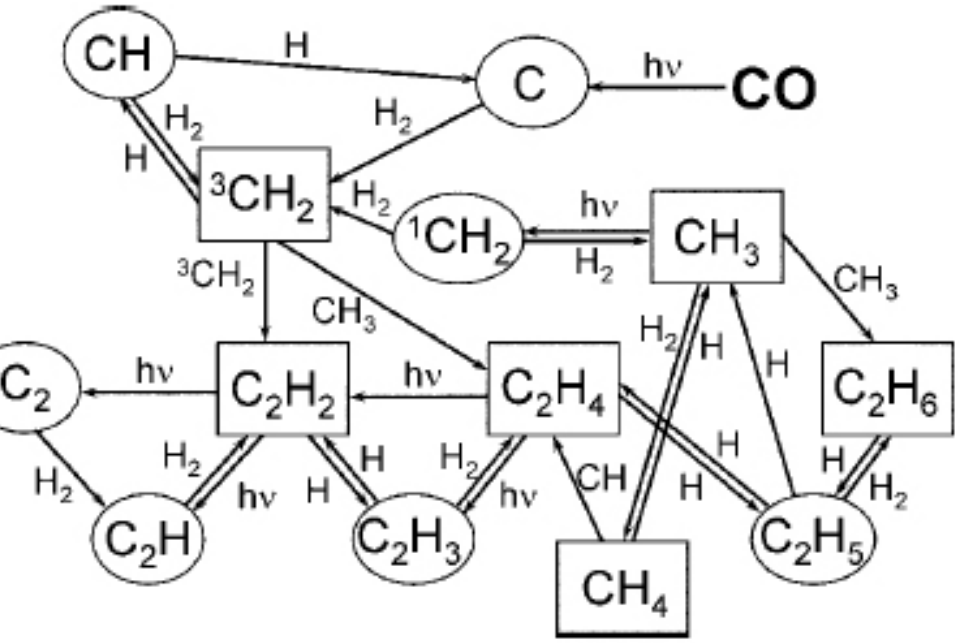

FIG. 2.—Major photochemical pathways for forming C and C_2 species

FIG. 3.—Comparison of volume mixing ratios of C_2H_2 (*top panel*), C_2H_4 (*middle panel*), and C_2H_6 (*bottom panel*) for models A, D, E, and Jupiter (*solid, dashed, dash-dotted, and dotted lines*, respectively). The high C_2H_2 mixing ratio at the top of the atmosphere is due to the high photolysis rate of CO.

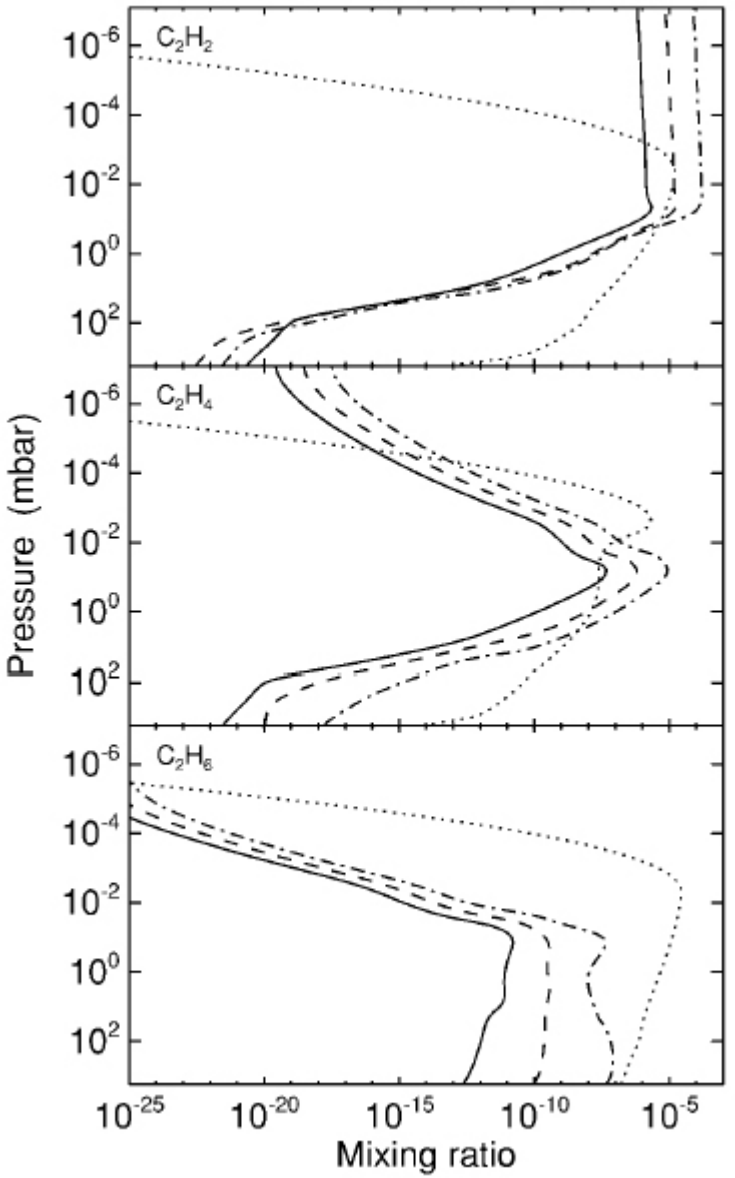

C_nH_m HD 209458b/Jupiter mixing ratio ~ 10^{-4}

Liang et al. (2004) ApJ, 605, L61.

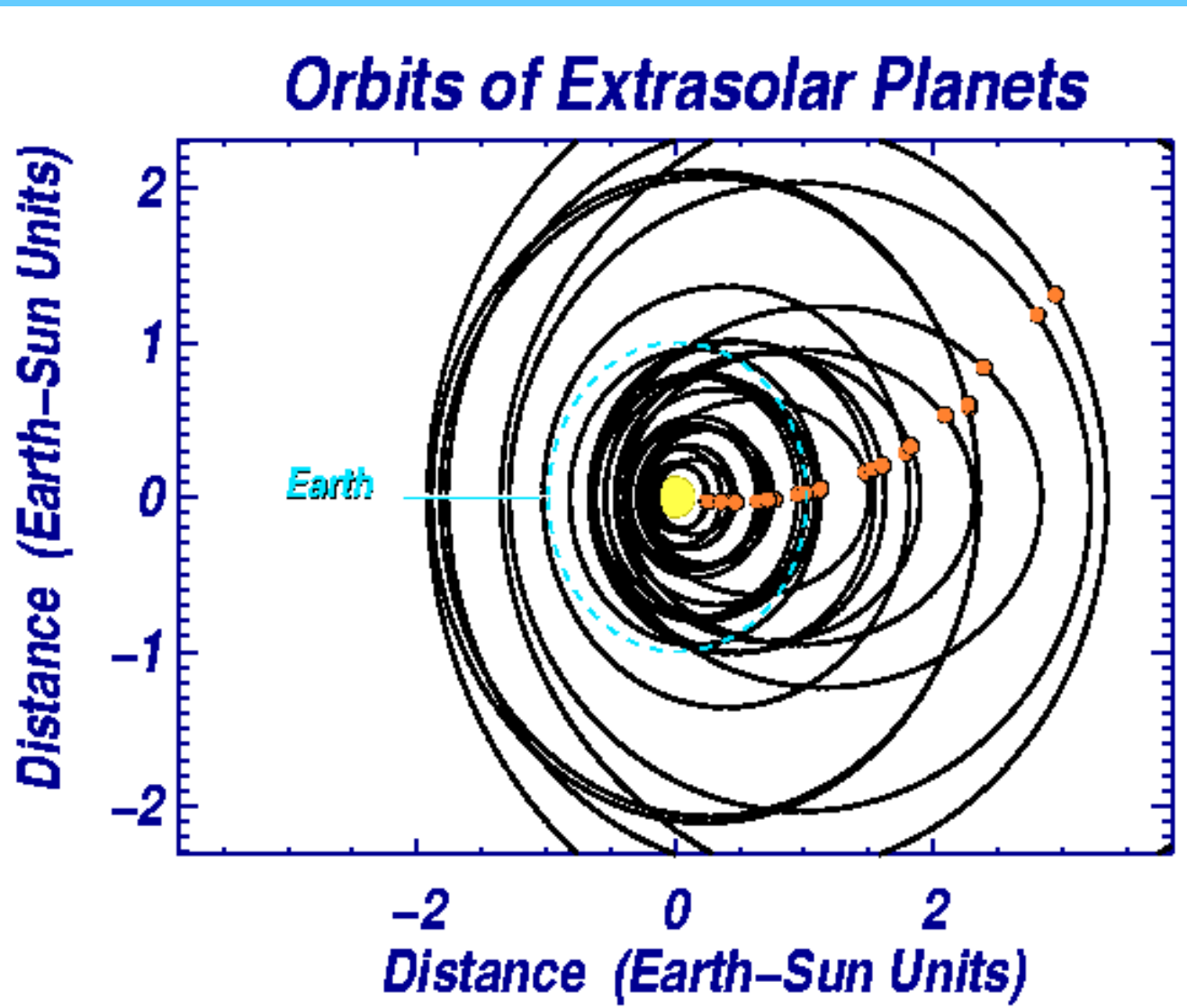
Orbits of Extrasolar Planets
Distance (Earth–Sun Units)
2
1
0
–1
–2
Earth
–2
0
2
Distance (Earth–Sun Units)

Jovian Thermospheric Temperature

Surface equilibrium temperature at

- Jupiter:

$$T_{eq} = \frac{300K}{\sqrt{a}} = 131K$$

Jovian thermospheric temp ~ 850 K

Soft photoelectrons as heat source ?

Same effect at other outer planets.

Solar EUV and X-ray flux as

- ionization and photodissociation

gents.

Barthelemy et al. (2004) A&A, 423, 391.
Hunten & Dessler (1977) Planet. Space Scil, 25, 817.

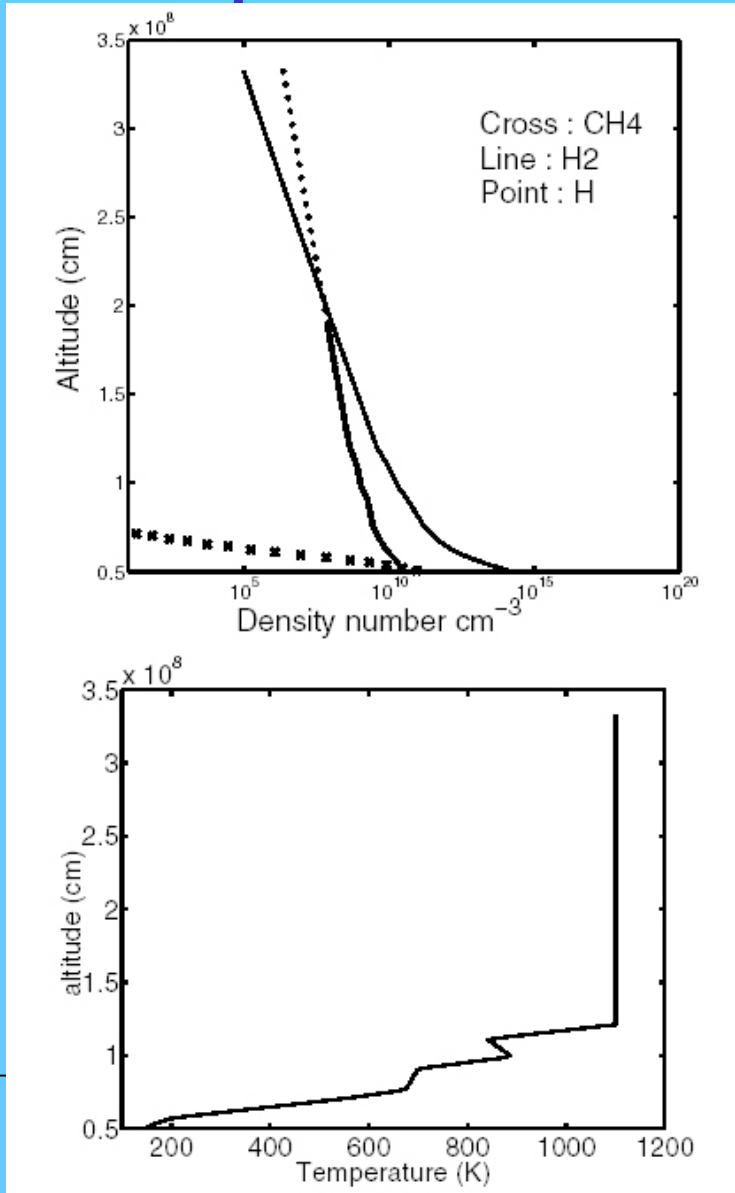

Fig. 1. Jovian neutral atmosphere, *top panel*: composition, *bottom panel*: temperature (non-bulge region).

Heating by the Stellar XUV Flux

Bauer(1971, 1973; Bauer and Hantsch, 1989):

$$T_{xuv}^{s} \simeq \frac{\varepsilon \alpha I_{xuv} \kappa \sigma_c}{K_0 m_i g \sigma_a} + T_0^s$$

Where I_{xuv} is the XUV intensity at the planet's orbital distance, ε is the heating efficiency, κ the Boltzmann constant, m_i is the mass of the atmospheric molecule(H_2), $K(T) = K_0 T^2$ is the thermal conductivity , g is the gravitational acceleration, T_0 is the thermospheric temperature at the base, σ_c and σ_a are the collision and absorption cross sections, respectively.

$$\frac{\left(T_{xuv}^{s} - T_0^s\right)_1}{\left(T_{xuv}^{s} - T_0^s\right)_2} \approx \frac{I_{xuv_1} g_2}{I_{xuv_2} g_1}$$

Bauer (1971) Nature, 232, 101.
Bauer (1973) Physics of Planetary Ionspheres(Heidelberg: Springer)
Bauer & Hantsch (1989) Geophys. Rev. Letter, 16, 373.

Evolution of the Stellar XUV Flux

"Sun in time" program (Guinan & Ribas 2002): XUV flux of solar-type stars (~130 Myr - 8 Gyr) in 0.1 – 100nm interval

- $\frac{I_0(t)}{I_0} = 6.16\,[t\,(Gyr)]^{-1.19}$

Obs. of HI Lyα fluxes from HST

- $\frac{I_{L\alpha}(t)}{I_{L\alpha}} = 3.17\,[t\,(Gyr)]^{-0.75}$

$$
\begin{aligned}
I_{xuv}(t) &= I_0(t) + I_{L\alpha}(t) \\
&= 6I_0 + 3I_{L\alpha} \qquad at\ t = 1.0\ Gyr \\
I_{xuv} &= 100I_0 + 20I_{L\alpha} \qquad at\ t = 100\ Gyr
\end{aligned}
$$

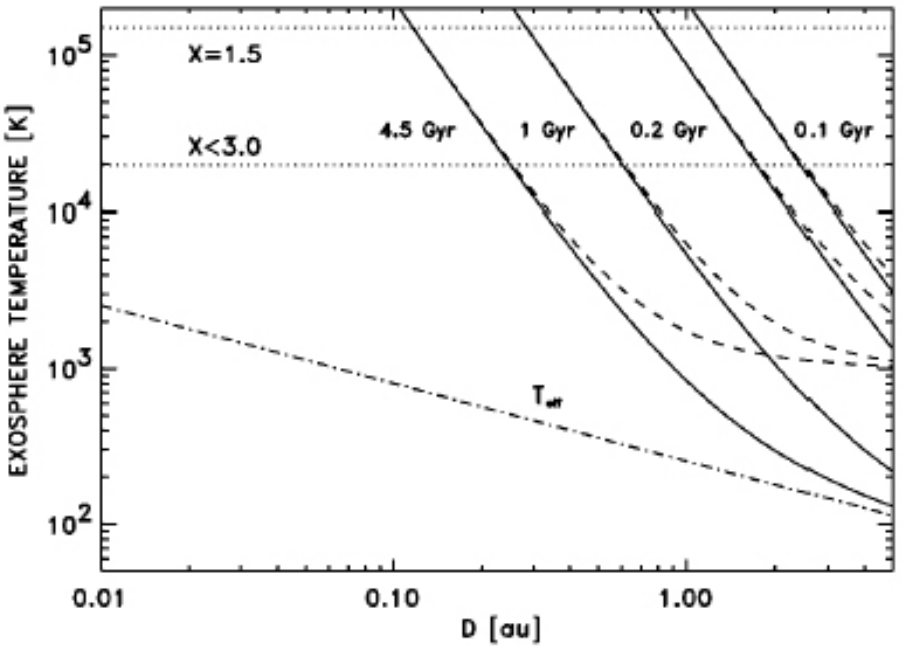

FIG. 1.—Scaled T_{XUV_∞} and T_∞ for Jupiter-class exoplanets are shown as a function of orbital distance for Sunlike stars with ages of 4.5, 1, 0.2, and 0.1 Gyr. The corresponding XUV fluxes are 1, 6, 50, and 100 times the present value. *Dashed lines*: T_∞ calculated by scaling solely the XUV contribution and assuming the additional heating sources to be a constant term. *Sold lines*: Only the scaled T_{XUV_∞}. As can be seen, regardless of the case considered, the exosphere temperature reaches blow-off conditions (*dotted lines*). *Dashed-dotted line*: T_{eff}, which is much smaller than T_∞ at close orbital distances.

Lammer et al. (2003) ApJ, 598, L121.

Extended Hydrogen Atmosphere Around HD 209458b

- HST STIS Measurements
- Lyα absorption depth ~ 15%
- Filling beyond the Roche lobe with radius $\simeq 2.7 R_p\,(3.6)\,R_J$
- Large-scale atmospheric excape with $\dot{M} > 10^{10} g/s$

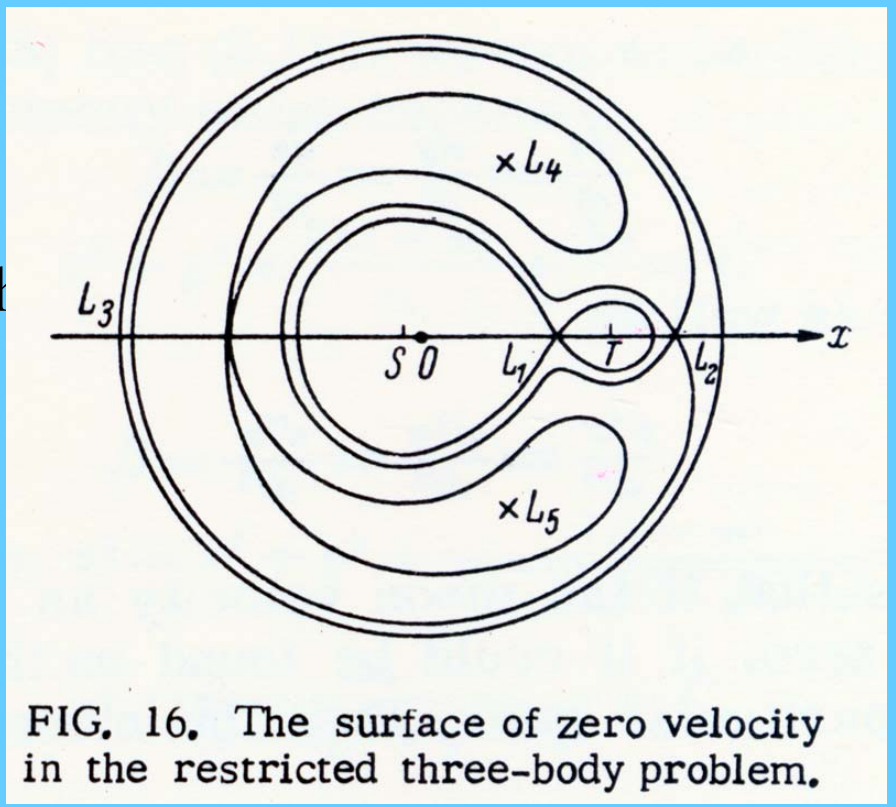

FIG. 16. The surface of zero velocity in the restricted three-body problem.

Vidal-Madjar et al. (2003) Nature, 422, 143.

Tidal Effect on Atmospheric Escape from CEGPs

- HST detection of HI, OI, CI and CII in the atmosphere of HD 209458b

➠ Roche lobe filling, with a thermospheric temperature of 5000 ~ 20,000 K.

- Tidal force ➠ $\dot{M}(\theta, \phi)$

- Lyα radiation pressure force to be considered in future.

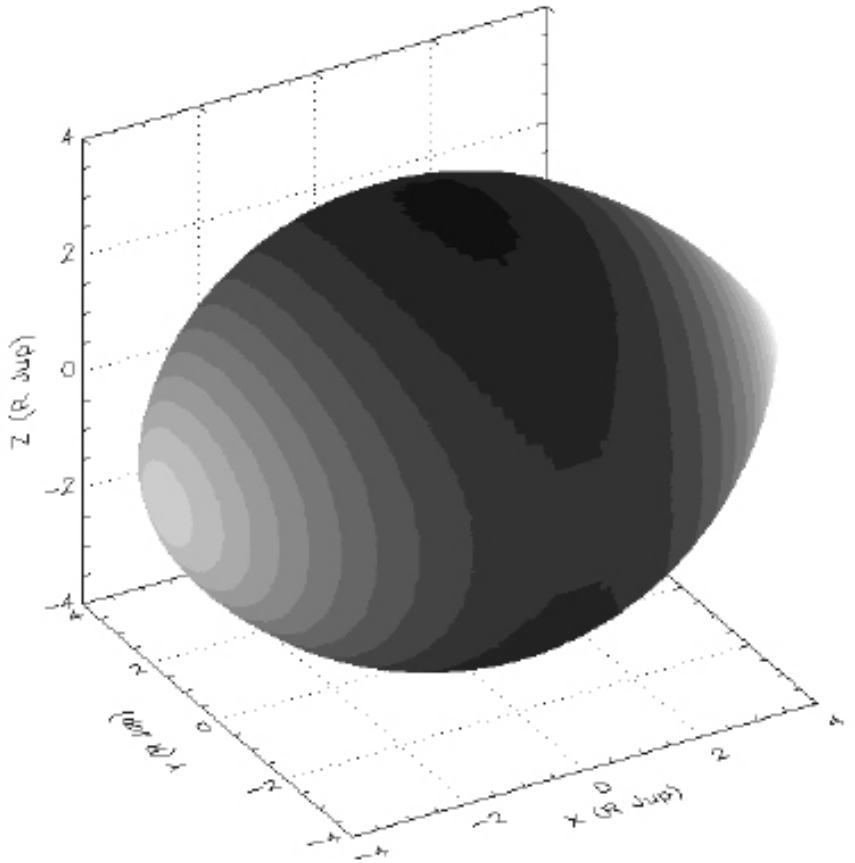

Fig. 2. Shape of the exobase and the corresponding escape rate (Model A, T_{up} = 11 100 K). Light grey is for the large escape rates (10^{10} g s^{-1} str^{-1}) and black is for the small escape rates ($<5 \times 10^{9}$ g s^{-1} str^{-1}). The star is on the X-axis toward positive coordinates. The escape rate is the largest toward the star and in the opposite direction.

Lecavelier et al. (2004) A&A, 418, L1.

XUV-driven Atmospheric Loss

Theory of energy-limited
ydrodynamical outflow in
ydrogen-dominated
tmosphere(Watson et al. 1981)

$$\dot{N} = \frac{4\pi r_0 r_1^2 I_{xuv}}{GMm} \ (s^{-1})$$

UV Absorption
ayer

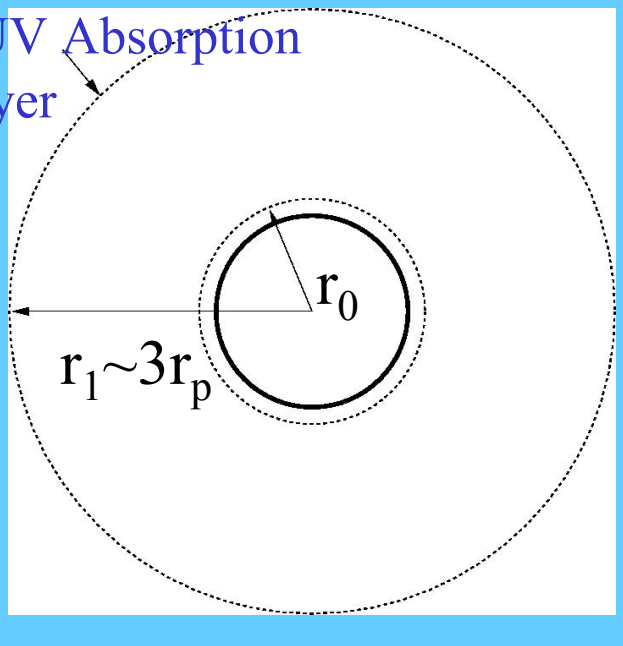

$$\dot{M} \approx 10^{12} g/s$$

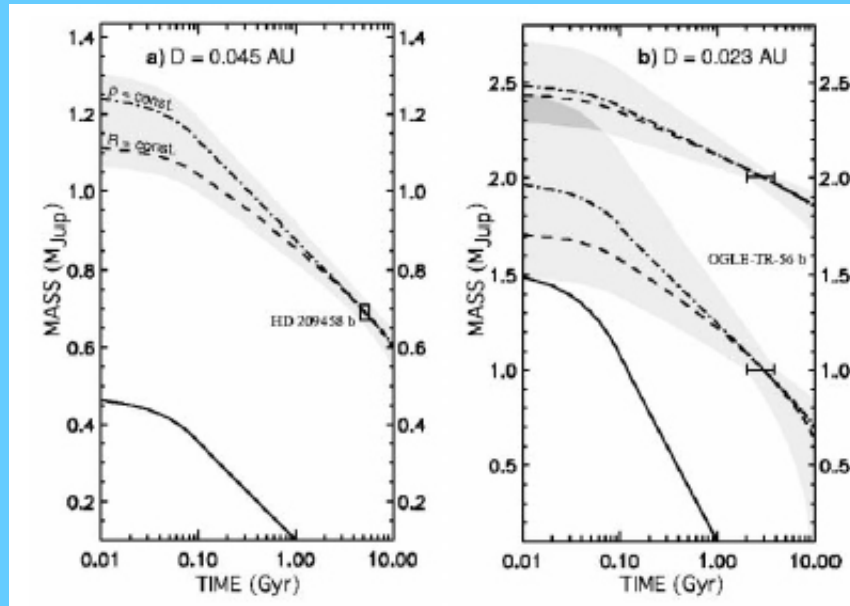

FIG. 3.—Long-term evolution of the mass of hot Jupiters from XUV-drive
thermal escape. For a given set of parameters characterizing an exoplanet
a given age τ (r_{pl}: radius, M: mass, D: orbital distance), one can calculate th
mass evolution by assuming (1) that the only loss process is energy-limite
escape, (2) a mass-radius relation, (3) a constant orbital distance, and (4)
hydrogen-rich atmosphere. The observed parameters for HD 209458b (*a*) a
$r_{pl} = 1.43 \pm 0.04 R_{Jup}$, $M = 0.69 \pm 0.02 M_{Jup}$, and $\tau = 5.2$ Gyr (Cody & Sa
selov 2002). For OGLE-TR-56b (*b*), we adopted $r_{pl} = 1.3 \pm 0.15 R_{Jup}$, $M =$
$0.9 \pm 0.3 M_{Jup}$, and $\tau = 3 \pm 1$ Gyr (Konacki et al. 2003; Sasselov 2003). Th
dashed and dash-dotted lines show the evolution obtained with the mean ob
served parameters, considering, respectively, a constant radius or densit
Shaded area: Envelope of all possible evolution scenarios within the unce
tainties of the planetary parameters. *Solid curve*: Evolution of a gaseous plan
at the same orbital distance with a constant density of 0.3 g cm^{-3}, which ful
evaporates after 1 Gyr. In the case of OGLE-TR-56b, whose nature is still
debate, our calculations yield an initial mass of $2.5 \pm 0.2 M_{Jup}$ if its curre
mass turned out to be twice the value determined by Konacki et al. (2003)

M-R Relation

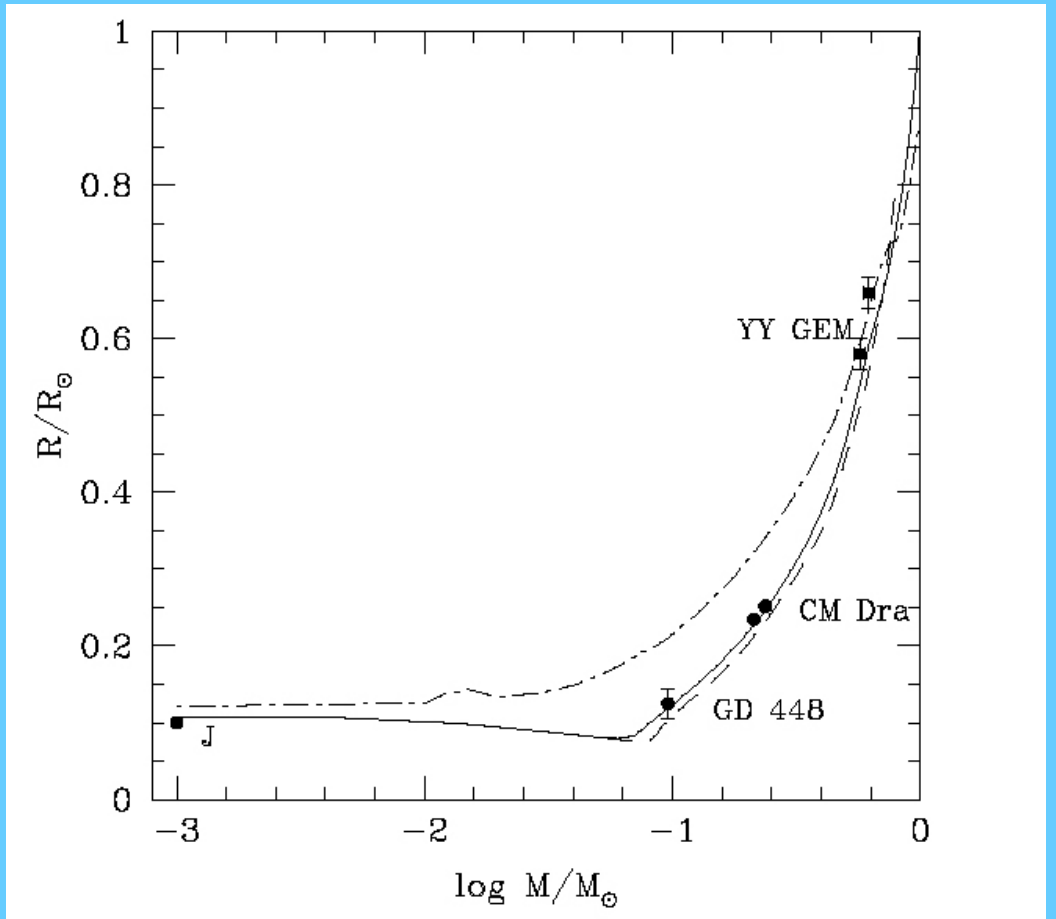

Figure 3 Mass-radius relationship for LMS and SSOs for two ages, $t = 6 \times 10^7$ yr (*dot-dash line*), 5×10^9 yr (*solid line*) for $Z = Z_\odot$, and $t = 5 \times 10^9$ yr for $Z = 10^{-2} \times Z_\odot$ (*dashed line*). The HBMM is 0.075 $M_\odot$ for $Z = Z_\odot$ and 0.083 $M_\odot$ for $Z = 10^{-2} \times Z_\odot$. Also indicated are the observationally-determined radii of various objects (see text) and the position of Jupiter radius (J). The bump on the 6×10^7 yr isochrone illustrates the initial D-burning phase.

Thermal Evaporation of CGEPs

- Evaporation affects significantly the inner structure and the m-R relationship.
- No irradiation ➠ gradual contraction
- With irradiation ➠ contraction countered by envelope expansion
- Existence of critical mass (m_{crit}) by which run away evaporation takes place for $m < m_{crit}$.
- An extra energy source might be required to explain the present radius of HD 209458b.

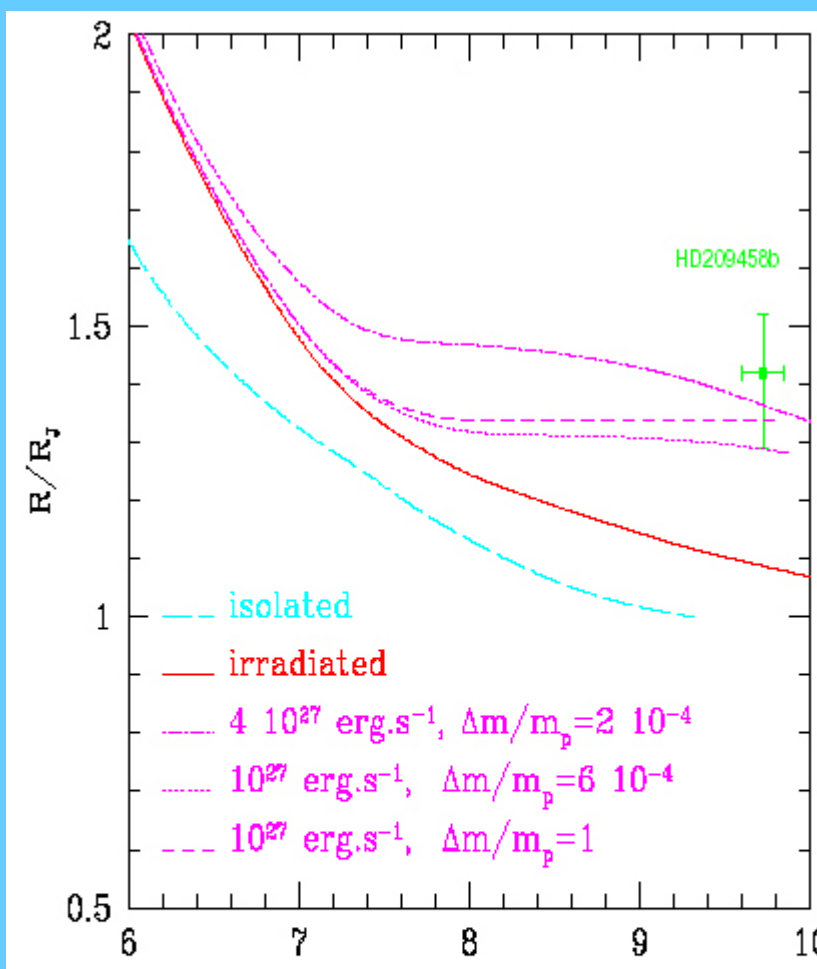

Fig. 8. Effect of extra source of energy dissipation on the evolution of planet with mass $m_p = 0.69\ M_J$. The solid and long-dashed lines correspond to the irradiated and non-irradiated sequences respectively, wit no extra source of energy dissipation. The other curves correspond t irradiated sequences with a total amount of additional energy L_{ext} (in erg s^{-1}) deposited in layers between the surface and the mass shel $m_r = \Delta m$, as indicated in figure (see text)

Baraffe et al. (2003) A&A, 402, 701.
Baraffe et al. (2004) A&A, 419, L13.

Exoplanets III

Hot Jupiters

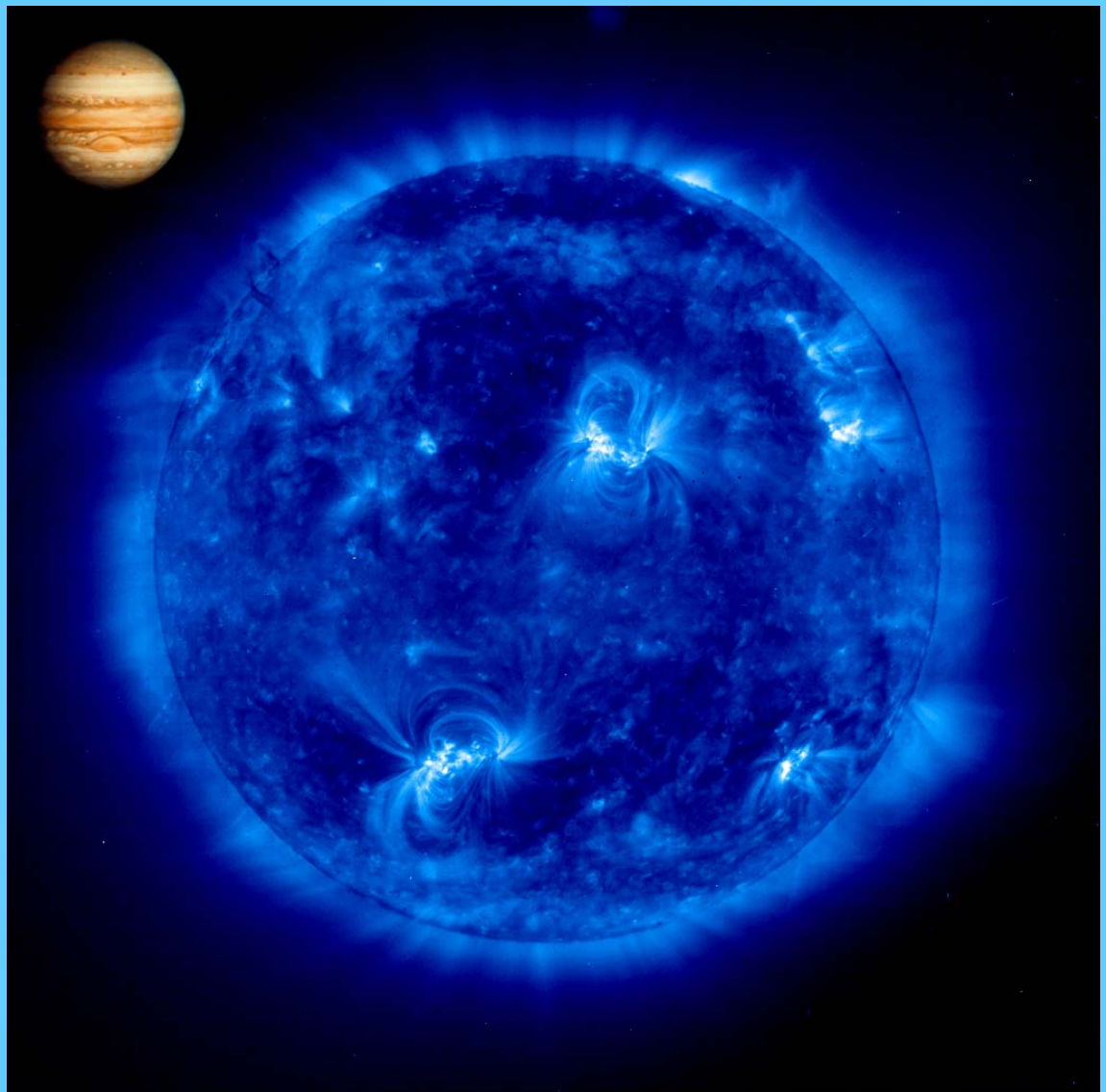

Stellar Interaction with CEGPs

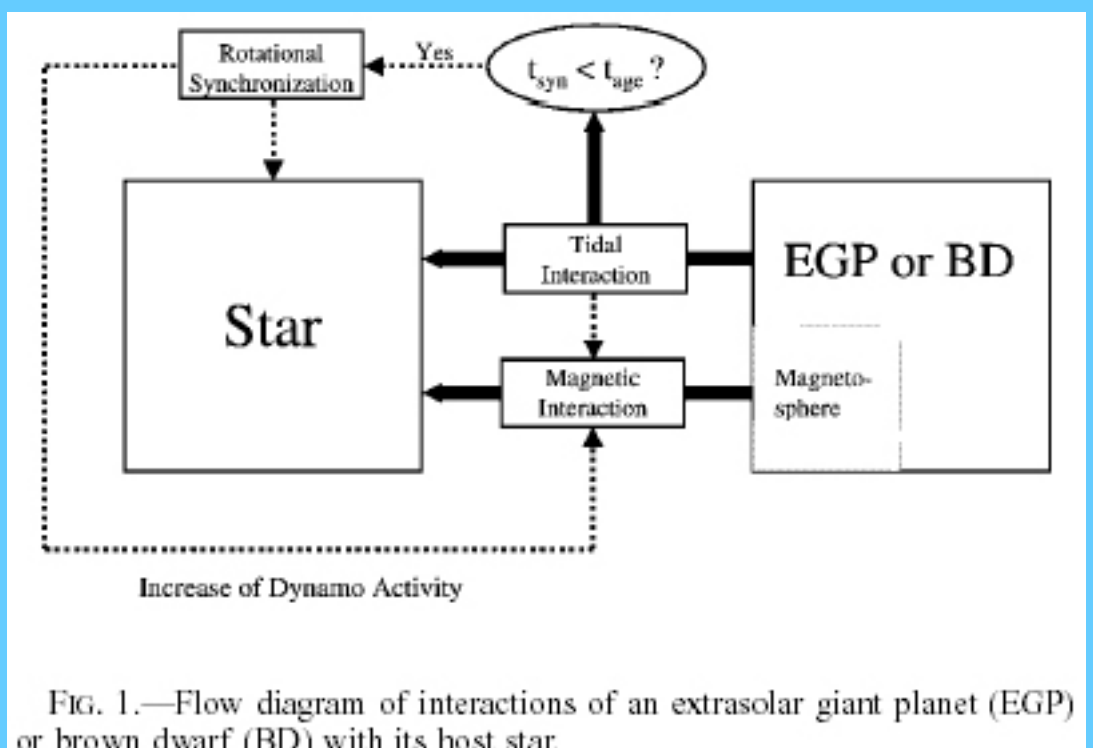

FIG. 1.—Flow diagram of interactions of an extrasolar giant planet (EGP) or brown dwarf (BD) with its host star.

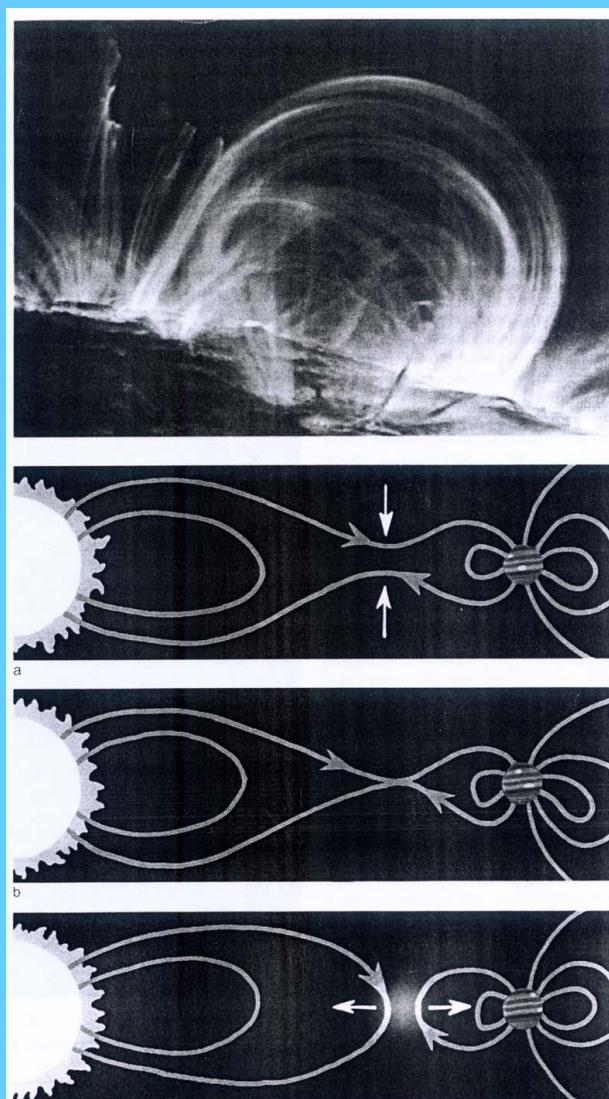

Figure 7. Filaments of hot coronal gas reveal looping solar magnetic-field lines in an image obtained from the Transition Region and Coronal Explorer (TRACE) spacecraft (*top*). The magnetic fields around stars with giant planets in close orbit are likely to be even more complicated, with some lines connecting the two bodies (*a*). At times motion of the planet or of the ionized gases in space (*white arrows*) can force two fields lines together, allowing them to break from one configuration and reconnect in another (*b*). This process injects energy into the surrounding plasma, accelerating charged particles and giving off a burst of high-fre

Cuntz et al. (2000) ApJ, 533, L151.
Rubenstein (2001) Arner. Scientist, 89, 38.

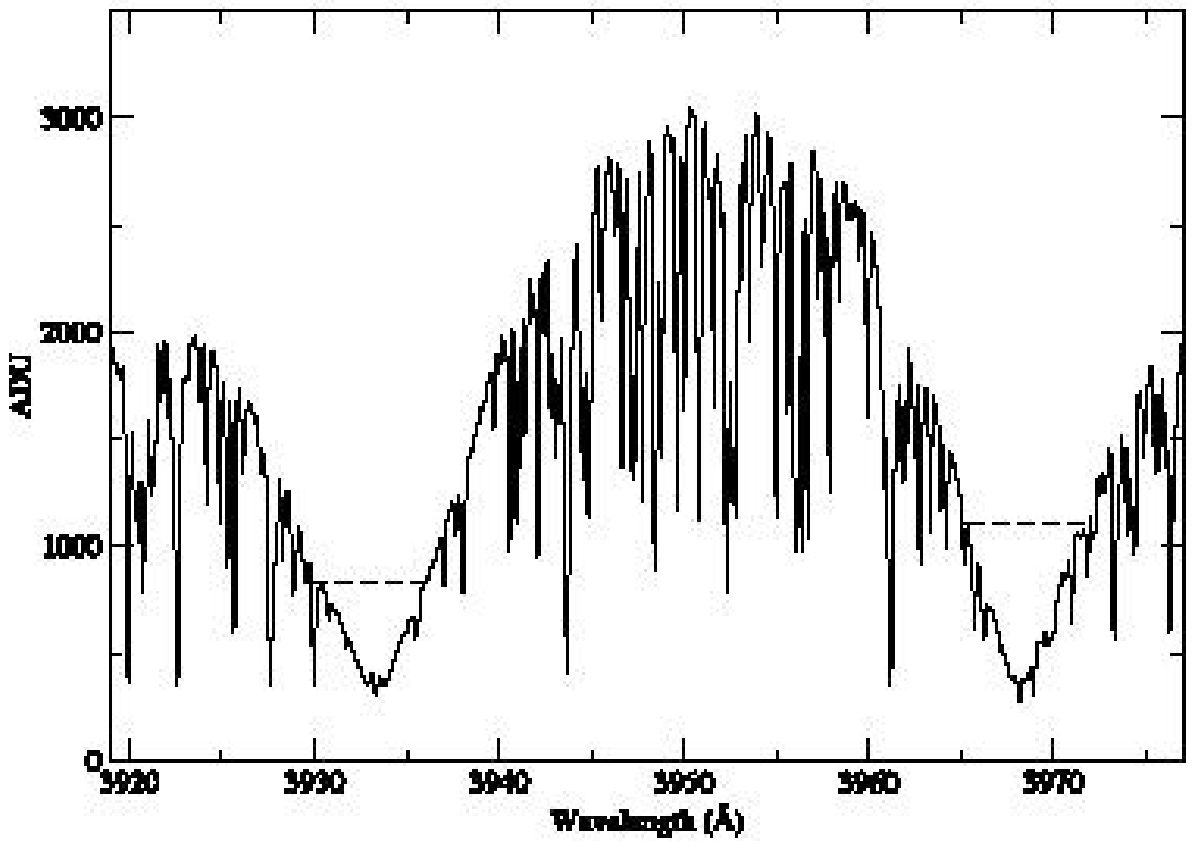
3000
2000
1000
0
ADU
3920
3930
3940
3950
3960
3970
Wavelength (Å)

Ca II K-line Emission induced by Stellar Chromospheric Heating

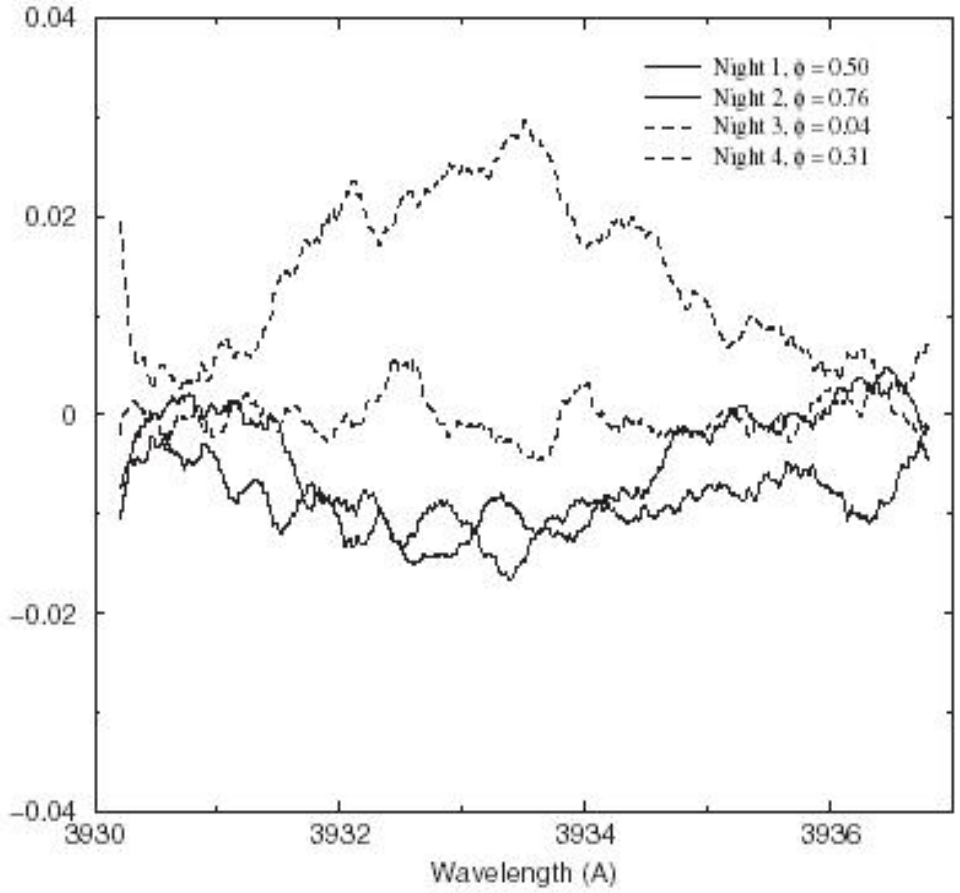

Fig. 2. Ca II K line residuals from the normalized mean spectrum for HD 209458 for four different phases ϕ (Shkolnik et al. 2001).

Magnetic Interaction Important!

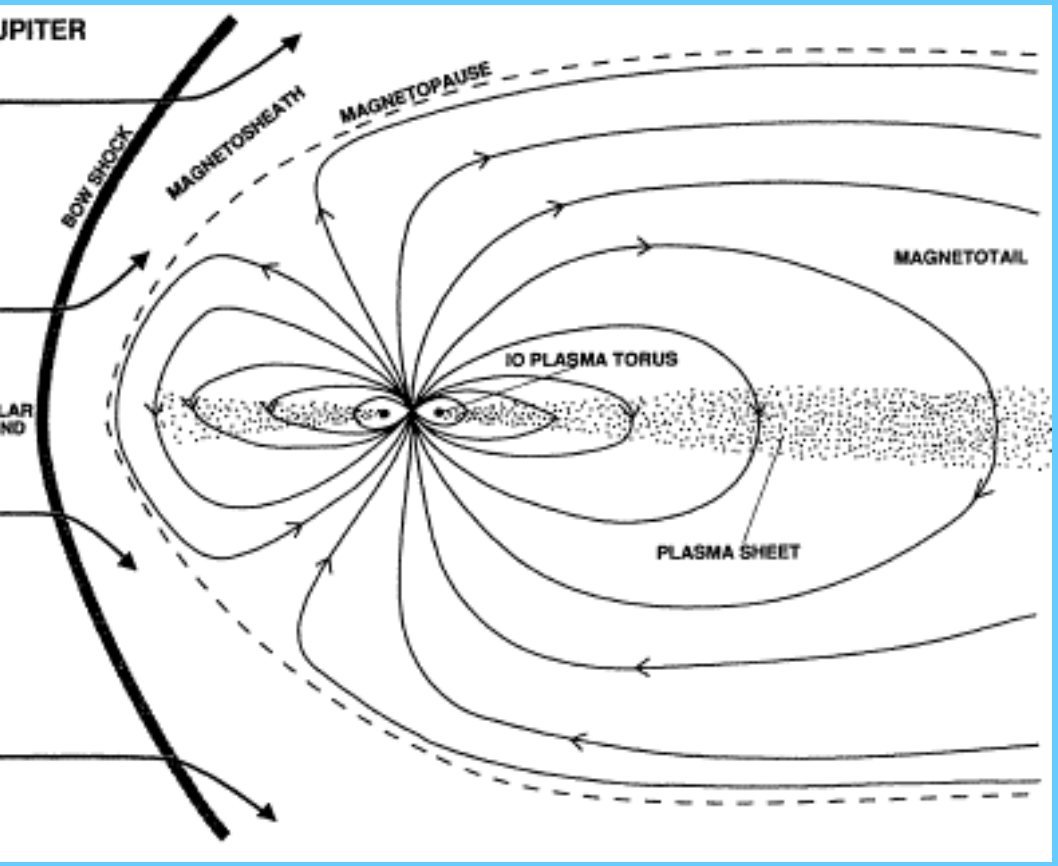

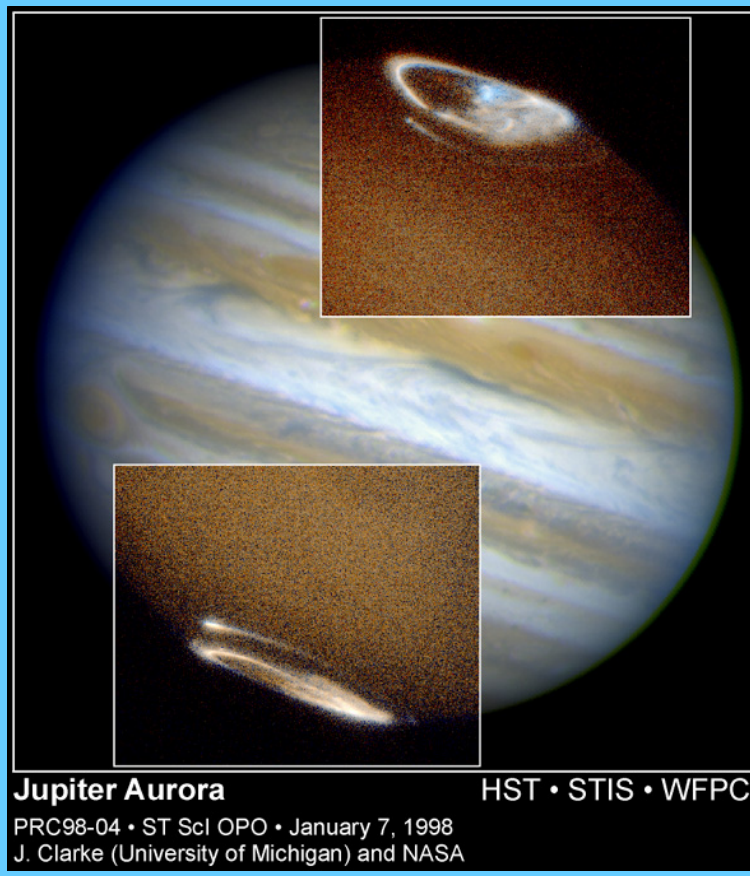

MHD Simulations of Exoplanet Interaction

- Interaction dominated by magnetic field
- Sub-Alfvenic interaction

➠No bow shock

- “Open” and “shut” cases determined by stellar field direction

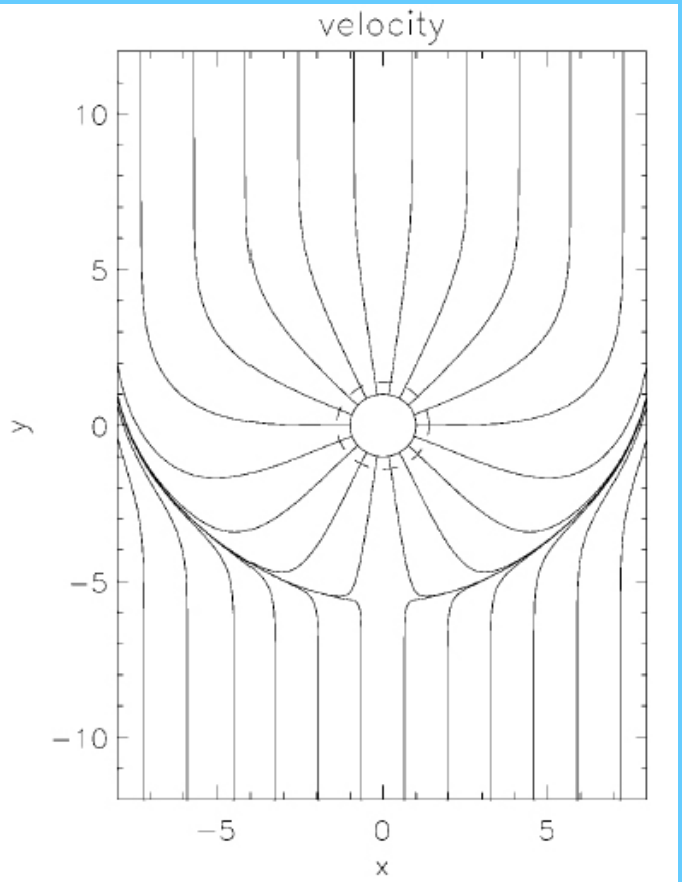

FIG. 1.—Plasma flow pattern on the equatorial plane resulting from the interaction of the expanding stellar corona and the dipolar magnetic field of a CEGP. The external coronal flow and the internal magnetospheric plasma flow are divided by a contact surface. Because the stellar outflow is highly sub-magnetosonic, no bow shock forms in the upstream region. Both of the vertical and horizontal coordinates are in units of planetary radii.

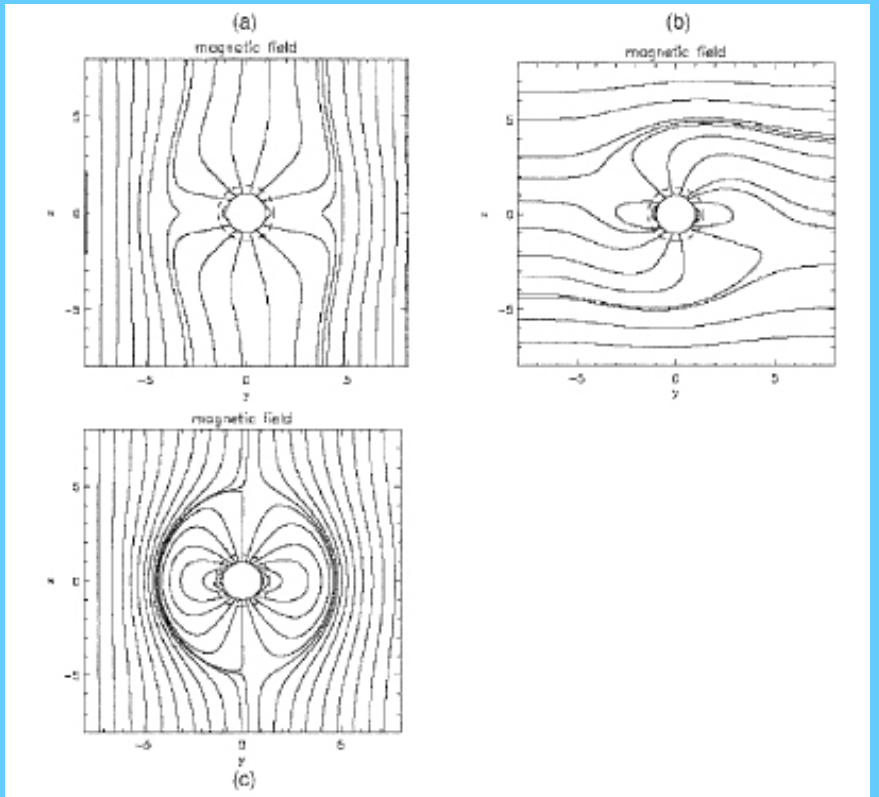

FIG. 2.—Magnetospheric configurations of the exoplanet with different orientations of the coronal magnetic field. (*a*) Open case, in which the pointing direction of the coronal magnetic field is opposite to the planetary field at the equatorial region. (*b*) Intermediate case, in which the coronal magnetic field is pointing radially. (*c*) Closed case, in which the direction of the coronal magnetic field is parallel to the equatorial planetary field. As in Fig. 1, the coordinates are in units of planetary radii.

Ip et al. ApJ, 602, L53.

Energy input:

$$
\begin{aligned}
P &= V_s B^2 L^2 \; ergs \; s^{-1} \\
&\sim 3.4 \times 10^{26} \; ergs/s \\
if \; V_s &\sim 280 \; km/s \\
B &\sim 0.1G \\
&\sim 5R_J
\end{aligned}
$$

Energy ~ a typical solar flare

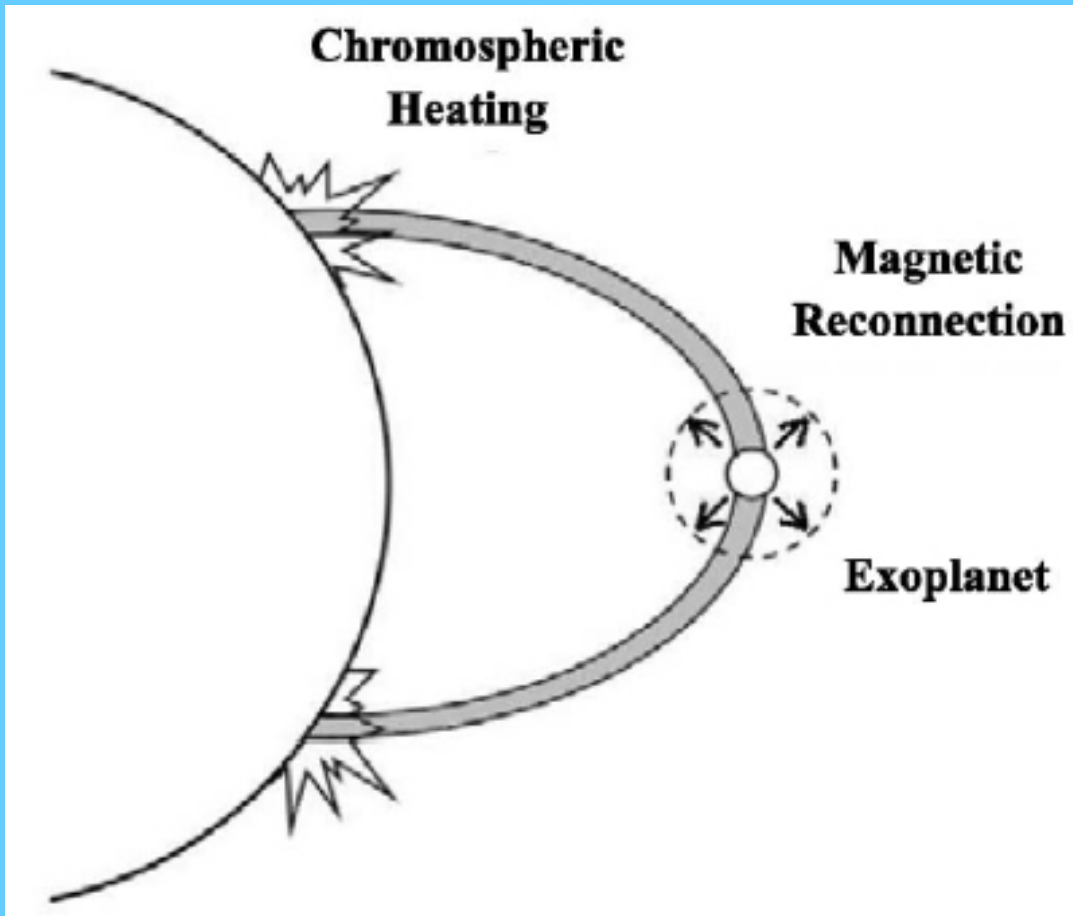

FIG. 3.—Illustration of how a strong electrodynamical interaction could lea to both chromospheric heating of the host star and massive atmospheric escap of the close-in exoplanet by solar flare–like process driven by magneti reconnection.

Exoplanet – Star Interaction

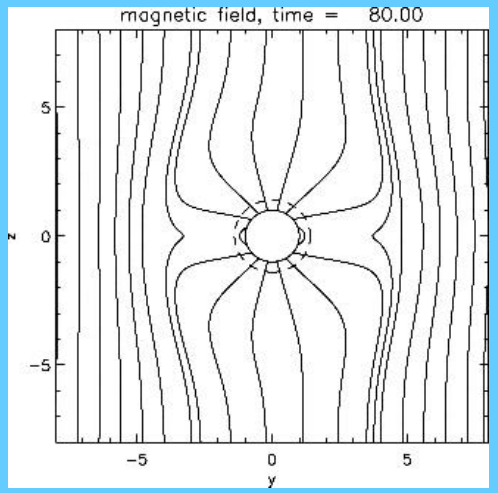

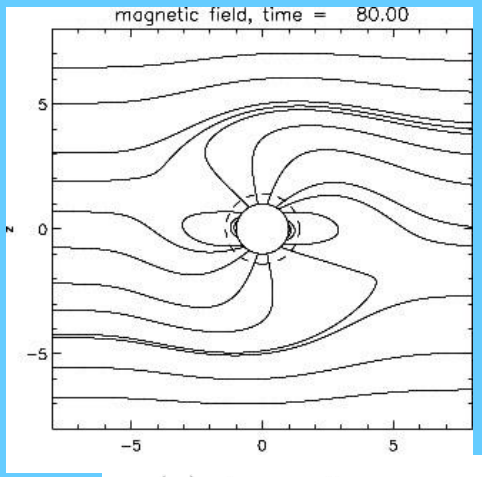

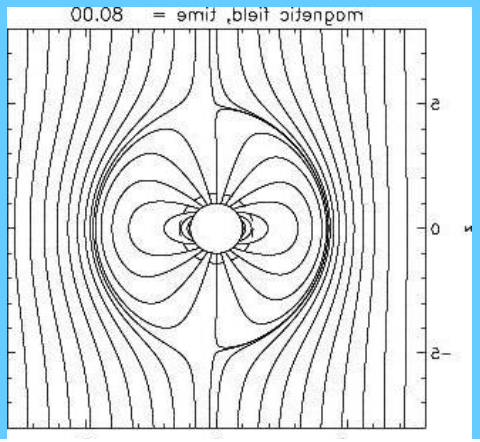

(a) Open Case (b) Closed Case

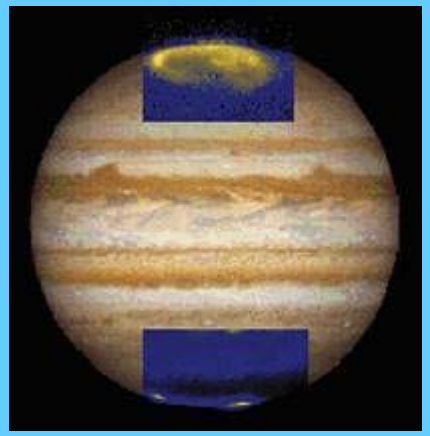

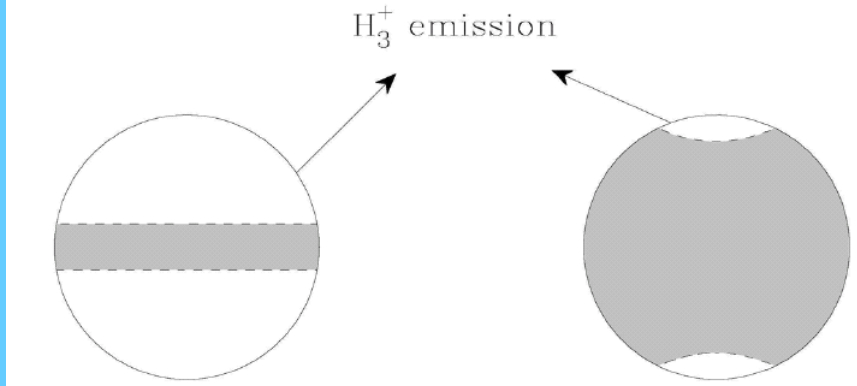

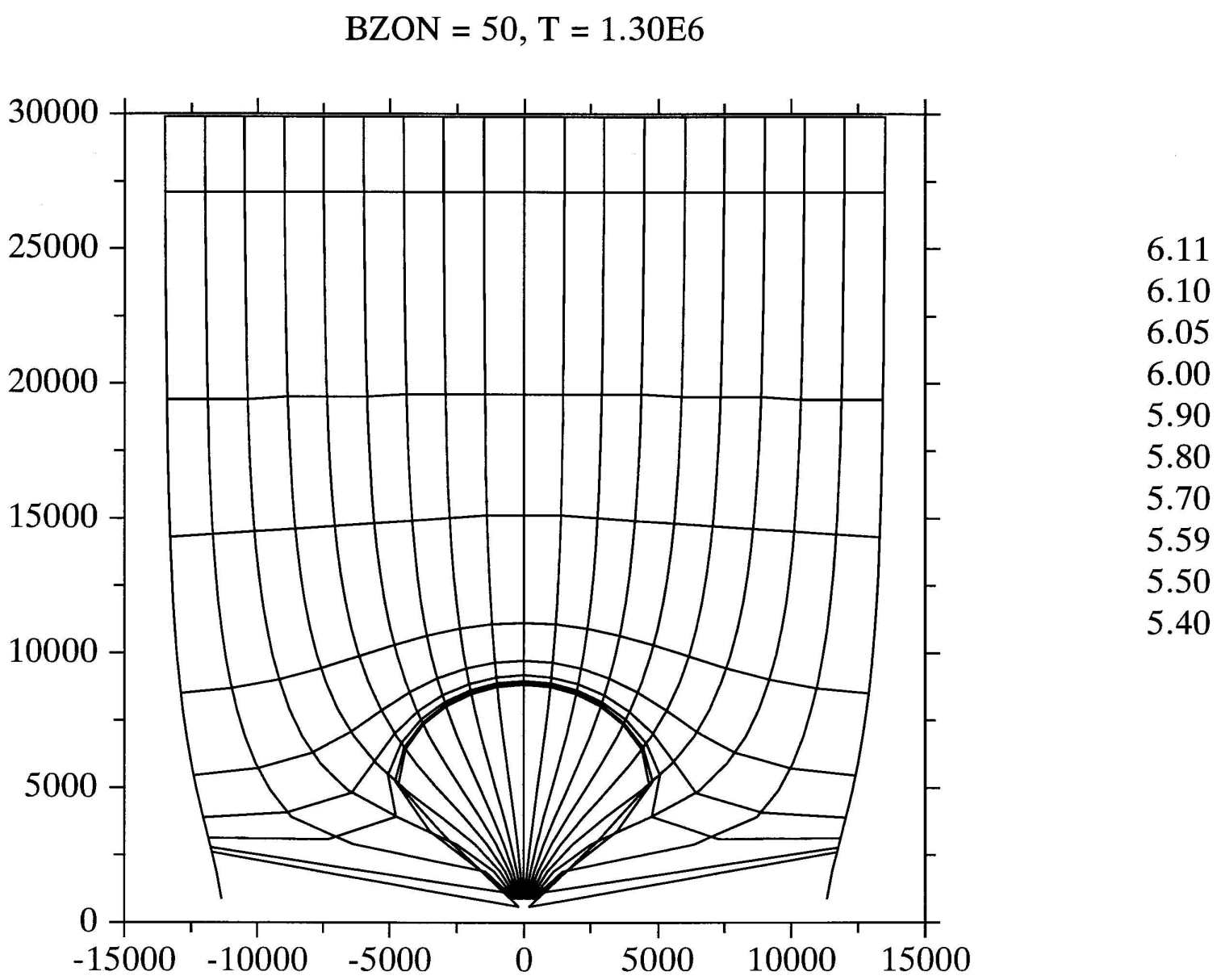
BZON = 50, T = 1.30E6
30000
25000
20000
15000
10000
5000
0
-15000
-10000
-5000
0
5000
10000
15000
6.11
6.10
6.05
6.00
5.90
5.80
5.70
5.59
5.50
5.40

H alpha Emission Feature?

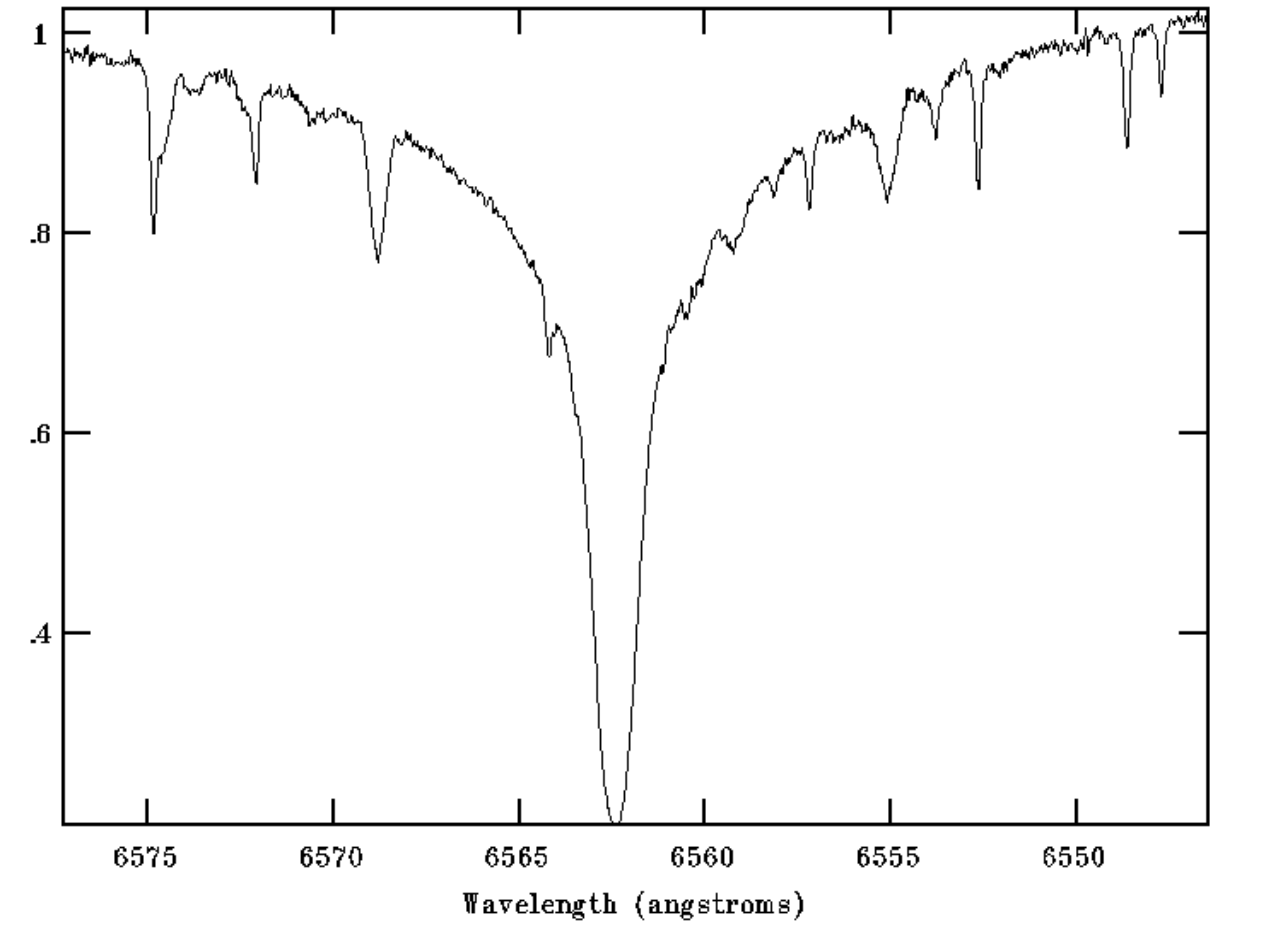

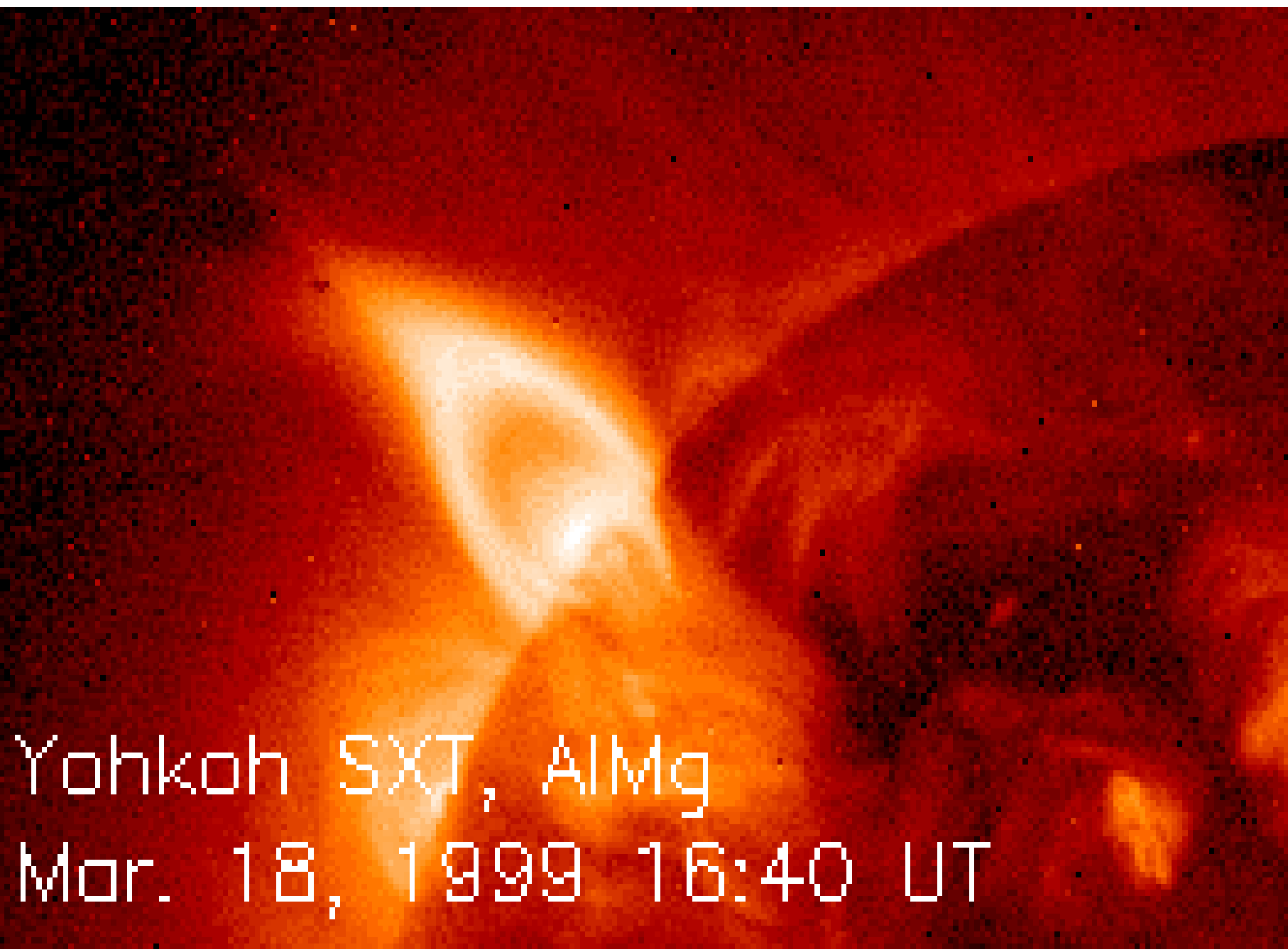
Yohkoh SXT, AlMg
Mar. 18, 1999 16:40 UT

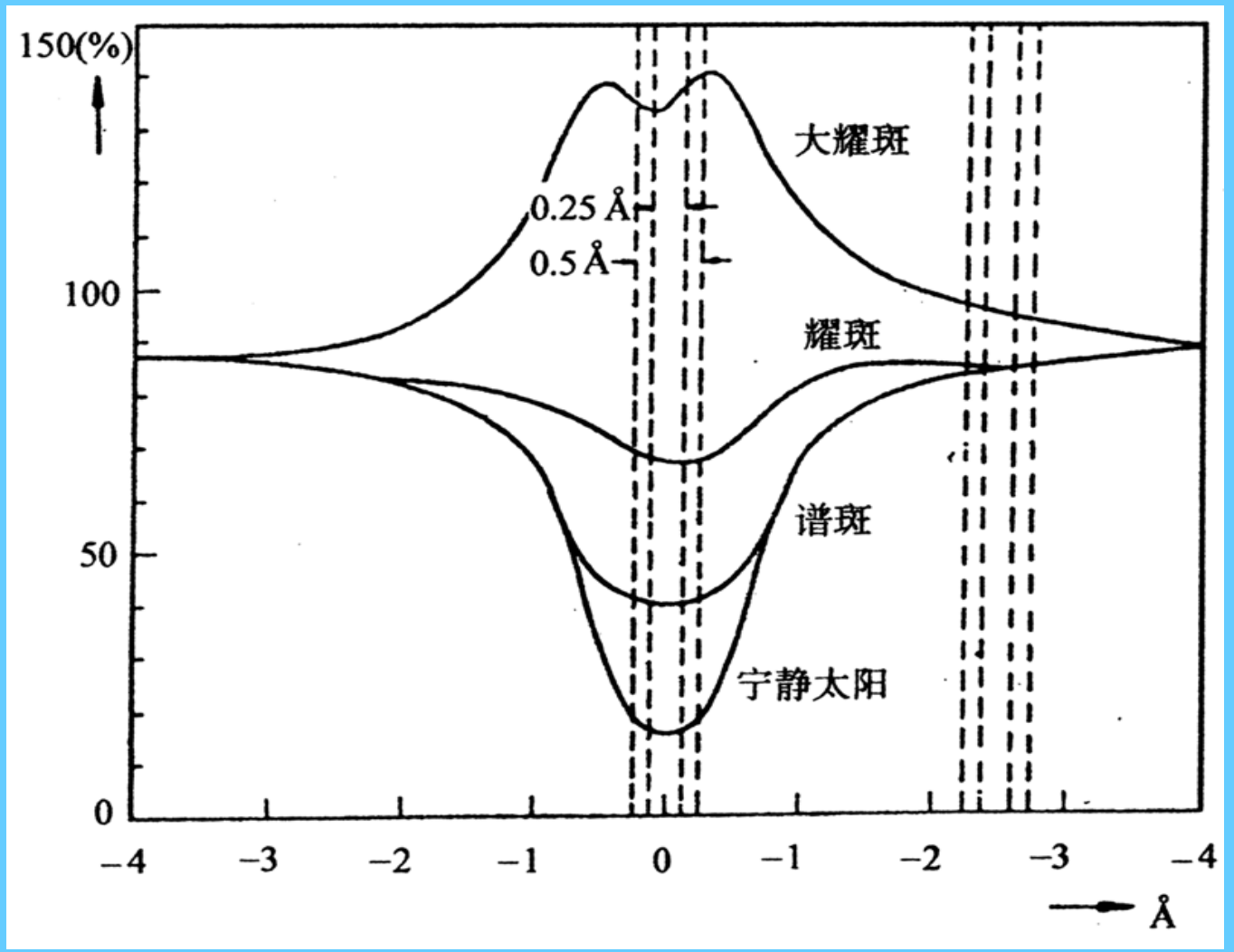
150(%)
100
50
0
大耀斑
0.25 Å
0.5 Å
耀斑
谱斑
宁静太阳
−4
−3
−2
−1
0
−1
−2
−3
−4
Å

Okayama HIDES Observations

March 26-April 3, 2004

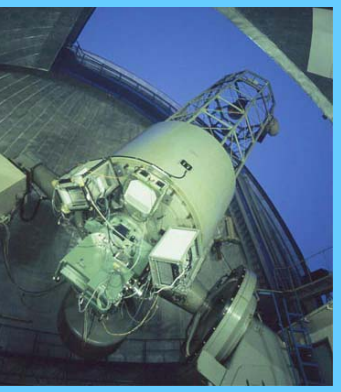

188cm telescope)

2004/04/02

2004/03/28

Tau Boo

Tau Boo b

Raw data in time series

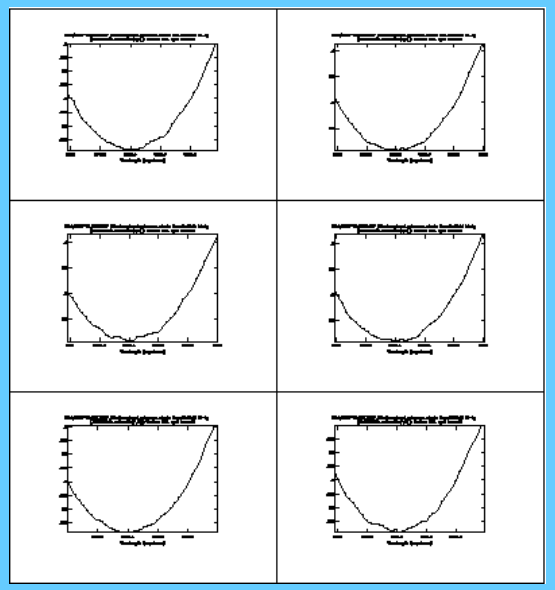

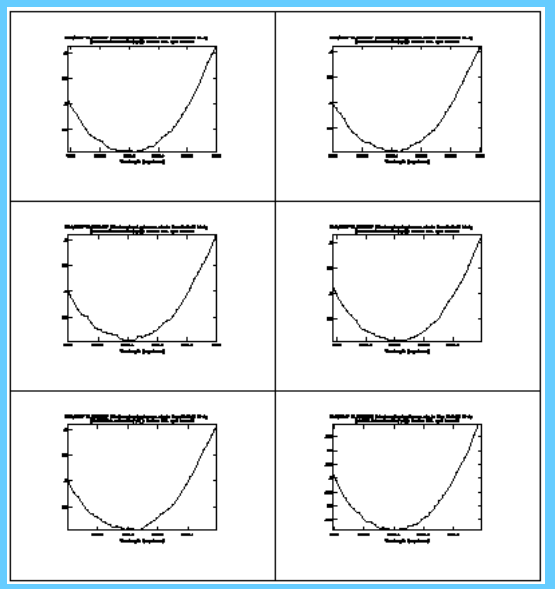

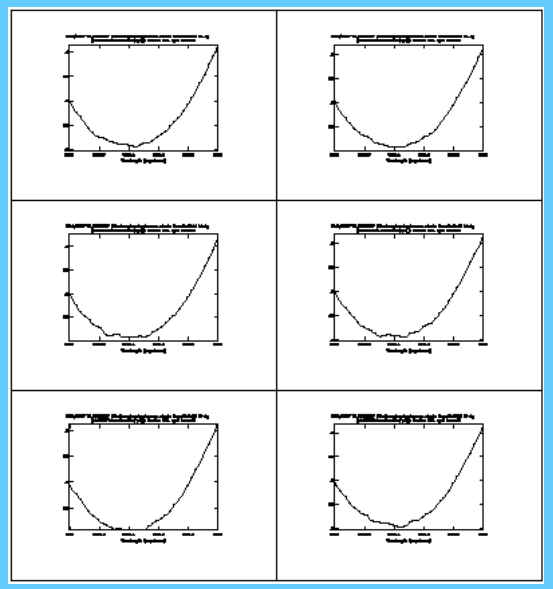

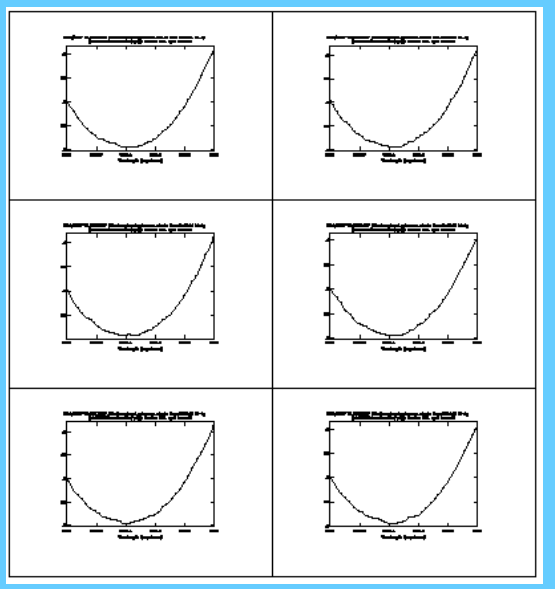

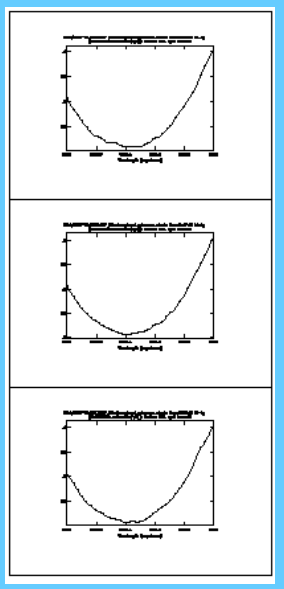

Spectroscopic Mapping of Hot Spots

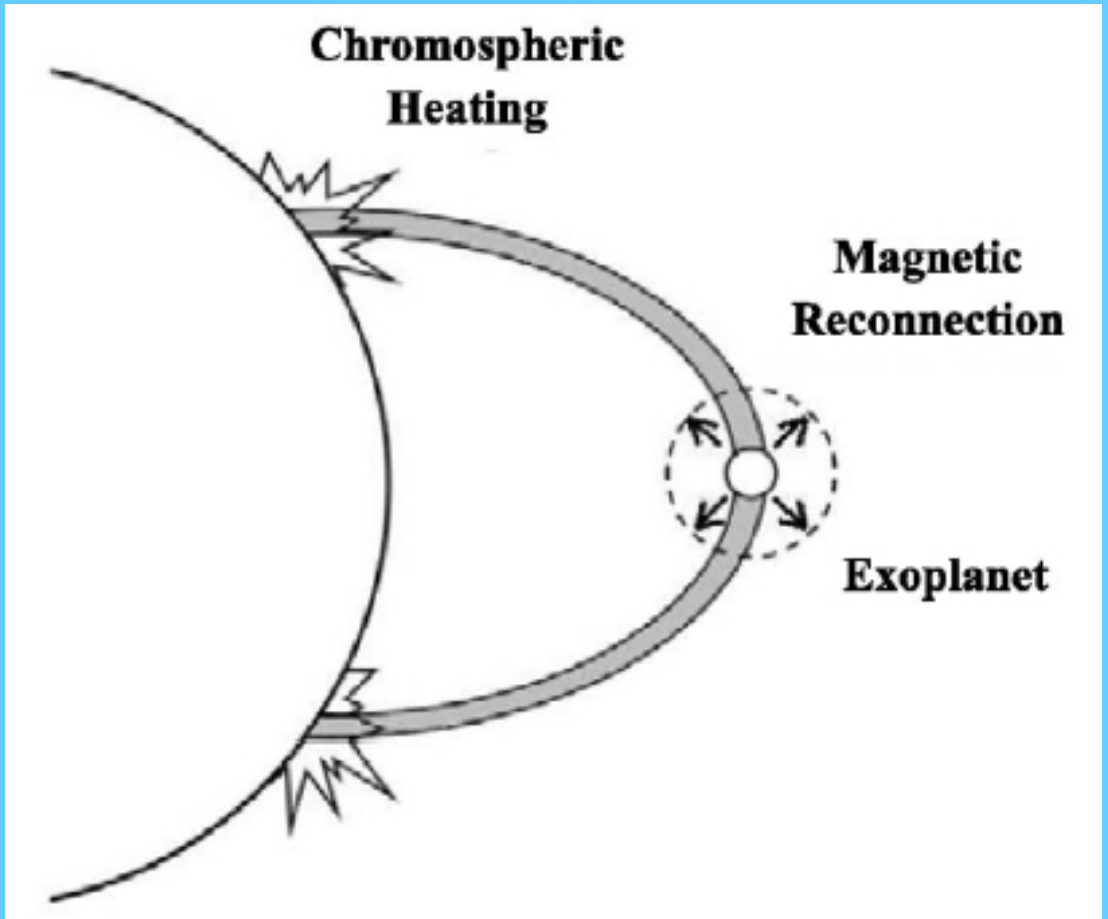

FIG. 3.—Illustration of how a strong electrodynamical interaction could lead to both chromospheric heating of the host star and massive atmospheric escape of the close-in exoplanet by solar flare–like process driven by magnetic reconnection.

Osiris

The Egyptian god of the underworld and of vegetation.

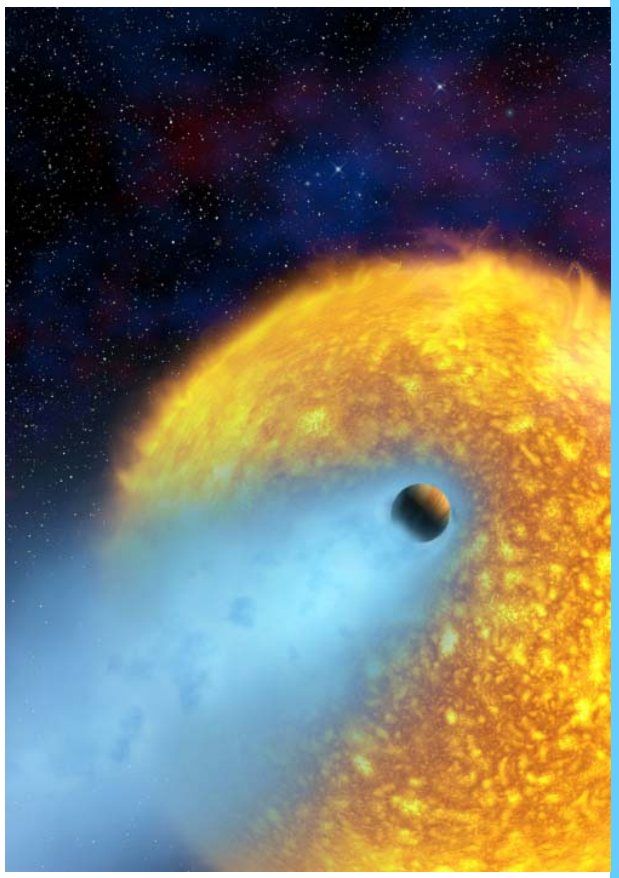


瀬名秀明
八月の博物館

There are always new things (worlds) to be found.